Optomechanics for Inertial Sensing

A Dissertation

Presented to the Faculty of the Graduate School

of Cornell University

In Partial Fulfillment of the Requirements for the Degree of

Doctor of Philosophy

by

David Neil Hutchison

May 2014

DAVID.N.HUTCH@GMAIL.COM

Optomechanics for Inertial Sensing

DAVID NEIL HUTCHISON, PH.D. DISSERTATION

CORNELL UNIVERSITY 2014

Abstract

Inertial MEMS (accelerometers and gyroscopes) is a rapidly-growing billion dollar industry. At the heart of these devices is a displacement sensor. Since its commercialization in the 1980s, the core technology has not changed (viz., capacitive displacement readout of mass-on-springs), for almost all commercially-available inertial MEMS. However, recent developments in integrated optomechanics when combined with recent low-cost on-chip lasers and detectors may enable high-SNR on-chip displacement sensing. Such devices represent a new paradigm in on-chip inertial MEMS sensors, but have yet to be considered in detail in the literature.

In this dissertation we quantitatively investigate several optomechanical displacement sensing schemes, both theoretically and experimentally, and discuss the merits of each approach. These schemes include: cavity deformation sensing, cavity evanescent field displacement sensing (both waveguide or nearby absorber moving), and two-cavity gap sensing.

Beyond simply investigating different sensing schemes, we find that reinventing the traditional displacement-sensing element has the effect of reinventing the entire system. For example the driving circuitry may be simpler and/or lower-power than traditional inertial MEMS driving circuitry, the noise sources are fundamentally different and are limited by different mechanisms, the footprint and cost drivers may be completely reimagined, etc.

Although we have not yet integrated the devices reported here with on-chip lasers and detectors, we show experimental results and modeling for our non-integrated devices, discuss the noise sources to be expected in an integrated device, and survey some on-chip laser/detector noise figures from the literature. Using such noise figures and the measured optomechanical sensitivities, we show that our measured devices when operated as accelerometers could easily achieve sub-$\mu g/\sqrt{\mathrm{Hz}}$ total noise, and thus potentially exceed typical electrostatic MEMS accelerometer performance. Though we have applied these findings primarily to accelerometers, these findings may also be applied to MEMS gyroscopes, or other sensors that involve displacement sensing, such as MEMS microphones, MEMS pressure sensors, and so forth.

Biographical Sketch

David Hutchison was born and raised on the North Shore of Auckland, New Zealand. He attended Torbay Primary, Northcross Intermediate, and then Rangitoto College, where he was interested in physics, art, and music, before coming to the US to study physics at Brigham Young University in Provo, Utah. He began working for Dr. Robert C. Davis in his freshman year. During his first two years he studied ribosomal self-assembly and AFM probe enhancement using *in situ* grown carbon nanotubes. In his final two years he invented a way to make high aspect ratio MEMS in any material with minimal etching, by covering a sparse nanotube "forest" framework with the desired material and then a short etch to release the structure. He obtained several US and foreign patents and published papers about this technology. His other interests during his undergraduate study were improv comedy (performing with BYU's improv comedy club for two years), choral singing, and playing the guitar. David graduated Magna Cum Laude with a degree in physics and minors in Mathematics and Japanese in August 2008.

The next month he began his Ph.D. with the School of Applied and Engineering Physics at Cornell. He first worked with Dr. Sunil A. Bhave and the OxideMEMS group in the School of Electrical and Computer Engineering at Cornell University, and then under the advisorship of Prof. Paul McEuen in the Physics department. During his time at Cornell he worked on a few ideas in optomechanics, then invented a cavity-enhanced optomechanical inertial sensor. On October 22, 2011, he married his wife Stacy Wilson. From July 2012 to February 2014 he interned at Intel Corporation in Santa Clara, California, US, developing other optomechanical displacement sensors and working on integration of on-chip lasers and detectors.

He obtained his Doctor of Philosophy in Applied Physics in February 2014. He is currently continuing his work at Intel Corporation in Santa Clara as Research Scientist.

To Stacy

Acknowledgements

I would like to thank my current advisor Prof. Paul McEuen and my past advisor Prof. Sunil Bhave for valuable direction and guidance. Also, I will forever be in debt to Haisheng Rong and John Heck at Intel Corporation for giving me a chance and guiding me towards success. John in particular has always looked out for me and helped me in countless ways for which I can never fully repay.

Thank you to the members of my committee: Dr. Michal Lipson, Dr. David BenDaniel, and Dr. Craig Fennie, and Dr. John Heck, for your time and thoughts.

I am also thankful for the friendship and support the OxideMEMS group: Dana Weinstein, Hengky Chandrahalim, Eugene Hwang, Suresh Sridaran, Tiffany Cheng, Laura Fegely, Siddharth Tallur, Tanay Gosavi, and Ryan Wang. I am particularly indebted to Suresh for his mentorship during our overlapping time at Cornell. Thank you to all my colleagues at Intel for their camaraderie, help, and valuable insights. Thanks to my friends at Cornell in ECE, AEP, and the Cornell Student Branch.

This work would not be possible without the help and support of the entire staff of the Cornell Nanoscale Science and Technology Facility (CNF) and Stanford Nanofabrication Facility (SNF), and the always-helpful Sally Yanez at Intel.

Thanks to my brothers, sisters, and parents, and grandparents, whose loving support has always been an example to me of how to raise my future family.

Most of all I thank my wife Stacy, my *joie de vivre*, for her infinite love, sacrifice, and support; lil Elsa for being so much fun; and God for makin' it all happen.

Table of Contents

List of Abbreviations

Ch.	Chapter
Sec.	Section
Eq.	Equation
Fig.	Figure
MEMS	Microelectromechanical Systems
OM	Optomechanics or Optomechanical, depending on context
RIN	Relative Intensity Noise (of a laser)
FEM	Finite Element Modeling
FDTD	Finite Difference Time Domain
TE / TM	Quasi-transverse-electric or quasi-transverse-magnetic optical mode
SOI	Silicon-on-insulator
LPCVD	Low-pressure chemical vapor deposition
FWHM	Full-width at half-maximum (of a Lorentzian-shaped resonance)
HWHM	Half-width at half-maximum
DUT	Device under test
NEP	Noise-equivalent power (for a detector)
PC / PV	Photoconductive or photovoltaic mode (for a detector)

Chapter 1 : Introduction

There was this huge world out there, independent of us human beings

and standing before us like a great, eternal riddle,

at least partly accessible to our inspection and thought.

The contemplation of that world beckoned like a liberation.

-- Albert Einstein

1.1 : Overview and objectives

This primary purpose of this dissertation is to answer the question: *How may displacement be sensed, on-chip, optically, and how do these approaches compare?* To put this in context of some commercially important devices, in many places we specifically apply these findings to *inertial sensors* (accelerometers and gyroscopes), however micromechanical displacement sensors are a large part of many useful microelectromechanical (MEMS) systems. MEMS accelerometers and gyroscopes need to read out the position of the proof mass; pressure sensors may need to read out the deformation of a membrane or movement of another micromechanical element, mechanical mass sensors may need to read out the resonant frequency of a vibrating element before and after some molecule or particle has attached itself. So, in this dissertation we target inertial sensors but present a largely device-agnostic, theoretical and experimental analysis of some types of optomechanical displacement sensors that we hope will be useful for some of these applications.

Many more possible reasons are given as the text unfolds – however at the outset we were originally motivated by several reasons:

(A) Despite the fact that capacitive displacement sensing is almost ubiquitous in MEMS today, the most sensitive displacement measurements in science are done using optical techniques, not capacitive gaps – just to give one example, consider the Laser Interferometer Gravitational wave Observatory (LIGO), which is searching for tiny changes in cavity length as a gravitational wave passes through the optical cavity. We usually use capacitive plates in on-chip MEMS because historically these have been the tools available in the world of microfabrication, while on the length-scale of LIGO many techniques are available – but what if newer better tools became available on the micro-scale?

(B) The recent development of microfabricated on-chip lasers, for example by University of California at Santa Barbara, and Intel Corporation [1]. Using silicon microfabrication techniques for such components enables massively scalable production and optical systems with unprecedented small form factors and low cost compared to traditional piecemeal-assembled optical systems.

(C) On-chip detectors are now available in a variety of forms, e.g. [2].

(D) The recent birth of the field of optomechanics (OM)[1], and with it a deeper understanding of the interaction between light and motion of physical objects (mirrors, waveguides, etc.) in a variety of configurations.

(E) Optical sensors with their associated circuitry may have other advantages over traditional capacitive sensing. Some of these may include more "knobs" to play with to engineer a sensor for a particular purpose, new effects that may be harnessed such as optical forces, optical

[1] Note: We use the acronym "OM" to refer to either "optomechanics" or "optomechanical" based on context.

feedback, optical heating and cooling, higher immunity to electromagnetic interference or high-temperature operation, etc.

Thus we began our investigations into optomechanics for displacement sensing; this dissertation reports the results.

1.2 : Structure of this dissertation

Here we introduce several different on-chip OM displacement sensing schemes, and investigate them analytically, computationally, and experimentally, then compare between approaches.

Chapter 1 provides the reader with an overview and an introduction to displacement sensing, optics, and optomechanics. We also categorize and review past approaches to optomechanical displacement sensing.

Chapter 2 describes some groundwork needed for the present work: first, it covers the important parameters for that will be referred to in subsequent chapters, and secondly it describes test setups that were built, that we refer to in following chapters. In this sense it functions partially as an appendix, however since the concepts presented here are integral and not tangential to the following chapters, we include this as a chapter rather than an appendix at the end.

Chapters 3, 4, and 5 describe different types of optomechanical displacement sensors we invented or analyzed. This list of sensor types is not necessarily exhaustive. Each chapter will talk about the basic sensing principle and variants, analytical modeling, computational modeling, and experimental results.

Chapter 6 includes conclusions and a comparison of the devices in Chapters 3-5, along with a comparison with acceleration noise of some commercial accelerometers.

1.3 : Example motivation case: Inertial MEMS

Though displacement sensing is important to most MEMS devices, to give motivation, now we will consider in more detail how on-chip displacement sensors might apply to inertial sensors specifically. Along the way, we will uncover some interesting motivations that may not be otherwise obvious – for example, arguments of simplified driving electronics, potentially lower power consumption, and footprint.

1.3.1 : Why inertial MEMS?

One of the first commercial uses for MEMS was for car airbag deployment sensors in the 1980s. Today it is primarily driven by the consumer electronics market, and in particular by smartphones and tablet computers. In particular, inertial sensors commonly used in:

- Smartphones, tablets, ultrabooks, gaming controllers, etc., to measure orientation, rotation, and vibration, for motion input or navigation.
- Wearable electronic devices to measure motion or physical activity.
- Laptop computers to park the hard disk head when free-fall is detected (if the laptop is dropped), to prevent damage to the hard disk when the laptop hits the ground.
- Electronic stability control (ESC) for vehicles such as cars. When ESC detects the car is moving in a way not allowed by the tires in normal operation (i.e. the car is skidding instead of traveling in the direction the tires are pointing), ESC applies the brakes to individual wheels to help overcome skidding and "steer" the vehicle where the driver intends to go. Although the idea dates back to 1987, recently regulation in many countries has begun requiring all new cars to have ESC (for example, all 2012 vehicles under 10,000 lb. in the US must have ESC systems, each of which require accelerometers and gyroscopes) [3].
- Digital cameras to detect orientation and sometimes for image stabilization (correcting for the jitter of a user's hand).

- Industry to measure vibrations or movement of critical machines, buildings, safety installations, and so forth.

Inertial sensors comprise about a $1-2B growing market, as shown in Figure 1.1.

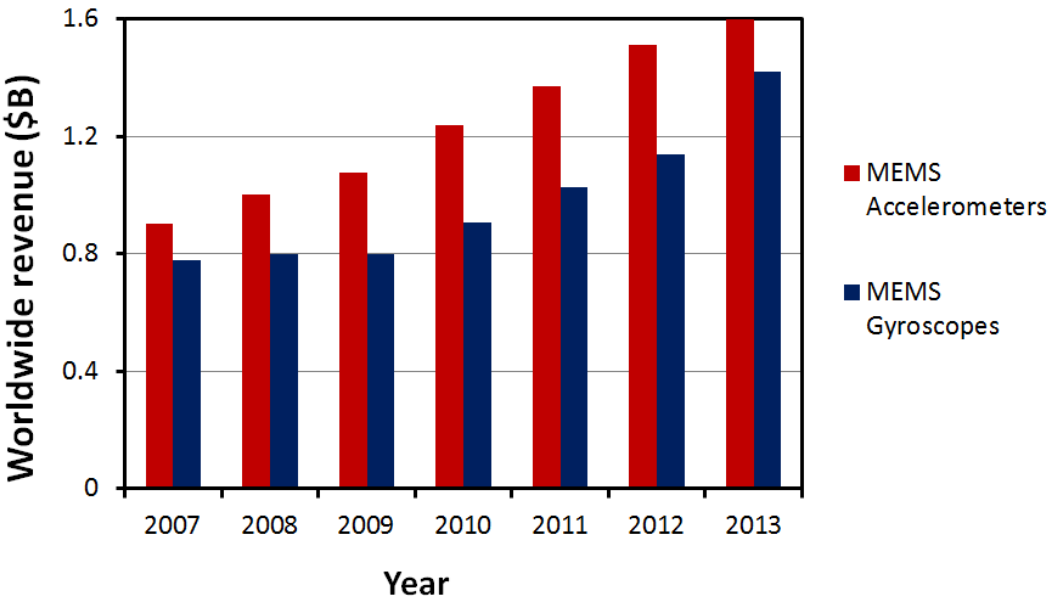

Figure 1.1

Total revenue from MEMS accelerometers and gyroscopes up to 2011 (estimated) and beyond (projected – this data is from a 2011 industry report). Adapted from [4].

Cheaper, smaller, and lower power MEMS will always be attractive to the MEMS industry, and these are some of the technology drivers. However we may ask whether *performance* is a driver – do inertial sensors really need to be any *better*? One way it might be "better" may be to have low noise, or more correctly, higher SNR; other ways might be to have higher dynamic range or lower drift, for instance. So, for instance, do we need better SNR? In truth, if all we wanted was to have an accelerometer that could determine if a smartphone was being held in portrait or landscape mode, the

problem is already solved. However, to ask whether today's sensors are good enough for today's applications is not the important question, because better sensors beget new applications.

For example, some very expensive defense-related (e.g. Northrop Grumman's Hemispherical Resonator Gyro [5]) or experimental gyroscopes (e.g. [6]) may have orders-of-magnitude lower noise or drift which can enable "northfinding" and GPS-denied navigation (but, in some cases may be many orders of magnitude more expensive). *Northfinding* refers to measuring the Earth's rotation vector directly so that (after a sufficient period of averaging while the device is stationary), north can be determined without the need for a MEMS compass (this is useful because a MEMS compass measurement is frustrated by stray magnetic fields or nearby metal). *Navigation*, on the other hand refers to tracking the sensor's movement by integrating the gyroscope signal to find the heading, and double-integrating the accelerometer signal to track position. This is important because a user may want to use their smartphone to navigate inside of a shopping mall, for instance, where GPS signal does not penetrate. Today's inertial MEMS alone are far too noisy to enable indoor navigation. It is true however that today's accelerometers and gyroscopes when combined with other techniques such as WiFi-triangulation, sensor fusion algorithms, Simultaneous Localization And Mapping (SLAM), etc., can have varying degrees of success with indoor navigation, but in each case (WiFi-triangulation, SLAM, etc.) there is some drawback (e.g. WiFi-triangulation may require additional hardware to be set up, and the arena calibrated; SLAM may require a clear camera view with a constant video stream, a lot of processing power, recognizable surroundings, etc.). In any case, simply having better sensor data in the first case is truly the best approach to solve the problem of indoor or GPS-denied navigation, and today's inertial sensors are far from sufficient to solve this problem.

1.3.2 : What is an accelerometer?

An accelerometer is simply a mass m attached by springs k to a frame, as shown schematically in Figure 1.2 (a). Under a known acceleration a of the frame, the inertia of the so-called "proof mass" causes the springs to deform and the mass to be displaced according to $F = m\,a = k\,x$, where x is the displacement from equilibrium. Thus by measuring the displacement from equilibrium we calculate the acceleration. Of course this is true only below the resonant frequency; at the mechanical resonant frequency[2] ω_m the mass is driven to larger amplitude by the same driving acceleration; above the resonant frequency the inertia of the mass cannot respond quickly enough and the amplitude is reduced, as in Figure 1.2 (b).

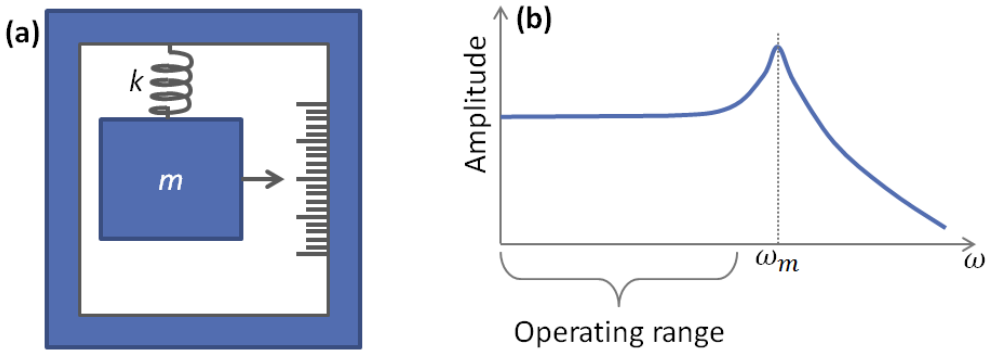

Figure 1.2

(a) An accelerometer is simply a mass on springs with a displacement readout. (b) The frequency response of an accelerometer. Such a device has some mechanical resonant frequency ω_m and is operated as an accelerometer at frequencies below that. In this regime, $ma = kx$. Adapted from [7].

So, accelerometers are designed to sense accelerations below their resonant frequency. The displacement-sensing element is almost always a pair of electrodes separated by a gap, with the

[2] Note that in this dissertation we use subscript "m" to refer to mechanical quantities and "o" to refer to optical quantities.

position of the proof mass sensed by measuring capacitance across the electrodes. To increase the area of the capacitor these plates are usually in the form of interdigitated “comb fingers” as shown in Figure 1.3. The “differential capacitance” comb finger configuration in Figure 1.3 (a) is best for sensitive measurements of displacement. Also pictured is a “fringing field” comb fingers in Figure 1.3 (b) for comparison – though these are more suited to electrostatic actuation rather than sensing, and allow for larger displacements.

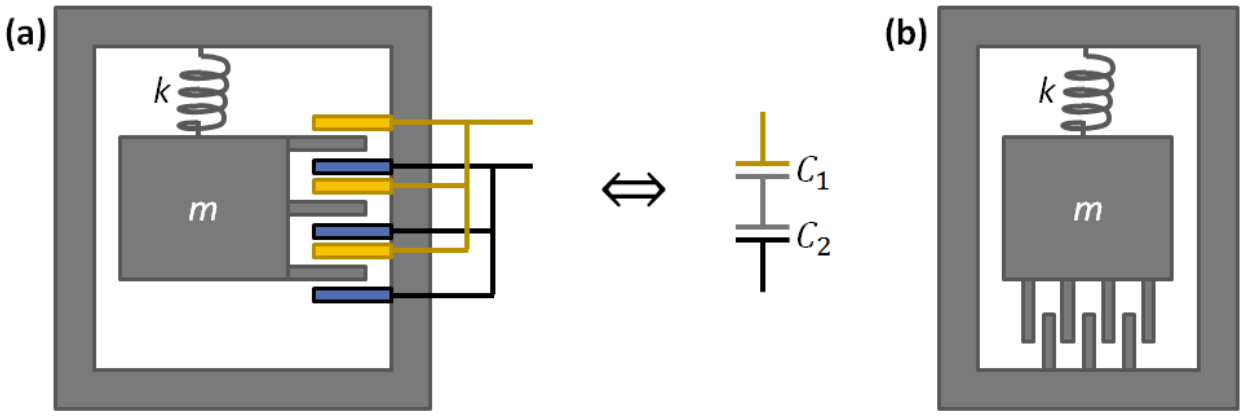

Figure 1.3

(a) A differential capacitance $C_1 : C_2$ is formed when mass m moves vertically, since the C_1 gap increases (decreases) and the C_2 gap decreases (increases). (b) For comparison we show this “fringing field” comb finger arrangement. This can also sense changes in the gap, however it is less effective at this compared to (a) and is instead usually used to drive the mass m into vertical motion since large displacements can be attained.

1.3.3 : What is a gyroscope?

MEMS gyroscopes exist in many forms and a discussion of the various current designs would take us beyond the scope of this dissertation. Instead we choose perhaps the simplest imaginable design

for purposes of discussion here. This will illuminate the basic operation and also show where the displacement sensors in this dissertation may be applied.

Figure 1.4 (a) shows a basic accelerometer with four straight springs clamped at points P to the frame. The mass is shown moved upwards from equilibrium position for clarity. A simple gyroscope design is shown in Figure 1.4 (b) and (c), and may consist of an outer frame of mass m_1, with an inner mass m_2 oriented perpendicularly to the first mass. The inner mass, viewed by itself, is simply an accelerometer. If the mass of m_1 and m_2 are driven (electrostatically or otherwise) in the y-direction, with no overall rotation, the inner mass m_2 will not move relative to the outer mass m_1. However in the presence of an overall rotation in the z-direction, in the reference frame of the device, there is an acceleration of the inner mass of

$$\boldsymbol{a_C} = -2\,\boldsymbol{\Omega} \times \boldsymbol{v} \qquad \text{Eq. 1-1}$$

which we may sense in a similar way to how linear acceleration was sensed in the accelerometer: by measuring the displacement of m_2 relative to m_1.

Thus we see that at the heart of both accelerometers and gyroscopes there is a *displacement sensing element*. In this thesis we are not reinventing the mass or springs (which are required by the laws of physics for mechanical-based inertial sensing), nor the drive mechanism used to drive the gyro mass at velocity $\boldsymbol{v}$, but only investigating the displacement sensing element.

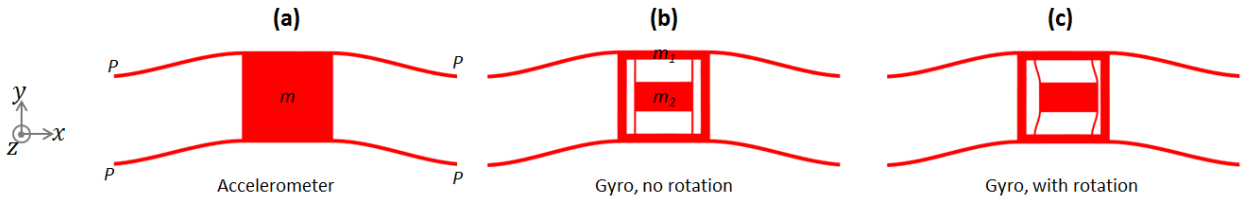

Figure 1.4

(a) A simple accelerometer with mass m and four straight springs clamped at

points P. The mass is shown displaced upwards from equilibrium. (b) A simple gyroscope with an outer mass m_1 and an inner mass m_2. (c) In the presence of an overall rotation in the z direction, the Coriolis force causes the inner mass to move relative to the outer mass.

1.3.4 : Drive and sense circuitry

At first glance it appears that comb fingers "do the trick" perfectly – other than that they might take up die space due to the need for many interdigitated fingers. However one of the most salient points, and actually perhaps one of the least obvious due to years of designing MEMS in the same way, concerns the "hidden side" of MEMS – the driving circuitry. A simplified circuit for measuring the capacitance of a MEMS capacitor plate is shown in Figure 1.5. A high-frequency carrier wave is used to probe the capacitance of the plates.

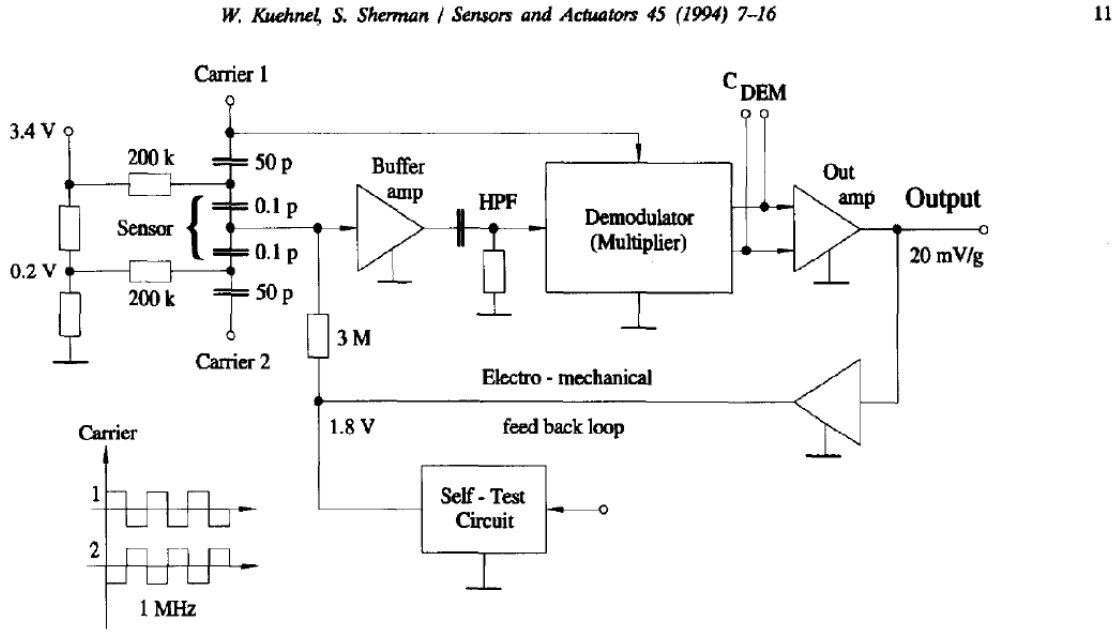

Figure 1.5

Schematic circuit diagram of typical driving circuitry for the differential comb

finger displacement sensor in Figure 1.3 (a). The differential capacitance ("Sensor") is fed two complimentary 1 MHz square wave signals and given a DC bias, then the output signal demodulated to measure differential capacitance. (This also shows a feed-back loop to use it in force-balance mode, not necessary for the current discussion.) From [8].

In contrast, an on-chip light source (such as a hybrid III-V/silicon laser [1]) is driven simply by supplying current I_L, so all that is needed is a low-noise current source; the signal from on-chip photodiodes (such as [2]) is collected by measuring photocurrent I_P. This arrangement is shown in Figure 1.6.

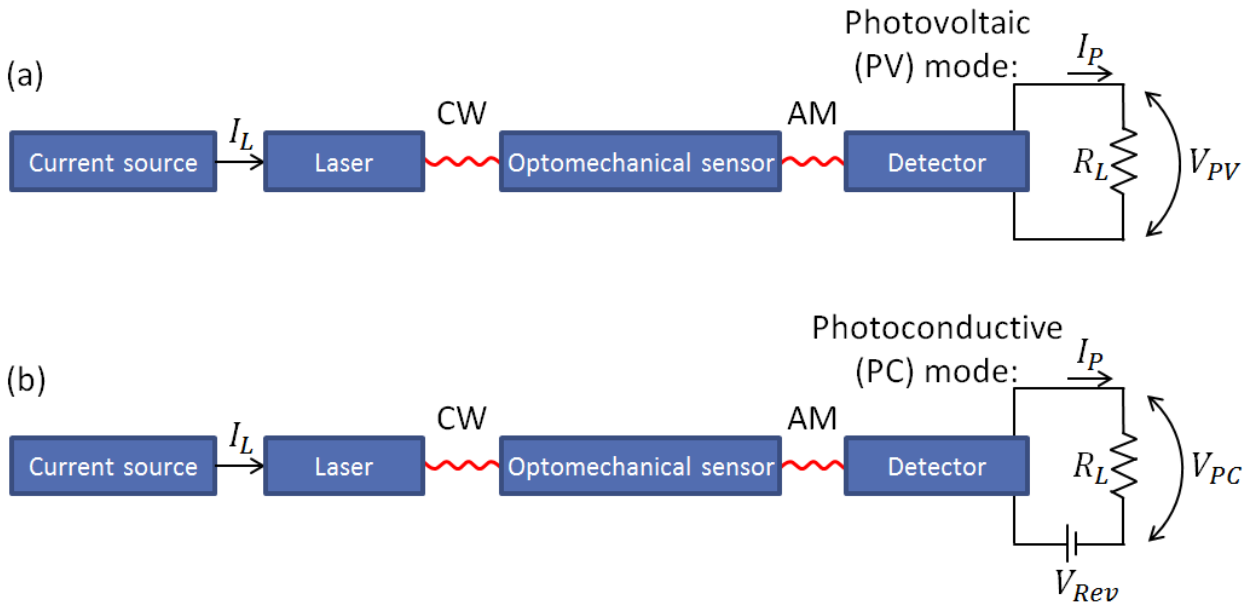

Figure 1.6

General schematic showing an optomechanical sensing system. The laser is driven by a low-noise current source and produces CW light. The detector is reverse biased in photovoltaic mode and unbiased in photoconductive mode, and the photocurrent is measured – shown crudely here by measuring the current

through a resistor, however in practice the signal is fed into an amplifier.

In Figure 1.6 we have indicated the laser light is continuous-wave (CW) and the optomechanical sensor amplitude modulates (AM) the light – other arrangements may be possible but this is what applies to the optomechanical sensors in this dissertation. Meanwhile the detector may be operated in photovoltaic mode (with no reverse bias, (a)), or in photoconductive mode (with reverse bias V_{Rev}, (b)), and the photocurrent measured by measuring voltage across a load R_L. Of course, an amplifier or transimpedance amplifier is usually used rather than a direct measurement of voltage across a load resistor, but this just illustrates the general principle.

Comparing the driving circuitry required in Figure 1.5 and Figure 1.6, we see that not only is the circuitry much simpler (no high-frequency carrier wave input, it's just a DC current source!), the achievable signal-to-noise ratio is limited by different mechanisms – by the photodetector noise and the noise in the simple optical-drive and optical-sense circuitry, for example. Photodetectors can be made to be extremely sensitive and low-noise – even to detecting single-photon levels if desired (e.g. [9]).

We make one final remark about the two detector "modes" shown in Figure 1.6. Photoconductive (PC) mode is the operation mode of choice for most on-chip photodetectors – the benefits being higher bandwidth and a linear output with light intensity. In photovoltaic (PV) mode, we have much smaller bandwidth – the bandwidth is usually limited here by the junction capacitance, and for photodetectors of interest this practically limits the bandwidth to somewhere in the range of 100s of kHz [10]. However for many sensor applications of interest this is already plenty of bandwidth – for example, the mechanical bandwidth of accelerometers is typically a few kHz or tens of kHz; for gyroscopes it is often even smaller. Other sensors such as pressure sensors may have even smaller relevant bandwidths. More importantly, however, operating the same photodiode in photovoltaic mode typically results in lower noise and higher ultimate sensitivity [11]. (In photovoltaic mode, the noise can

be basically the thermal noise generated by a shunt resistance; in photoconductive mode, shot noise from the dark current is an additional source of noise.) The down-side of photovoltaic mode is that the output voltage is logarithmic rather than linear with light intensity, however this can be linearized later, and besides, it is more or less linear when $V_{PV} < V_{OC}$, where V_{OC} is the open-terminal voltage of the photodiode. In any case, our point here is that, contrary to how the vast majority of on-chip photodetectors in the literature are operated – in the photoconductive mode – it may make sense for the detectors associated with future optomechanical sensors to operate in the photovoltaic mode for reduced noise and increased sensitivity to modulation of the light, because the bandwidth is sufficient for these applications.

1.3.5 : Turn-on time and power consumption

The turn-on time of typical MEMS circuits involving electrostatic sensing is usually several milliseconds, often limited by the time needed to charge the capacitances needed for those circuits. In contrast, electrically-pumped lasers, photodiodes, current sources, and possibly even transimpedance amplifiers (which we may use to convert a photocurrent signal to an analog voltage), can have much faster turn-on times. Aside from the obvious benefit of faster off-to-on wait times, this may have the less obvious benefit of lower average power consumption: If a laser and detector can be turned on, stabilize, a measurement taken, and turn off again, all in a fraction of the time between inertial sensor measurements (typical data rates being around 100 Hz to 5 kHz), then the optical circuitry is off for most of the time and can have much lower average power consumption than the capacitive driving circuitry.

To put this in specific terms we turn to results from the literature. We are not aware of any on-chip laser turn-on times that have been reported, however laser diodes used in 10Gb/s optical networks have been made to be operated in such a “burst mode” as we are describing here, with 16 ns full turn-on time including power stabilization time [12]. If we require data-rates of 1 kHz (a typical high-end data

rate for an accelerometer) from a sensor then this means the laser is on for only 16 *millionths* of the cycle. Thus even if the instantaneous power consumption of the laser is a large number like 100 mW, the average power consumption, which is the more important number, is 1.6 *microwatts*.

Of course, the driving circuitry needed for such a current-pulse generator will consume some power, but at the very least we can say that the power consumed by the *laser* itself is negligible in this mode of operation – so the fact we are adding a laser requiring tens or hundreds of mW of *instantaneous* electrical power should not be a big deal – and the total *average* power consumption is primarily due to the pulse generator circuit (which may consume similar power to the high-speed square wave generator in Figure 1.5). So at the very least the power consumption is approximately the same as present-day electrostatic MEMS. However due to the nature of the needed driving circuitry it is likely this can be designed to consume less power than traditional MEMS sensors. Driving circuitry for traditional MEMS accelerometers or gyroscopes, for instance, typically consumes several milliwatts (with turn-on times of typically tens of milliseconds, meaning that they often have to stay on constantly to be able to serve data at typical data rates – so that number is both the instantaneous power and the average power).

1.3.6 : Footprint

Another less obvious advantage for going to optical transduction of accelerometers: footprint can be reduced for the same mass (or, mass increased for the same footprint). Footprint is a factor in cost, and large mass is important for lower thermal-mechanical noise.

Most MEMS accelerometers today are made using a thick SOI (silicon-on-insulator) wafer with a thick (300-600 $\mu\mathrm{m}$) silicon handle wafer and a thinner (usually 10-100 $\mu\mathrm{m}$) silicon on top, separated by a sacrificial oxide layer. If the particular accelerometer is limited by thermal-mechanical noise, it would benefit from being etched through the whole wafer, using more mass, rather than just being made from

a thin layer on top of the wafer (and if it is *not* limited by thermal-mechanical noise then optics can help here too, as we shall see in more detail as this dissertation unfolds). However why is this not done? One reason is that the deep etching used to define the accelerometer's proof mass also defines the comb finger sensors – and these must be defined with vertical sidewalls and small gaps, all the way down their height. Usually ~ 1 to 2 μm comb gaps are desired and the best deep etch systems typically have reliable and repeatable aspect ratios of $\sim 100:1$, so a thick SOI wafer is micromachined instead of the entire wafer. A cross-section of a MEMS accelerometer is shown in Figure 1.7.

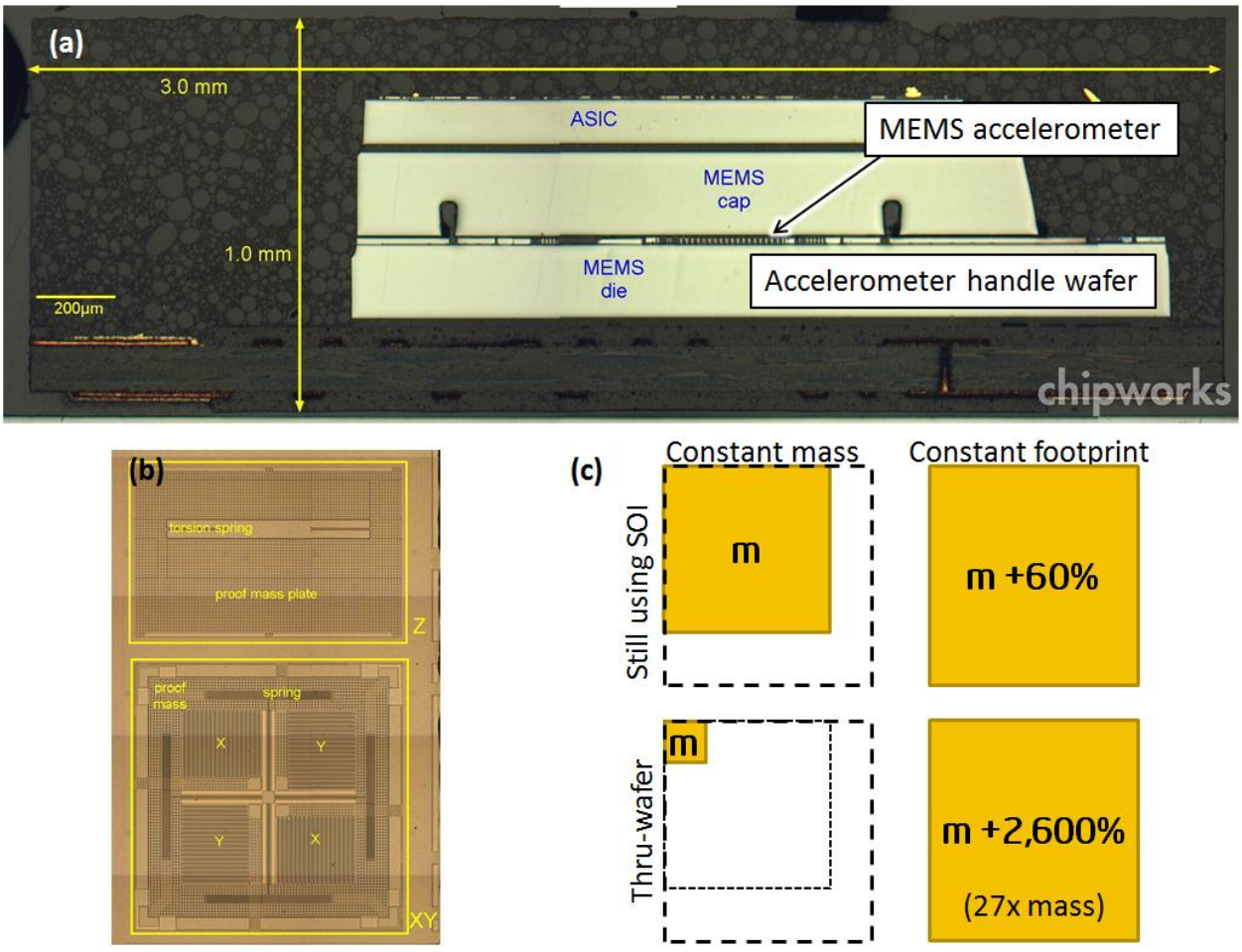

Figure 1.7

(a) A cross-section of the STMicroelectronics LIS331DLH found in the iPhone 4.

Image adapted from [13]*. (b) A top view of the same accelerometer, with z-axis proof mass on top and x and y axis accelerometer on bottom. The four sets of comb fingers (under the small "X" and "Y") consume about 60% of the footprint and need to be fabricated with such small and precise gaps that a through-wafer etch is not possible. (c) As discussed in the text, there are mass and/or footprint advantages when the comb finger geometry no longer sets the proof mass geometry.*

In Figure 1.7 (c) we show in the top row what happens when we stay with SOI wafers but just remove the comb finger area – either a smaller footprint or a 60% mass increase for the same footprint can be achieved. However as we discussed, if the comb fingers are removed then we have no need for precisely-defined high aspect ratio gaps and therefore if we use the entire wafer thickness, the bottom row shows we can gain a huge footprint and/or mass advantage. (The coarse dotted line indicates the LIS331DLH footprint; the finer dotted line traces the "Still using SOI / Constant footprint" square for comparison.)

In saying that we have "no need" for precisely-defined high aspect ratio structures we have neglected the fact that the springs still need to be thin and tall in cross-section, preferably with vertical sidewalls. However this requirement is probably much less stringent because: (A) High aspect ratio fins are typically much easier to fabricate than deep narrow trenches due to etchant and etch product diffusion issues; (B) Even if the fins are not perfectly rectangular but rather slightly trapezoidal, they still act well as in-plane springs because their tall height suppresses undesirable out-of-plane cross-axis sensitivity.

In this argument we have only assumed x or y accelerometers – commercial z-axis MEMS accelerometers often use the handle wafer as one of the electrodes and so it is necessary to have a

handle wafer for that particular design. However in this dissertation we also consider other z-axis (optomechanical) designs that don't require the handle wafer, for example the racetrack resonator in Ch. 3. Also, this argument only partially applies to MEMS gyroscopes, which have electrostatic driving comb fingers in addition to electrostatic sense fingers – if we replace the sense fingers but keep the same drive scheme then we must still use SOI wafers.

1.3.7 : Inertial MEMS example conclusions

We see from our short investigation that *reinventing the displacement sensing element has the effect of reinventing the entire system* and several unexpected benefits beyond simply lower-noise displacement sensing. Similar arguments may be made for other MEMS devices such as pressure sensors, MEMS microphones, absorption mass sensors, and so forth.

1.4 : Review of optomechanical displacement sensing

Optomechanics is a relatively recent field involving the study of the interaction of light, and movement of physical objects in the path of the light. For example, movement of the mirrors of a free-space Fabry-Perot cavity is a simple example of the class of problems covered by optomechanics. Optomechanics has two sides: (1) Using the optical field to sense the movement of some physical object in the optical field; (2) Using the optical field to interact with a physical object, effecting motion. These are often both present in a device, for example in optically-mediated regenerative mechanical oscillations of an optical cavity reported by Vahala *et al.*[14] or many other demonstrations (for example, [15]–[18]). To focus this dissertation we consider only (1).

1.4.1 : Categorization of optomechanical displacement sensors

Over the last few years, a variety of ways to measure displacement on-chip have been reported. We first categorize these methods in Figure 1.8. Those that are discussed in this dissertation have the

relevant chapter listed in blue text beside the device type. In red text is listed a numbering scheme that is used in the literature review of Sec. 1.4.2.

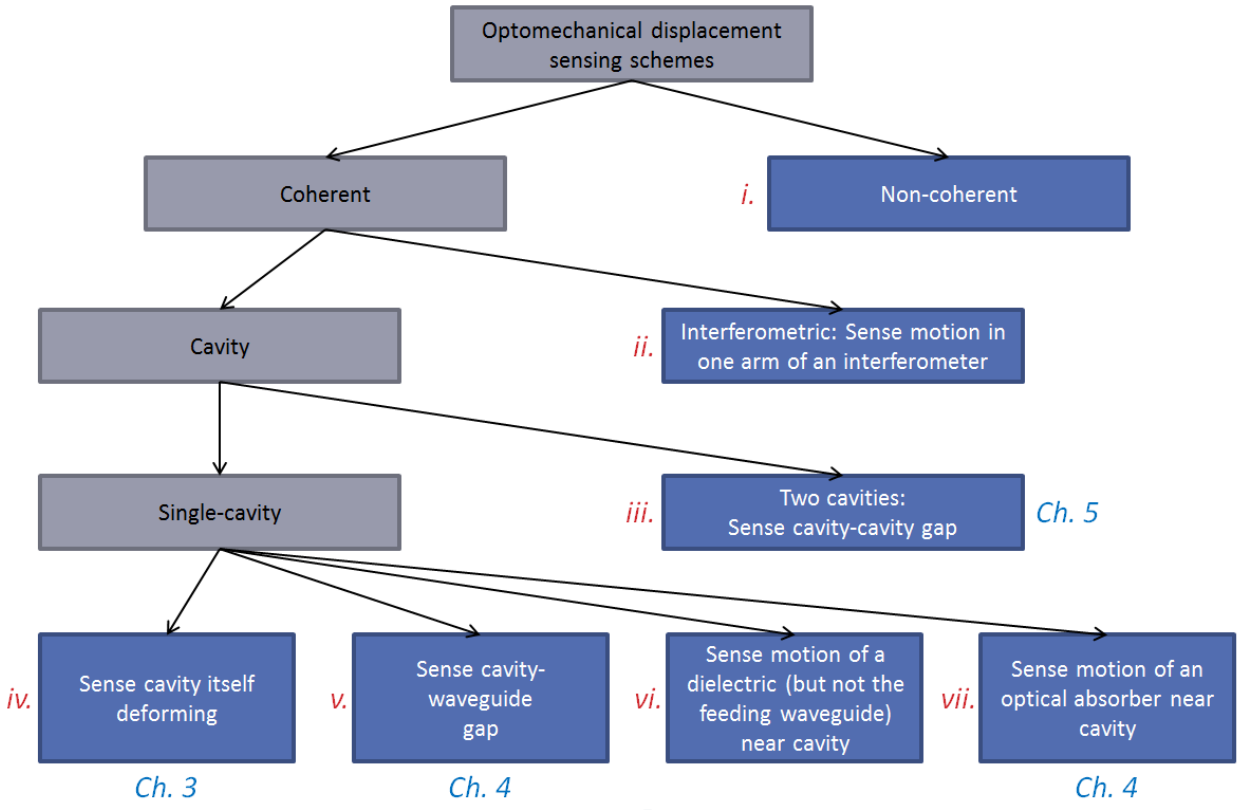

Figure 1.8

Categorization of optomechanical sensor types.

1.4.2 : Review of optomechanical displacement sensors

In Figure 1.8 we have listed the approaches to optomechanical displacement sensing. We will refer to these below as we review the approaches in the literature.

1.4.2.1 : i. Non-coherent

- ***Occluding the beam:*** Perhaps the simplest way to get optical readout of a proof mass is to have that proof mass partially occlude a beam of light, so that displacements of the proof mass are transduced into optical amplitude changes. Guildmann *et al.* use this approach in

[19] where they align two optical fibers in grooves, end-to-end with a gap between, and have a shutter in the gap that is attached to a proof mass. In a similar approach, Malki *et al.* [20] instead has one input fiber at the center of a spherical mirror, with the shutter between the two. Movements of the shutter change the amount of back-reflected light. This sensor is however highly nonlinear and since the optical mode is a few microns wide in both cases, relatively large displacements are needed to be able to transduce the motion.

- ***Misaligning the beam:*** Uttamchandani *et al.* [21] and Burcham *et al.* [22] both use the approach with two optical fibers aligned end-to-end, but one fiber is attached to a micromachined proof mass and moves out of plane, misaligning the fibers as it moves upwards or downwards. Due to symmetry however this cannot tell up from down – instead the fibers can be placed with some known initial offset so they are already misaligned by an amount to yield maximum transduction. Ollier *et al.* [23] have a similar in-plane version, but get around the symmetry problem by having one micromachined input waveguide on a cantilever, a gap, then a micromachined multimode interference device with two output waveguides. The differential signal from the two output fibers gives a linear acceleration signal. In 2009, Li *et al.* [24] demonstrated all-photonic transduction of nanocantilevers. These cantilevers were again microfabricated end-to-end as the ones in the previous bullet, and used as waveguides. As one waveguide-cantilever moved relative to the other waveguide-cantilever, the light transmitted between them changed. This device was not intended as an inertial sensor, but rather they allude (but do not demonstrate) that by differently functionalizing the cantilevers they may multiplex several molecular mass sensors on a single chip (i.e. molecules that adsorb to a functionalized cantilever would

change its resonant frequency). For their specific chosen geometry they report 40 fm/rtHz displacement sensitivity.

- The advantages of non-coherent devices include low wavelength sensitivity (high spectral quality of the light source is not required – any light source such as an LED will do), and thermal insensitivity.

1.4.2.2 : ii. Interferometric: Sense motion in one arm of an interferometer

- It may be noted that ring cavities also operate due to interference – however this "Interferometric" category refers to devices consisting of an optical interferometer. While this category could be divided in a way analogous to how we divided the "Single-cavity" category in Figure 1.6, the mechanical-based sensor experiments are few and such a division is not helpful so the division will not be made – all interferometric device types will be lumped together. Of course, many other non-mechanical sensors such as chemical sensors have been demonstrated but here we only consider ones where one arm is moved or stretched in some way.
- Li *et al.* [25] describe an experiment with an on-chip Mach-Zehnder Interferometer (MZI) where the waveguide in one arm has a released section that moves relative to the nearby underlying oxide. The sensing scheme here is primarily not by the physical motion of the waveguide itself but by the change in cross-sectional effective index as the waveguide moves in proximity to the dielectric substrate. Here they also drive the motion via optical gradient force; however it is only the sensing we are focusing on here. For the particular device geometry in that paper, they report displacement sensitivity of $18\ \mathrm{fm}/\sqrt{\mathrm{Hz}}$. It is worth mentioning here that in a separate paper they also made analogous clamped-

clamped beams as a section of an optical racetrack resonator [26] with $Q_o = 4200$ and report $40\ \mathrm{fm}/\sqrt{\mathrm{Hz}}$.

- Hallynck *et al.* [27] made interferometers where one arm of the interferometer lies over a membrane with differential pressure above and below. The bulging of the membrane and hence stretching of that arm relative to the other arm is read as an optical amplitude change at the output. In the same papers the authors compare with some rings they made, and find comparable results. This comparison however is not fully general as they only tried one ring-on-membrane geometry and one MZI-on-membrane geometry – intuitively one would expect that ring resonators can be made to have much greater transduction than MZI-based sensors. However on the other hand MZIs can show lower temperature dependence than optical ring resonators.

1.4.2.3 : iii. Two cavities: Sense cavity-cavity gap

- Wiederhecker *et al.* [15], [18] fabricated two released ring cavities from silicon nitride, stacked one on top of the other with a small gap in between. Resonant light applied a force to the cavities which caused deformation of up to 60 nm (estimated), causing the resonances to shift 32 nm, twice the optical FSR, and simulate to find $g_{OM}/2\pi = 60\ \mathrm{GHz/nm}$ for their gap size. (The quantity g_{OM} measures the optical-to-mechanical coupling and is an important quantity we will treat in Ch. 2.) Another demonstration of this by Rosenberg *et al.* using silicon dioxide cavities showed 4.2 nm (43% of the FSR) and $g_{OM}/2\pi = 31\ \mathrm{GHz/nm}$ (simulated). These stacked-cavity devices are not sensitive to inertial forces (nor were they intended to be) – since both cavities are released an acceleration would cause both cavities to deform and the gap would not change, to first order. Instead, one application is for dynamic all-optical wavelength routing.

- Some work by the present author [28] and elaborated in this dissertation, involves two stacked rings with one fixed and one free, thus being sensitive to acceleration. We simulate $g_{OM}/2\pi = 4\ \mathrm{GHz/nm}$ for our gaps.
- Krause *et al.* [7] show a design using two nearby 1D photonic crystal cavities rather than rings. By having one cavity fixed to a frame and the other attached to a proof mass on springs, they make an accelerometer. They show results consistent with $g_{OM}/2\pi = 5.5\ \mathrm{GHz/nm}$. An earlier investigation of similar cavities by the same group showed $g_{OM}/2\pi = 123\ \mathrm{GHz/nm}$ and photoreceiver-noise-limited displacement sensitivity of $0.05\ \mathrm{fm}$.

1.4.2.4 : iv. Single cavity: Sense cavity itself deforming

- Wu *et al.*[29] make an optical ring resonator attached to the clamped point of a cantilever. Acceleration causes the cantilever to bend and the ring to stretch, changing the optical resonant frequency of the ring resonator. However this is not an integrated device (instead, an optical fiber and manually-created fiber ring is glued onto a micromachined cantilever) and the optical quality factor Q_o of the ring (8,500) is orders of magnitude lower than can be easily achieved by integrated optics. A similar approach [30] using microfabrication of a polymer ring on polymer substrates used rings with $Q_o = 6200$.

  It is worth noting here that a similar approach has been used with integrated optics as a pressure sensor – A few groups [27], [31], [32] have demonstrated a microfabricated optical ring resonator (and in a different configuration, one arm of a Mach-Zehnder Interferometer) on a membrane. When there is differential pressure on the two sides of the membrane, the membrane bulges, stretching the ring (or MZI) and changing its optical resonant frequency

(or the phase in one arm of the MZI). This is detected as amplitude modulation for fixed wavelength input.

- A few groups have made on-chip free-space Fabry-Perot interferometers, with one fixed and one free mirror [33]–[35]. A laser shining down onto the cavity (which may have a photodetector fabricated beneath it), with the wavelength detuned on the side of the Fabry-Perot resonance, gives amplitude modulation as the free mirror moves. One disadvantage of this approach is that it is a complicated assembled stack of components and not all microfabricated and integrated on-chip. In the approach of Waters *et al.* (e.g. [33], [34]) there is an integrated detector, but none of the approaches have an integrated laser – instead they rely on packaging a laser on top. Integration means it would be cheaper to produce and the production process would likely be easier to control. An in-plane (waveguided) version of that has also been demonstrated by Zandi *et al.* [36] but with much poorer performance due to the difficulty of fabricating a high-finesse Fabry-Perot cavity in-plane. (The out-of-plane version is easy to fabricate by using dielectric multilayer stacks.)
- A non-integrated OM accelerometer was demonstrated by Cervantes *et al.*[37] comprised of two fibers in grooves aligned end-to-end. The ends of the fibers are coated or shaped to form mirrors, and one fiber is fixed while the other is attached to a proof mass. They report displacement sensitivities of $0.2\ \mathrm{fm}/\sqrt{\mathrm{Hz}}$.
- Another approach [38] used an optical cavity formed from a two-dimensional silicon photonic crystal, with a slot running through the cavity. As the silicon on either side of the slot moved, the cavity resonance was modified. Using a cavity with $Q_o = 1.2 \times 10^6$ they infer $g_{OM}/2\pi = 140\ \mathrm{GHz/nm}$.

- There has been a significant amount of work (e.g. [39], [40]) in the optomechanics community with the so-called "membrane-in-the-middle" approach – where a membrane (often silicon nitride) is placed in the center of a free-space Fabry-Perot cavity and its motion transduced (and possibly mechanically acted upon by the optical field). Of course this is not integrated and it is difficult to make a small-form-factor sensor out of it, but it has been important in understanding optomechanical interactions.

1.4.2.5 : v. Single cavity: Sense cavity-waveguide gap

- Mo *et al.* [41] discuss the theory behind a sensor based on a changing cavity-waveguide gap, but this approach has not been shown experimentally by any groups to the author's knowledge.

1.4.2.6 : vi. Single cavity: Sense motion of a dielectric (but not the feeding waveguide) near cavity

- Perhaps the first landmark paper in this category was by Anetsberger *et al.* [42] who took a high-quality factor melted oxide optical ring resonator on one chip, and brought a silicon nitride clamped-clamped beam on a second chip near to the resonator on the first chip. When the clamped-clamped beam was close enough to interact with the optical mode in the ring, the displacement of the clamped-clamped beam could be transduced. They used resonances with $Q_o > 10^8$ and measured up to $0.57\ \mathrm{fm}/\sqrt{\mathrm{Hz}}$.
- The next step in the progression of this category of OM devices was to integrate the clamped-clamped beam onto the same chip as the resonator. This was done by Basarir *et al.* [43] with resonances of $Q_o = 35\mathrm{k}$, reported displacement sensitivities of $10\ \mathrm{fm}/\sqrt{\mathrm{Hz}}$. However the feeding waveguide was not integrated on chip.

- Instead of a straight clamped-clamped beam as in the previous two bullet points, Srinivasan *et al.* [44]–[46] demonstrated an optical disk resonator that wraps partially around a thin dielectric beam. The advantage is that more of the mechanical element interacts with the optical field, and they use a $Q_o = 10^5$ mode to measure displacement sensitivity of $0.44\ \mathrm{fm}/\sqrt{\mathrm{Hz}}$, with simulated $g_{OM}/2\pi = 0.5{\sim}3\ \mathrm{GHz/nm}$. These devices do not have an integrated waveguide.
- An effort to integrate everything on chip and to separate the mechanics from the optics was a different approach by the same group at NIST [47], [48]. A silicon optical ring resonator was fabricated, and then a large "paddle" made from silicon nitride was fabricated on top, with some gap between. The paddle moved up and down (in fact, could be electrostatically actuated to move downwards) which changed the dielectric environment of the ring and hence the paddle's motion can be transduced using $Q_o{\sim}10^6$ with displacement sensitivities of $4.6\ \mathrm{fm}/\sqrt{\mathrm{Hz}}$.
- The same group at Caltech that we discussed in Sec. 1.4.2.3 has also created an optical cavity side-by-side with a phononic cavity, where transduction occurs with small change in the gap between the two [49], [50]. In truth the optical mode is more of a so-called "slot waveguide" mode that is confined more to the slot between the two beams – therefore it is possible to call this a Sec. 1.4.2.6 device or a Sec. 1.4.2.3 device, since whether the cavity itself "deforms" or a dielectric moves near the cavity is a matter of perspective.

1.4.2.7 : vii. Single cavity: Sense motion of an optical absorber near cavity

- The author is aware of no literature on this subject. This makes sense as it is not often that we want to bring an optically absorbing material near an optical cavity – since if we are going choose something to bring within reach of the cavity field we may intuitively choose a

dielectric instead. However the former scheme has other benefits and is treated and some experimental and theoretical results shown in Ch. 7.

Chapter 2 : Test setups and description of relevant parameters

I would rather understand one cause than be King of Persia.

-- Democritus

2.1 : Introduction

This chapter describes specific theory and experimental background necessary to understanding future chapters. These fall into two categories:

Sec. 2.2 – Description and characterization of testing setups;

Sec. 2.3 – Description of relevant parameters referred to in the text (such as the definition and a discussion of noise, etc.).

2.2 : Test setups

2.2.1 : Taper-coupled + tilt test setup

A test setup was built to couple light into an optical resonator using a tapered optical fiber, and then allow for the device to be held at arbitrary tilt, to measure gravity at arbitrary angles. This setup is shown in Figure 2.1.

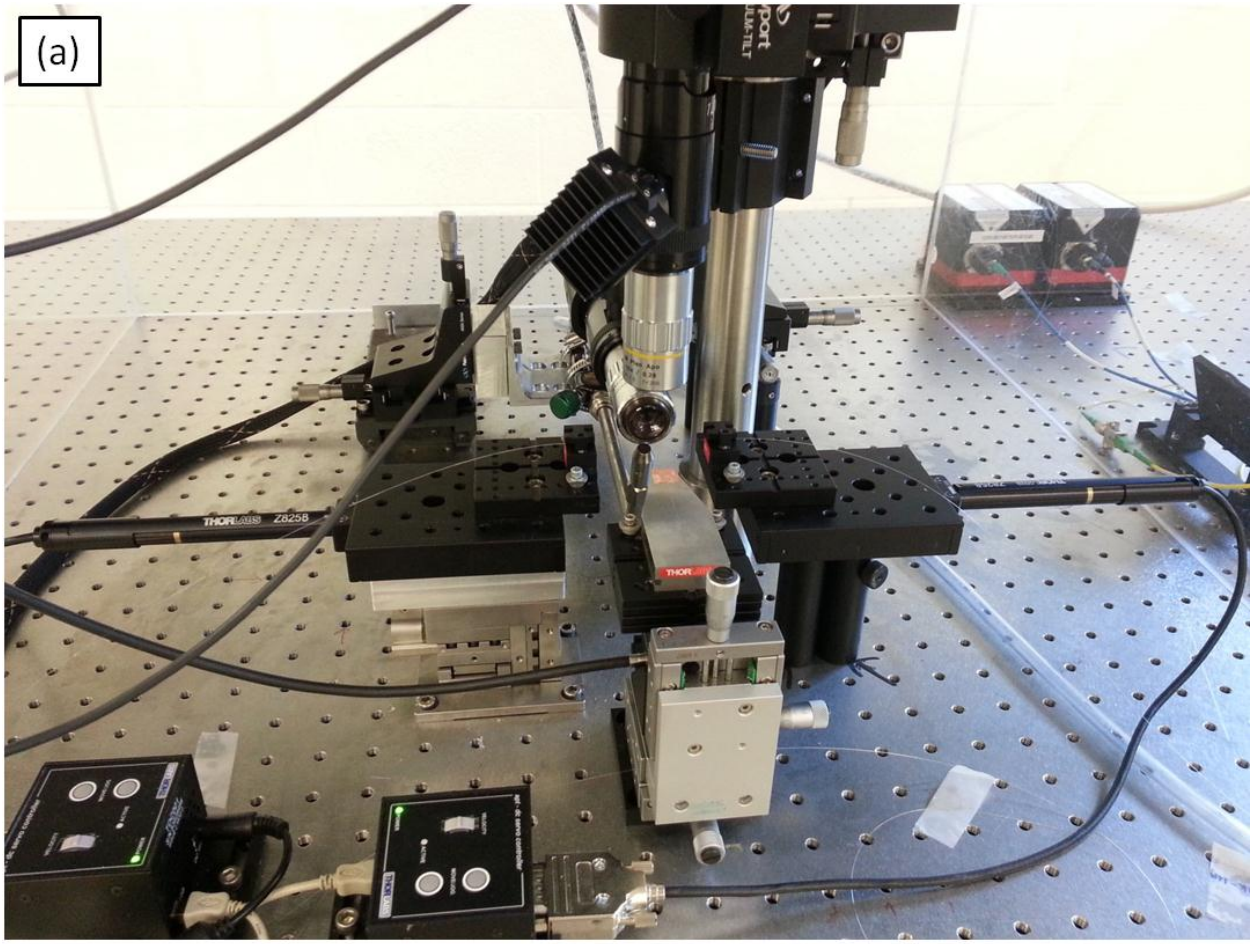
(a)
THORLABS Z825B

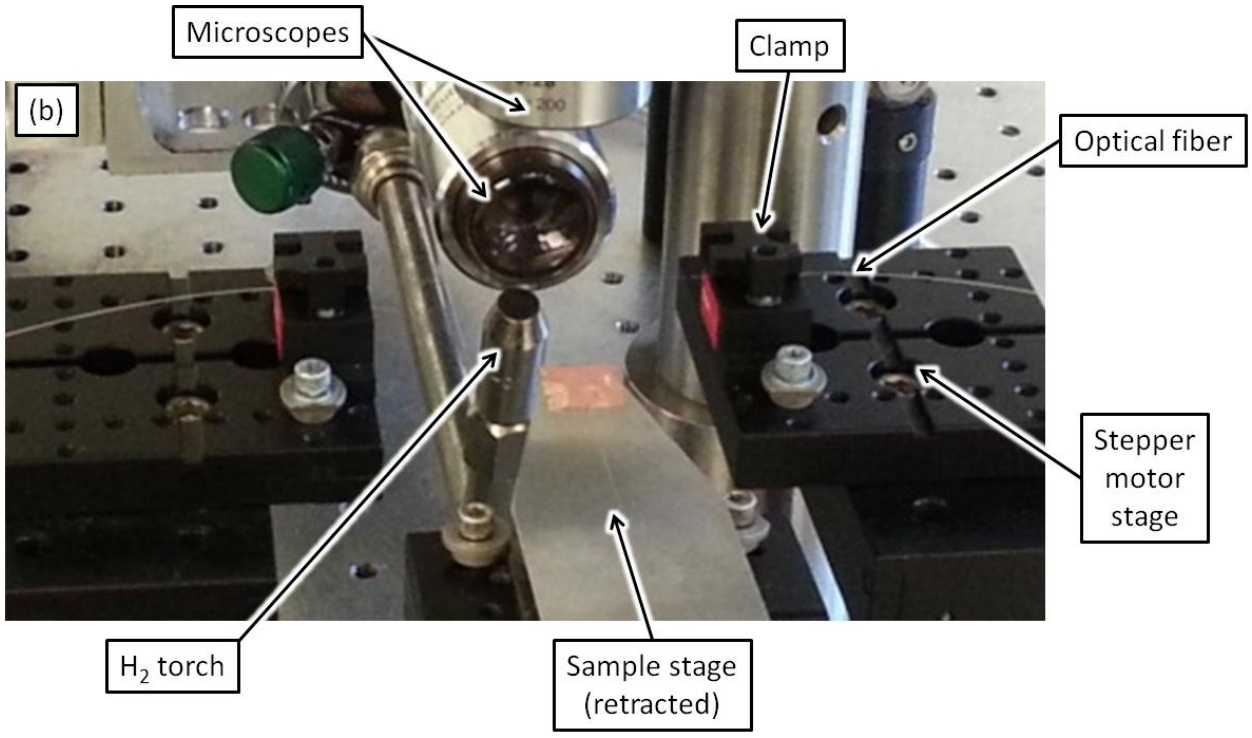

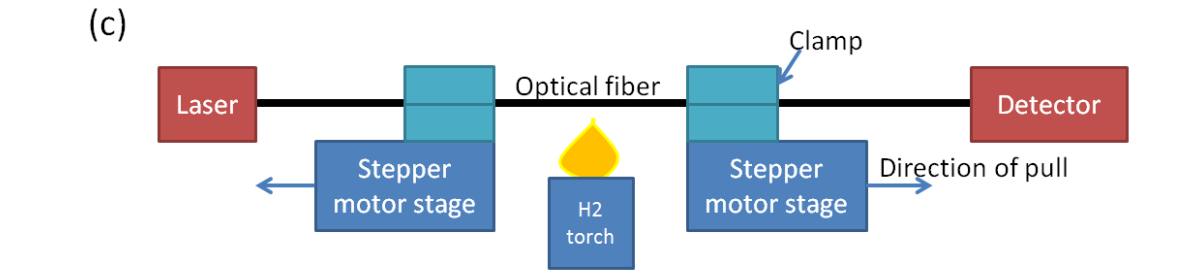

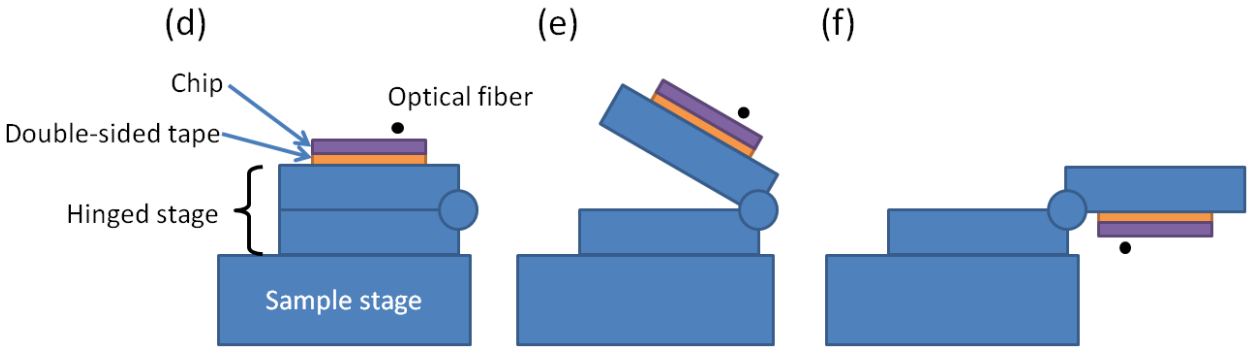

Figure 2.1

The static test setup. (a) Full view. (b) Zoom-in of taper pulling area. (c) Schematic

showing the taper pulling setup. (d)-(f) An optional attachment to the sample stage allows one to rotate the chip and thus measure the chip at any angle relative to gravity.

Figure 2.1 (a)-(c) shows the setup. The whole experiment is enclosed in a Lucite (Perspex) box which we found necessary to prevent air currents from moving the delicate pulled fiber. A hinged stage (d)-(f) allows measurement of the chip at any arbitrary tilt, useful for gravimetric measurement. The hinge is measured using a protractor to an accuracy of about 1° and held in place with friction.

The tapered fiber is pulled in the following manner. A 5cm section of SMF-28e+ optical fiber is stripped of its cladding and clamped between two motorized stages. A hydrogen torch is lit and slid under the fiber. The torch is on a quick-slide stage and an xyz micropositioner stage, so its position can be controlled accurately but then slid in and out quickly. Note that the height of this hydrogen torch is quite important and requires some optimization – we found a good location was for the fiber to be about 2mm above the tip of the barely-visible blue flame. Note also that while the torch is under the fiber, the upper microscope should be slid out of the way so the heat from the torch does not crack the lens.

At the same instant the torch is slid in under the fiber, the steppers start pulling both ends of the fiber equally (controlled by a computer which sets the acceleration rate and pull rate). A pull rate of about 0.1 mm/s was found through trial and error to produce the best results. As the fiber is being pulled, the optical spectrum is monitored on a power meter. A typical successfully-pulled fiber signal is shown in Figure 2.2.

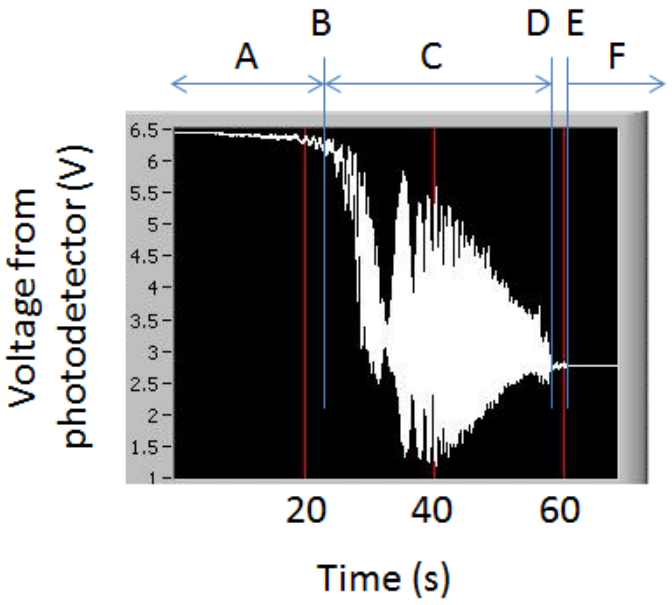

Figure 2.2

A typical signal from an optical fiber as it is being pulled. A-F are discussed in the text.

Some discussion of Figure 2.2 will highlight the relevant parts of the graph. In A, the fiber is being heated and pulled and is getting slightly narrower but not much is changing yet. At some point B, the heat reaching the doped center of the optical fiber is enough to cause the dopants to diffuse. This leads to fast oscillations in region C, as the fiber is still wide (somewhere between its starting diameter of $125\ \mu m$ and its ending diameter of about $1\ \mu m$) and the dopants diffuse throughout – effectively causing the mode to be no longer confined to its single-mode core area, but instead that section of the fiber becomes multimode. The oscillations in time seen here is due to these many higher-order modes interfering with one another as the fiber stretches and changes shape. Finally at D there is a marked decrease in these oscillations, indicating that although the dopants have diffused uniformly throughout the central portion of the fiber, now the fiber in this region is narrow enough to only support a single optical mode (actually, one each of each polarization, but we are only exciting one polarization with the

linearly-polarized laser). At this point the pulling and heat should be stopped. Here the pulling force and heat were continued for a few seconds (from D to E) to ensure the single mode condition had been reached. If it is pulled much further, the fiber will be too thin and will break. At E the pulling and heat were simultaneously stopped. Notice that between D and E, there are some oscillations, while in F there are no oscillations. This is because before E the hydrogen torch is still on and causes the fiber to shake slightly, so these oscillations go away as soon in F as soon as the torch is turned off.

When coupling to an optical resonator, for critical coupling we desire the Q-contribution from the "loading" of the cavity due to the presence of the fiber, to equal the Q-contribution from the cavity itself. The total Q we measure is

$$\frac{1}{Q_{tot}} = \frac{1}{Q_{ext}} + \frac{1}{Q_{int}} \qquad \text{Eq. 2-1}$$

where Q_{tot} is the measured (loaded) optical quality factor of the optical resonator, Q_{ext} is the Q-contribution from external loading of the cavity, Q_{int} is the intrinsic quality factor of the cavity. Since Q_{ext} depends on the waveguide-cavity gap and the effective index of both waveguide and cavity, we can tune this. The obvious way to tune it is to tune the gap – however since we are pulling a tapered fiber we can also tune the fiber's diameter to result in an effective index to match the effective index of the cavity. By pulling for longer we result in a thinner tapered fiber which results in a lower n_{eff}. In practice, however, while we had rough control over the final diameter (the largest single-mode (or nearly-single-mode) ones we pulled were about 2um diameter while the smallest ones were 0.6 um diameter), since we didn't have fine control over the diameter and since fibers would break during pulling especially for the narrower fibers, we would proceed by pulling a taper, testing it with a cavity, and if the extinction ratio of the cavity resonances (i.e. the depth of the dips in the optical spectrum) was not good enough for our purposes then we would try at a different point along the pulled fiber, which may have a different diameter, or pull a new tapered fiber.

To test optical cavities in this setup, we brought them close to the fiber taper using the sample stage shown in Figure 2.1, to couple light from the fiber into the cavity. The test setup is shown in Figure 2.3.

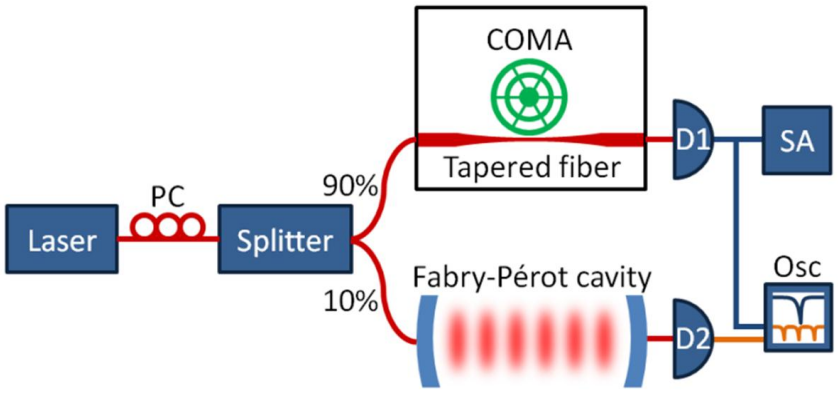

Figure 2.3

Typical test setup for optical probing of devices (a "COMA" – Cavity-enhanced OptoMechanical Accelerometer from Ch. 5) is shown here).

A tunable laser (New Focus Velocity 6324-P, fiber coupled) goes through a polarization controller (PC) and into a 90:10 splitter. The laser has fine-tuning capability which is enabled by a piezo attached to its internal grating, allowing for analog fine-tuning control of the wavelength. If we just observe an optical resonance on detector D1 while sweeping the laser wavelength back-and-forth in real time in this manner, we observe sweep-to-sweep variation in the laser wavelength of up to tens of picometers using this method, which is comparable to or much greater than the widths of the resonances reported in Ch. 4, so these dips appear to move around from sweep to sweep. Since in some cases we are interested in detecting very precise shifts in resonant wavelength, we employ a Fabry-Perot (PR) cavity to provide a frequency reference. So, the laser light is split and the majority of the light probes the device and enters detector D1, while the minority of the light enters a Fabry-Perot (FP) cavity. This cavity is a commercially-available piezo-tunable cavity with FSR of either 1.5 GHz or 10 GHz (Thorlabs SA200-12B or SA210-12B respectively), though we did not use the piezo-tuning element of it

but just used it as a fixed cavity. The detector signals are sent to a spectrum analyzer (for measurements where the laser is positioned on the side of a resonant dip) or an oscilloscope (for optical sweep measurements). For the optical sweep measurements, the wavelength of the laser is varied by sending the laser piezo a symmetrical up-down ramp voltage which allows tunability of about $100\ \mathrm{pm}$. Thus the optical response of the cavity can be monitored in real time on an oscilloscope that is synchronized to the sawtooth wave.

Note that this sweep-to-sweep wavelength variation is not from the driving voltage, which was more stable than the observed shifts, so appears to be a fundamental non-repeatability in the laser piezo drive mechanism. In other words, the piezo did not start every sweep in the same position nor end every sweep in the same position, so the wavelength scale is shifted and stretched from sweep to sweep. Nonetheless, as just mentioned, the reference cavity in Figure 2.3 gives a fixed set of fringes which forms a known background, which we use to correct (during data post-processing) for the sweep-to-sweep variation in the start and end wavelength.

2.2.2 : Vacuum test setup

The vacuum test setup is shown in Figure 2.4.

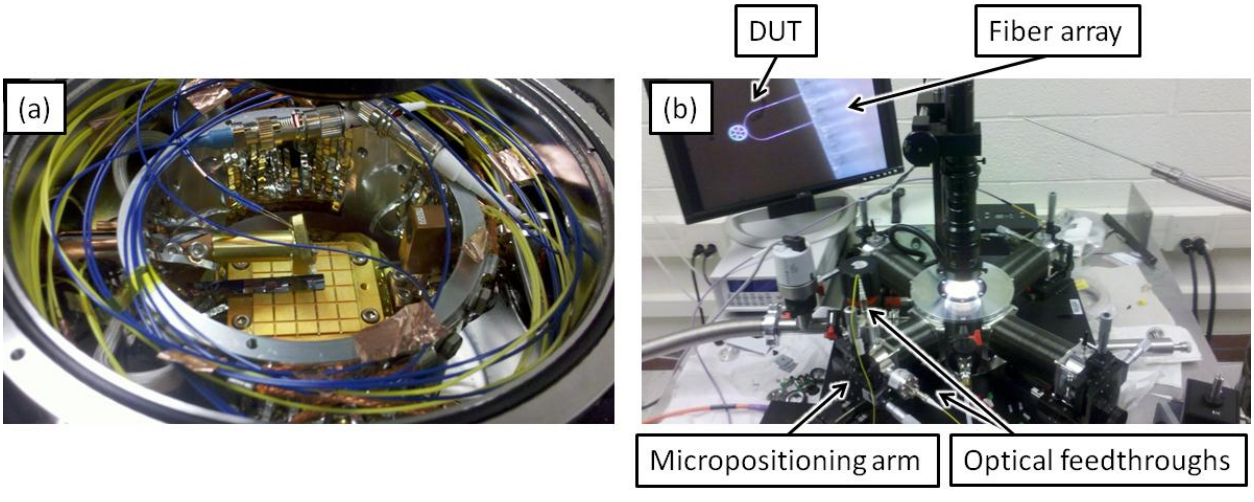

Figure 2.4

(a) View inside the chamber. The die is shown on the chuck, with a fiber array attached to the end of the micropositioning arm above it. (b) Wide view of the setup. Input and output optical feedthroughs send light into and out of the chamber.

In Figure 2.4 (b) on the screen we see a ring resonator ("DUT") with a U-shaped waveguide, and the edge of the fiber array obscuring the input and output grating couplers. This setup was used to characterize the mechanical response of the device in Ch. 6 under vacuum.

2.2.3 : Grating coupler + micromanipulator test setup

To probe devices by stretching them with a micromanipulator, we built the setup in Figure 2.5.

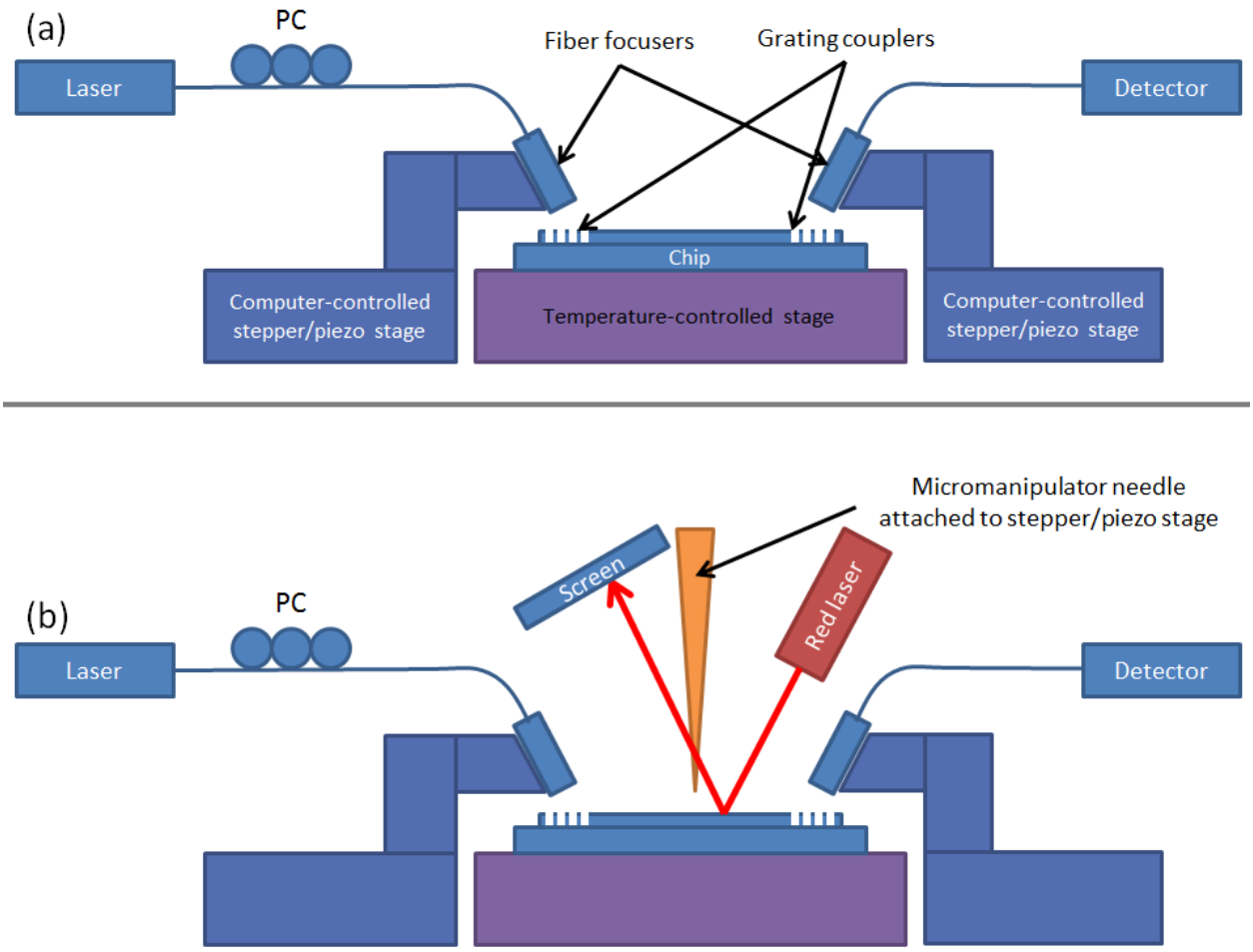

Figure 2.5

(a) Schematic showing the basic grating coupler setup. (b) Same setup also showing the optional micromanipulator needle and free-space laser position readout mechanism.

In Figure 2.5 (a) we see the basic optical coupling setup. Laser light is sent through a polarization controller (PC) and focused onto an input grating coupler using a fiber with attached lens with 3mm working distance, and collected from the output fiber in the same way. The computer controls the stepper and piezo positioning, and through repeated tests we find our coupling repeatability (i.e. how different the coupling is from one test on a device to the next test, aligned "from scratch," on the same device) to be around 1%. In Figure 2.5 (b) we have also indicated a micromanipulator needle that is

attached to a closed-loop piezo stage with electronic readout in microns. However we could not trust the position readout during our experiments for two reasons: (A) The piezo system is not necessarily correctly calibrated; (B) There is some flexibility in the micromanipulator system itself so even if the piezo readout was correct, deformation in the needle and needle arm may cause the displacement at the needle tip to be smaller. Due to this uncertainty, we use a free-space red laser to measure static deformation of the cantilevers we probed in Ch. 4. By shining the red laser onto the tip of the cantilever and collecting the laser spot on a screen (67 inches away from the chip), we can measure the displacement of the cantilever tip to within $\pm 1\ \mu\mathrm{m}$, limited by the ratio of the laser spot size to how far it moves on the screen for displacements of interest – however this was sufficient precision considering the other uncertainties in the system.

2.3 : Relevant parameters

2.3.1 : Introduction

In general the question we need to answer is, given some measured change in optical power ΔP (either static or rms), where did the signal come from? This process is depicted in Figure 2.6. We will consider each part of this diagram in the discussion below.

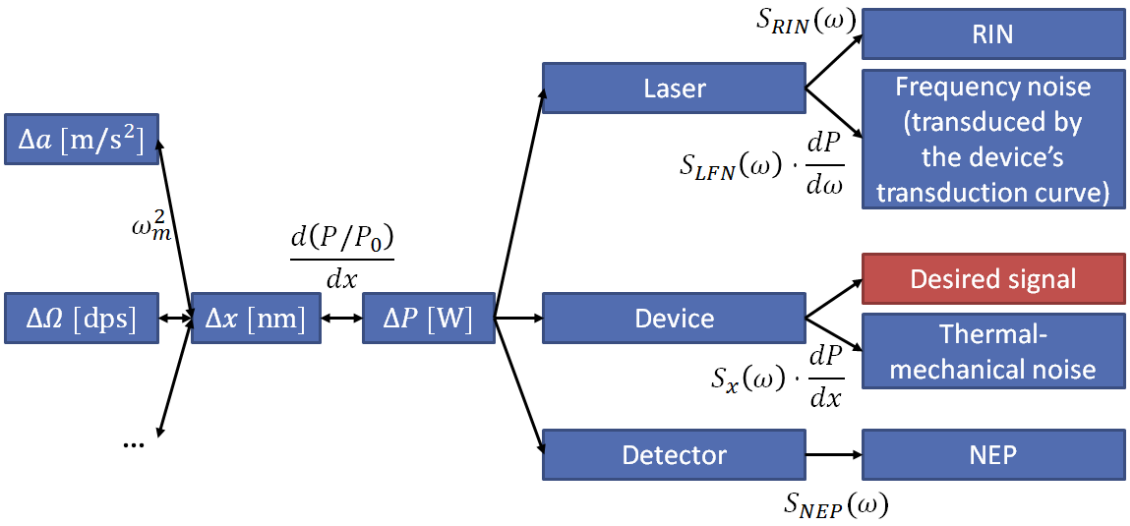

Figure 2.6

The relationship between sources of signal and noise (right-most column), and the effective measured acceleration Δa. The expressions in black text are treated in the following sections.

2.3.2 : x-to-a and x-to-Ω

Acceleration and displacement of a MEMS accelerometer proof mass are related by $ma = kx$, or

$$a = \frac{k}{m}x = \omega_m^2\, x \qquad \text{Eq. 2-2}$$

where ω_m is the mechanical resonance frequency. Note then that observing the thermal-mechanical spectrum from an accelerometer not only tells us the thermal displacement noise (if it is above the other noise levels in the system, then it will show up as a noise floor in the measurement) but also the displacement-noise to acceleration-noise conversion factor (since the scale factor is simply the resonant frequency ω_m we observe), so we may use Eq. 2-2 to convert from one to the other.

This is really just a simplification of the mass-spring-damper transfer function [51]

$$\frac{x(\omega)}{a(\omega)} = -\frac{1}{\omega_m^2 - \omega^2 + i\frac{\omega_m}{Q}\omega} \quad \text{Eq. 2-3}$$

below the resonant frequency, where a is an applied linear or Coriolis acceleration.

In the same way, for the gyroscope in Sec. 1.3.3 we find

$$x_s = -2\frac{m_2 v}{k_2}\,\Omega_v \quad \text{Eq. 2-4}$$

where m_2, k_2, and v are the mass, spring constant, and velocity of the sense mass and Ω_v is the component of the rotation vector perpendicular to both the drive motion and to the sense motion.

2.3.3 : P-to-x transduction

While other designs can be imagined, all the optomechanical sensors presented here have one detector at the output and have CW (continuous wave; fixed wavelength and power) input. The device therefore imparts an intensity modulation to the CW light, and we sense inertial forces by measuring a change in output optical power. Therefore we define a quantity $d(P/P_0)/dx$ which is the change in optical power P, normalized to the nominal power P_0, for a given displacement x. In other words, this measures the normalized optical power change due to a change in position of the proof mass, and this allows us to compare between different transduction schemes.

Note that we have used "nominal power" – by this we mean the power level at the detector around which the amplitude modulation happens. For instance, for a two-port ring resonator there is a dip in the output spectrum at a resonant wavelength. If we put some power P_{max} into the device with the laser set on the side (HWHM point) of the resonance, then our "nominal power" at the detector is $P_0 = P_{max}/2$. It makes more sense to compare signal-induced power modulation to the nominal power at the detector rather than to the input power because this allows us to compare across different approaches.

The quantity $\frac{d(P/P_0)}{dx}$ (or the more specific quantity for an accelerometer, $\frac{d(P/P_0)}{da}$) is not the same as "scale factor." Scale factor is a quantity measuring the signal output in units of volts per meter of displacement (or volts per g for an accelerometer, or volts per degree-per-second for a gyroscope). In colloquial terms, when one talks about how *sensitive* to *displacement* something is, they are usually talking about getting a large signal out from a small displacement, which indeed is what both $\frac{d(P/P_0)}{dx}$ and scale factor measure – however the distinction between the two is important. For an optomechanical sensor, scale factor would be the quantity $\frac{d(P/P_0)}{dx}$ $[\mathrm{m}^{-1}]$ (or $\frac{d(P/P_0)}{dx}$ $[g^{-1}]$) times the optical power P_0 [W] times the responsivity of the detector $\mathcal{R}$ [A/W] times the load resistance R_L [V/A] times any chosen amplifier gain G. For an electrical displacement sensor it would be the final amplified voltage signal, per m or per g. In truth, scale factor alone is rather unimportant, because if all we wanted was more volts-per-gee from an accelerometer, we could just increase G. Therefore this number is only meaningful when compared with the noise. We choose to use $\frac{d(P/P_0)}{dx}$ rather than scale factor since it doesn't assume a specific detector, load resistance, or amplifier gain.

2.3.4 : Noise

From Figure 2.6 we see that noise can come from three sources: Laser noise, device noise, and detector noise. In Ch. 6 we take the noise figures we find below, to investigate what noise level we may expect from a fully-integrated optomechanical system, and compare to state-of-the-art commercial MEMS accelerometers.

2.3.4.1 : Laser noise

Laser noise may take the form of intensity noise (RIN) or frequency noise. Both are spectral quantities which we will call $S_{RIN}(\omega)$ and $S_{LFN}(\omega)$ respectively. For on-chip lasers such as would be needed in integrated optomechanical sensors, extremely low RIN is achievable – for example Tanaka *et*

al. [52] report a high output power, single wavelength silicon hybrid flip-chip laser with RIN around -130 dB/Hz when it is fiber-coupled, but that number falls to around -150 dB/Hz for the non-fiber-coupled version for GHz frequencies, and appears to go down to -160 dB/Hz for the deep-sub-GHz frequency range of interest for optomechanical sensors – though this could be an artifact of electrical filters used, and it is unclear whether this is measurement-limited. The increase in RIN when the laser was fiber-connectorized may be due to mode competition in that configuration, back-reflections, or other effects, but since in the devices presented here the light never needs to leave the chip this may be a promising result. Assuming the RIN numbers quoted are referenced to the carrier (dBc) and assuming for this experiment (as in their other experiments in this paper) they were using $\sim 10\ \mathrm{mW}$ CW output, we may take the three values quoted above to actually be -120 dBm/Hz, -140 dBm/Hz, -150 dBm/Hz respectively. Of course this is a spectral quantity but when we use this number in Ch. 6 to project the optomechanical SNR, for simplicity we can take it to be a constant for a frequency range of interest.

Frequency noise (or equivalently, phase noise) of the laser gives the laser a finite linewidth, and manifests itself as amplitude noise on the detector only when transduced by a device, for example, when the laser wavelength is positioned on the steep side of a cavity resonance (so, this applies to the devices in Ch. 3 and Ch. 5 but not Ch. 4). If the frequency noise spectrum is S_{LFN} (measured in $\mathrm{Hz}/\sqrt{\mathrm{Hz}}$ — that is, the frequency noise per root-Hz of bandwidth) then multiplying this spectral quantity by the slope of the cavity resonance in $\mathrm{mW/Hz}$ gives the resulting amplitude noise spectrum (measured in $\mathrm{mW}/\sqrt{\mathrm{Hz}}$ — milliwatts of optical power per $\sqrt{\mathrm{Hz}}$ of bandwidth, which may be converted to $\mathrm{dBm/Hz}$ – that is, dBm of optical power per Hz bandwidth, so after such multiplication this has the same units as S_{RIN}).

A review of the literature reveals that frequency noise often has $1/f$ dependence at the low frequencies of interest to us and then becomes flat, but for purposes of having concrete numbers to use

later, we may read off the value at a frequency of 100 Hz, a relevant frequency for inertial sensors (actually, even lower frequencies are often relevant but results in the literature don't often take data at much lower frequencies). The author is not aware of any reported frequency noise measurements for on-chip lasers but for DBR or DFB fiber lasers a typical value may be taken to be 2×10^2 Hz/$\sqrt{\text{Hz}}$ (e.g. [53]) or 1.6×10^3 Hz/$\sqrt{\text{Hz}}$ (e.g. [54]).

2.3.4.2 : Device (thermal-mechanical) noise

Thermal-mechanical noise is due to the mechanical energy stored in the device at finite temperature T. It too is a spectral quantity, the square root of the PSD being

$$S_x(\omega) = \sqrt{\frac{4k_B T \omega_m}{m Q_m}} \sqrt{\frac{1}{\left(1 - \frac{\omega^2}{\omega_m^2}\right)^2 + \frac{1}{Q_m^2}\frac{\omega^2}{\omega_m^2}}} \qquad \text{Eq. 2-5}$$

where k_B is the Boltzmann constant, T is temperature, and m, Q_m, and ω_m are the mass, mechanical quality factor, and mechanical resonant frequency respectively. Since we are often interested in the response below the resonant frequency (for example, accelerometers operate below their resonant frequency), the noise is a constant in this range:

$$S_x(\omega) = \sqrt{\frac{4k_B T}{m Q_m \omega_m^3}} \qquad \text{below } \omega = \omega_m \qquad \text{Eq. 2-6}$$

It is also useful to express this in terms of acceleration noise, for when we apply this to accelerometers:

$$S_a(\omega) = \sqrt{\frac{4k_B T \omega_m}{m Q_m}} \qquad \text{below } \omega = \omega_m \qquad \text{Eq. 2-7}$$

For example, the XY iPhone accelerometer shown in Figure 1.7 may have:

- Mass of roughly 10 micrograms (based on its measured size from that microscope image, times an estimated fill factor of ~ 0.7 since it's full of release holes and comb fingers)

- Resonant frequency of 10 kHz (estimate based on 1kHz maximum data rate quoted in datasheet – the resonant frequency would need to be several times the maximum data rate, and usual consumer electronics accelerometer resonant frequencies may be around 10 kHz)

This leads to a noise floor of $0.3\ \mu g/\sqrt{\text{Hz}}$ if the mechanical quality factor is 10,000, and $S_a = 3\ \mu g/\sqrt{\text{Hz}}$ if the mechanical quality factor is 100. The datasheet lists the accelerometer noise as $218\ \mu g/\sqrt{\text{Hz}}$, which is two or three orders of magnitude larger! It is immediately obvious that the noise is probably not thermal-mechanical-limited but rather in the driving circuitry. Even if we did make expensive, low-noise circuitry for an accelerometer and found we were thermal-mechanical noise limited, we simply increase the mass of the device until we are again electronic-noise limited. In other words, it's a lot easier to reduce thermal-mechanical noise than it is to reduce electronic noise, therefore in practical accelerometers, thermal-mechanical noise is not a problem since it can always be designed to be equal to or better than the electronic noise.

The optical power fluctuation we'd observe from this noise is

$$S_{x,opt}\left[\frac{\text{W}}{\sqrt{\text{Hz}}}\right] = (P_0[\text{W}])\left(\frac{d(P/P_0)}{dx}[\text{m}^{-1}]\right)\left(S_x\left[\frac{\text{m}}{\sqrt{\text{Hz}}}\right]\right) \qquad \text{Eq. 2-8}$$

where $\frac{d(P/P_0)}{dx}$ was discussed in Sec. 2.3.3, and we have written out the units for clarity.

2.3.4.3 : Detector noise

The noise-equivalent power (NEP) for a detector is also a spectral quantity, but is usually taken as a constant around the frequency range of interest. NEP is usually quoted on the datasheet for commercial detectors, but since we are ultimately interested in on-chip photodetectors we may like investigate by assuming some typical values from waveguide-coupled on-chip detectors the literature. For example DeRose *et al.* report a waveguide-based Ge photodiode at telecom wavelengths with

$S_{NEP} \approx 10^{-14}\ \mathrm{W}/\sqrt{\mathrm{Hz}}$ [55]. In general we may assume a "good" detector to have $S_{NEP} \approx 10^{-12}$ to $10^{-14}\ \mathrm{W}/\sqrt{\mathrm{Hz}}$, approximately constant for all frequencies.

We may use such NEP figures as-is, however we wish to raise what may be an important point. This noise figure and most figures for such on-chip photodiodes assume the photodiode is operating in photoconductive (PC) mode (i.e. reverse bias and measure photocurrent), as opposed to photovoltaic (PV) mode (zero applied bias). As discussed at the end of Sec. 1.3.4, it may be advantageous to operate an on-chip photodiode in PV mode instead to take advantage of higher SNR and since the bandwidth in PV mode is still more than sufficient for OM displacement sensors.

Unfortunately we have been unable to find papers reporting waveguide-based photodetector operating at telecom wavelengths in *PV mode*. However some Schottky photodiode PV-mode detectors at shorter wavelengths have shown NEP figures of -142 dBm/Hz [56], and in general we expect better noise figures for PV mode compared to PC mode.

2.3.5 : g_{OM}

Central to most of the optomechanical literature today is the optomechanical coupling coefficient g_{OM}. This measures how the resonant frequency shifts for a given displacement x, measured in $\mathrm{GHz/nm}$:

$$g_{OM} \equiv \frac{d\omega_o}{dx} \qquad \text{Eq. 2-9}$$

Of course, this only applies in transduction schemes where the resonant frequency shift is the thing being sensed, such as in Ch. 3 and Ch. 5 (but not in Ch. 4). This is, however, the most common transduction scheme in optomechanics literature so it is an important quantity in the literature. In this dissertation, however, since we are also considering other transduction schemes such as in Ch. 4, we

primarily use the more relevant and useful $\frac{d(P/P_0)}{dx}$ as described in Sec. 2.3.3. (But when relevant this can be converted to g_{OM} as we show later using Eq. 5-6.)

Chapter 3 : Single-cavity mechanical deformation sensing

We measure things. We spend countless dull hours measuring the swing of a pendulum, the heat of an acid, the twitch of a muscle. But only with these measurements in hand can we begin our dialogue with the Cosmos. -- Anonymous

3.1 : Introduction

A two-port ring resonator is shown in Figure 3.1 (a).

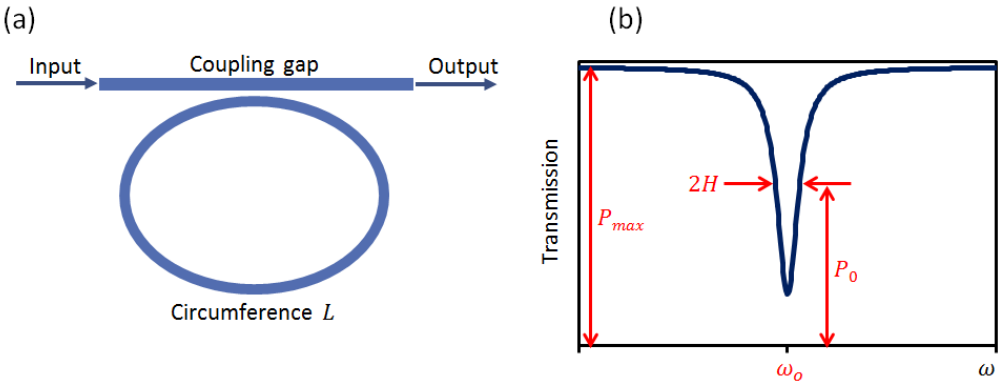

Figure 3.1

(a) A two-port ring resonator. (b) On resonance there is a dip in the optical transmission spectrum. The HWHM is H and the transmitted power at the transduction point is P_0, which is at a frequency of $\omega_s = \omega_o \pm H$.

When the following equation is true:

$$m\lambda = n_{eff}L \qquad \text{Eq. 3-1}$$

for integer m, then the wavelength in the ring λ/n_{eff} fits an integer number of times around the ring circumference L, light is resonant in the ring, and we observe a dip in the output spectrum as shown in Figure 3.1 (b). This dip is due to losses in the ring, and also partially to the light coupled out of the ring

destructively interfering with the light remaining in the waveguide. Such a dip is Lorentzian in frequency (and nearly Lorentzian in the wavelength domain too, since $2H \ll \omega_o$). The equation for a Lorentzian is

$$P(\omega) = P_{max} - \frac{D}{1 + \left(\frac{\omega - \omega_o}{H}\right)^2} \qquad \text{Eq. 3-2}$$

where $D = 2(P_{max} - P_0)$ is the depth of the dip.

Upon deformation of a ring resonator, we expect the wavelength resonant frequency to shift by [29]

$$\frac{\Delta\lambda_o}{\lambda_o} = \frac{\Delta L}{L} + \frac{\Delta n_{eff}}{n_{eff}} \qquad \text{Eq. 3-3}$$

(This may be intuitively obvious, but we will derive this from first principles in Sec. 3.4.3, since for the device described there, some modification of this equation is necessary.) The first term on the right of Eq. 3-3 is the physical length-change (strain) effect and the second term on the right is the stress-optical effect (which changes the cross-sectional effective index around the ring). In Sec. 3.4 we revisit this for a particular device geometry we made and tested, and show that for the particular device described there, the former term dominates the latter.

3.1.1 : Physical length-change effects

Now, we find from Eq. 3-3 for fixed n_{eff}, when the circumference changes by ΔL, the resonant wavelength λ_o shifts by $\Delta\lambda_o$, according to

$$\frac{\Delta L}{L} = \frac{\Delta\lambda_o}{\lambda_o} \approx \frac{\Delta\omega_o}{\omega_o} \qquad \text{Eq. 3-4}$$

Next we assume we are operating at a frequency halfway down the Lorentzian in Figure 3.1 (b), $\omega_s = \omega_o \pm H$. By differentiating Eq. 3-2 and evaluating at this point we find the slope to be

$$\left.\frac{dP}{d\omega}\right|_{\omega_{ss}} = \pm\frac{D}{2H} = \pm\frac{P_{max} - P_0}{H} \qquad \text{Eq. 3-5}$$

We consider only the positive sign. Combining Eq. 3-4 and Eq. 3-5 we find the expected power modulation at ω_{ss} due to circumference change to be

$$\Delta P = \frac{dP}{d\omega}\Delta\omega_o = \frac{(P_{max} - P_0)}{H}\frac{\omega_o}{L}\Delta L \qquad \text{Eq. 3-6}$$

Thus by knowing the properties of the Lorentzian and measuring the power modulation ΔP we know how much the circumference is changing ΔL, and thus what displacement sensitivity we have. Lastly we assume critical coupling, so $P_{max} = 2P_0$, and express this a different way which will be useful later:

$$\frac{d(P/P_0)}{dL} = \frac{\omega_o}{LH} = \frac{2Q_o}{L} \qquad \text{Eq. 3-7}$$

To investigate further, we made some silica microtoroids and used the tapered fiber setup described in Ch. 2 to optically probe their thermal-mechanical motion, reported in Sec. 3.2 and 3.3. Secondly we made integrated silicon racetrack resonators on-chip and statically deformed them using a different test setup described in Ch. 2 to probe their response, as reported in Sec. 3.4.

3.1.2 : Photoelastic (stress-optical) effects

Even non-birefringent materials such as those used here can exhibit birefringence when stress is applied – this phenomenon is known as the photoelastic effect. For example in Sec. 3.4 we consider a rib waveguide being stretched by an underlying cantilever. Since we are considering just one mode – TE mode in this case – we can just consider the stress tensor S_{kl} to have an effect on the bulk index $n(x, y, z, S_{kl})$ at each point x, y, z in the waveguide, which leads to an effect on the effective index $n_{eff}(x, y, z, S_{kl})$.

More generally, the linear stress-optical relation can be written as [57]

$$\Delta n_{ij} = -B_{ijkl}S_{kl} \qquad \text{Eq. 3-8}$$

where $\Delta n_{ij} = n_{ij} - n_0 I_{ij}$ is the bulk refractive index tensor, n_0 is the bulk refractive index in absence of stress, I_{ij} is the identity tensor, B_{ijkl} is the stress-optical tensor, and S_{kl} is the stress tensor. Assuming the nondiagonal parts of n_{ij} are negligible, we may simplify this to

$$\begin{bmatrix} \Delta n_x \\ \Delta n_y \\ \Delta n_z \end{bmatrix} = - \begin{bmatrix} B_1 & B_2 & B_2 \\ B_2 & B_1 & B_2 \\ B_2 & B_2 & B_1 \end{bmatrix} \begin{bmatrix} S_x \\ S_y \\ S_z \end{bmatrix} \quad \text{Eq. 3-9}$$

where we have also assumed only two independent parameters B_1 and B_2, similar to [57]. We simplify this further in Sec. 3.4.3.

It is difficult to exactly simulate photoelastic effects on the microtoroids described next in this chapter and we do not do so. However in Sec. 3.4 we revisit this to show that at least for the much easier-to-solve case for a racetrack resonator stretched by an underlying cantilever, the resonant frequency change is dominated by the physical length change, so the effect of photoelasticity is small.

3.2 : Microtoroids: Fabrication

Our first testbed of choice was a silica microtoroid because it is a high-Q_o ring resonator that we can fabricate in large numbers on a silicon chip. Although we tested several devices, for sake of clarity here, all results are from one device. The fabrication process and results are shown in Figure 3.2.

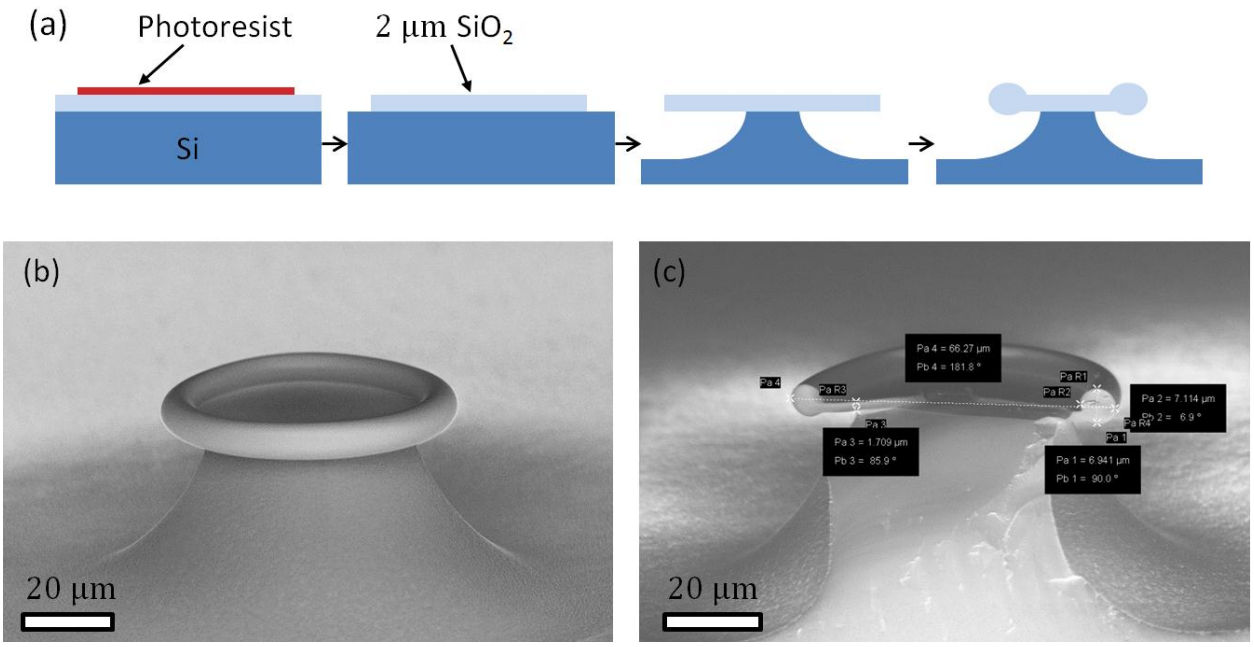

Figure 3.2

(a) The fabrication process to make silica microtoroids, described in the text. (b) An SEM image of the microtoroid used in this work with diameter of 62.5 μm. (b) A different microtoroid in cross-section showing the rounded rim more clearly, with measurements showing the size of the microtoroid rim.

To make the silica disk we start with a commercially-available 4" Si wafer with 2 μm of thermally-grown SiO_2. We use photoresist to pattern and reactive ion etching to etch circular disks with radius 100 μm. We then use a XeF_2 etch to undercut the disks so they sit on a pedestal about 40-45 μm diameter. Lastly, we melt the disks to form microtoroids. To do this we put the chip in a laser cutting tool (Versalaser VLS3.50) at maximum power (50 W at wavelength of 10.6 μm) and raster scan across the surface of the entire chip; this melts all microtoroids on the chip. However since the spot size of the Versalaser CO_2 laser is slightly smaller than our starting silica disk diameter, in order to get uniform melting we intentionally defocus the laser by moving the sample stage away from the focus point by about 15 mm. This spreads the laser spot out, ensuring good uniformity. The melting process is mostly

self-limiting so that once it has melted to a size where the toroid overhangs the pedestal by about 15 μm, additional time under the melting laser appears to melt it slowly, if at all. This appears to be due to the laser-generated heat applied to the silica disk being in steady state with the outflow of heat through the silicon pedestal (silicon has a higher thermal conductivity than silica). The microtoroids can only be melted more by using significantly more laser power (which, since we are already using the full available power, can only be done by bringing the chip close to the focus of the laser spot).

3.3 : Microtoroids: Thermal-mechanical motion

A typical optical resonance is shown in Figure 3.3 (a) and the mechanical spectrum observed on an electrical spectrum analyzer when biased at the point of greatest transduction is shown in (b).

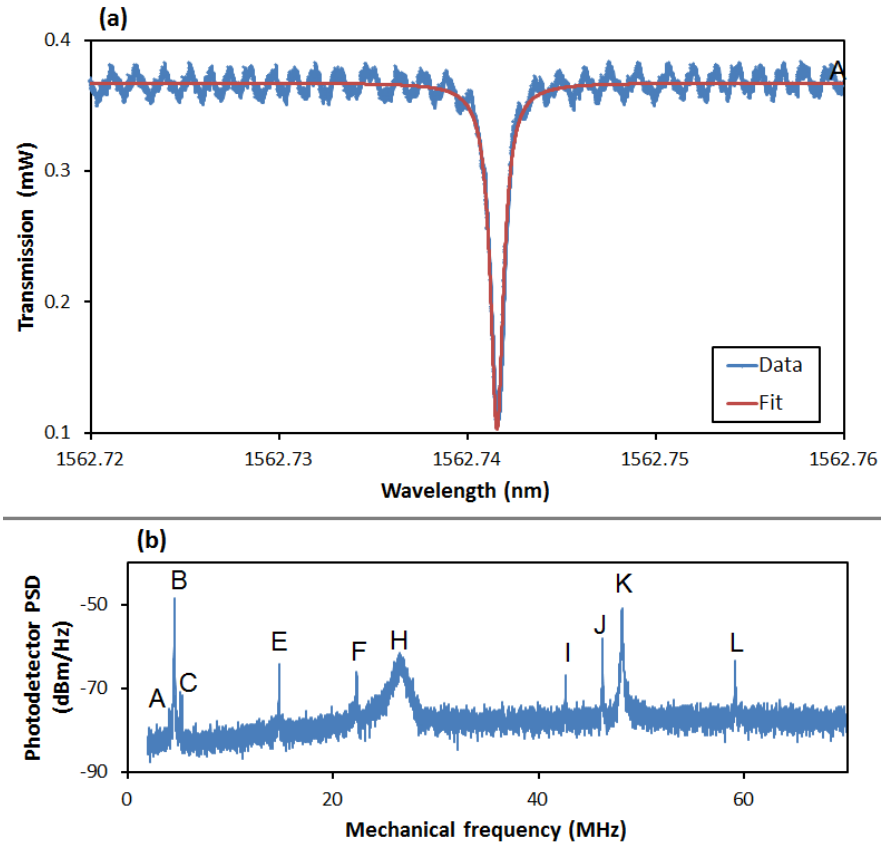

Figure 3.3

(a) Optical spectrum and fit of a typical microtoroid optical resonance with $Q_o \approx 1.9\ M$. (b) Mechanical spectrum obtained from biasing the laser on the side of the optical resonance and feeding the signal directly into an electrical spectrum analyzer. Letters A to L are referred to in Table 3.1.

As shown in Figure 3.3 (b), a rich spectrum of mechanical modes is observed. There are no higher-frequency modes observed beyond the 70 MHz range shown in Figure 3.3, and the detector bandwidth is 125 MHz (New Focus 1811). The properties and mode-shapes of main observed mechanical modes are shown in Table 3.1.

Mode name	**Measured freq. (MHz)**	**Q_m (from Lorentzian fit)**	**Peak height ($\frac{\mathbf{dB}}{\mathbf{Hz}}$, from Lor. fit)**	**Mechanical mode (from FEM)**	**Simulated freq. (MHz, from FEM)**	**Sim. freq. ÷ Meas. freq.**
A	4.46	-	-	Flapping with 2 nodes 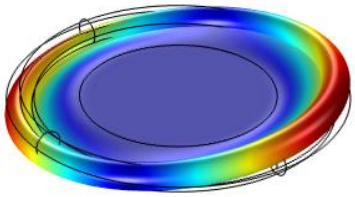	4.11	92%
B	4.55	330	-47	Flapping with 0 nodes 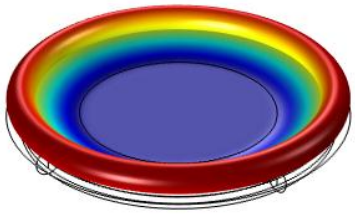	4.39	96%
C	5.10	500	-66	Flapping with 4 nodes 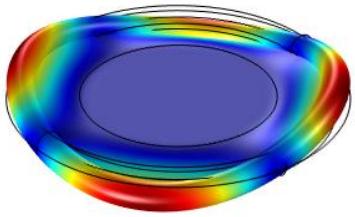	4.85	95%
D	-	-	-	Flapping with 6 nodes	8.32	-

				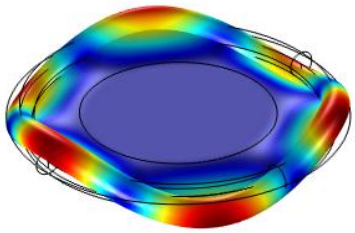		
E	14.74	480	-65	Flapping with 8 nodes 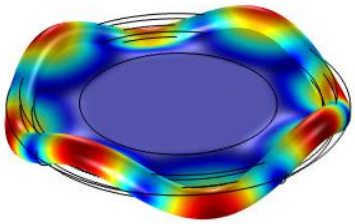	14.0	95%
F	22.29	200	-68	Flapping with 10 nodes 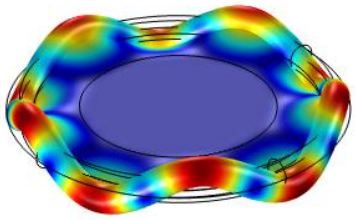	21.3	96%
G	-	-	-	Twisting 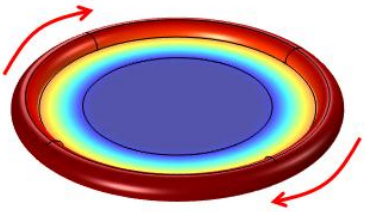	22.2	-
H	26.53	24	-64	Breathing with 0 nodes 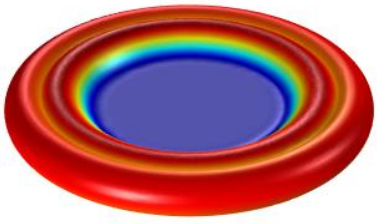	26.7	100%
I	42.62	1400	-68	Breathing with 4 nodes 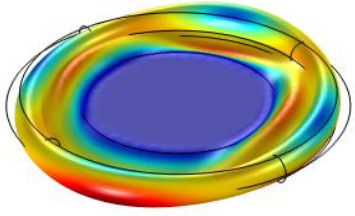	43.4	102%

J	46.20	1400	-58	Breathing with 8 nodes 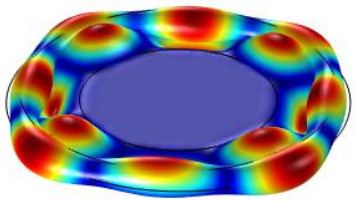	47.8	103%
K	48.09	720	-51	Different breathing with 0 nodes 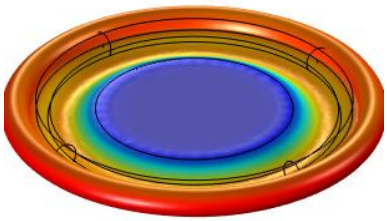	51.1	106%
L	59.08	1100	-64	Different breathing with 4 nodes 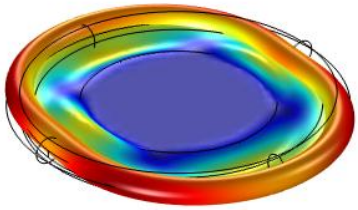	58.7	99%

Table 3.1

The mechanical modes from Figure 3.3 (b), matched with COMSOL simulations. We describe the modes with rim motion primarily out-of-plane as "flapping" and primarily in-plane as "breathing." The right-most column is the best-effort simulated frequencies based on SEM measurements of the geometry.

A few features of Figure 3.3 and Table 3.1 are interesting to note. The modes where the circumference moves primarily radially (rather than out-of-plane) have generally large amplitude but smaller mechanical quality factor. Mode G is missing, but this is to be expected since such twisting motion results in very little radial motion. However, curiously Mode D is also missing from the measured spectrum while Modes E and F (which are similar to Mode D but which we may expect to have smaller amplitude) are present. Furthermore, the simulated mode eigenfrequencies are a few percent off.

While this is a good demonstration of optomechanical effects and displacement sensitivity, it inherently lacks rigor in many ways:

I. **Uncertainty in knowledge of exact geometry of this particular device:** A best-effort simulation identifies the mechanical modes but the match is always a few percent off, even when varying the parameters slightly around the measured values to account for uncertainties in geometrical measurement.

II. **Geometrical simplifications:** For practical reasons, we simulate an axisymmetric geometry while the actual device is not perfectly axisymmetric. This is due to the XeF_2 etch not being perfectly axisymmetric (leading to a slightly squarish shape of the anchor, and the slightly squarish shape of the anchor also leads to a slightly squarish shape at the melted rim).

III. **Device-to-device geometrical variation:** Although not evident here, far from being precisely (e.g. lithographically) defined, each device is very different in nominal dimensions. Also the rim is not always perfectly uniform, but can have slight bulges around its perimeter, which can vary from device to device due to a XeF_2 etch that is inherently nonuniform across the die and the nature of the CO_2 laser melting procedure.

IV. **The simulation only gives the mechanical mode-shapes and eigenfrequencies** while the actual spectrum also includes peak height and peak width information. Peak width (mechanical damping) for such devices has been shown to be anchor-loss limited [58] and is inherently very difficult to simulate accurately, and matching the observed peak heights (getting the exact circumferential length change using FEM eigenmode analysis) is also difficult or impossible. This is because the eigenmode solver simply solves for the eigenmodes without regard for the amplitude of each. While we could make some amplitude analyses assuming equipartition of energy between the eigenmodes, it is still

difficult to measure the exact optical path around the deformed resonator in FEM, which is the circumference we are interested in.

To summarize the last few points: In general we are looking for a subtle effect from a small length change on a curvy deformed path around a round (actually, not perfectly round) resonator, all of which make exact FEM circumferential length analysis difficult or impossible. It is therefore difficult to have a perfect knowledge of the system, and thus difficult to explain the measured data perfectly.

3.4 : Stretching a racetrack resonator

3.4.1 : Fabrication and simulation

As just described, using thermal-mechanical motion in microtoroids to test for cavity length change has the disadvantage that we can't always fully explain all data with fitted simulation data. Most people resort to hand-waving at this point, as the experiment qualitatively (or semi-quantitatively) matches what is expected, which may be good enough. However without the chance to exactly match theory to experiment, we are still limited in being able to test the underlying physics. It is worthwhile to probe a more well-controlled system. Secondly, we choose to probe the more well-controlled system described below because we can use it to make an optomechanical accelerometer or gyroscope.

To this end we fabricated an integrated Si racetrack resonator in an SOI wafer and mechanically stretched the ring using a micromanipulator. Since the racetrack was microfabricated, we have an exact known geometry and waveguide cross-section. Since we are stretching the racetrack using a micromanipulator and measuring the exact deformation using a free-space laser reflected off the cantilever (described in Ch. 2), we have an exact known deformation. This allows us to experimentally probe a more controlled system. This device can be used as an accelerometer (though, we do not shake the device to demonstrate this, due to the difficulty of shaking the chip with precisely-aligned coupling optics) or perhaps even in a gyroscope or other MEMS sensors.

The fabrication process is shown in Figure 3.4 and the test setup is shown in Figure 2.5.

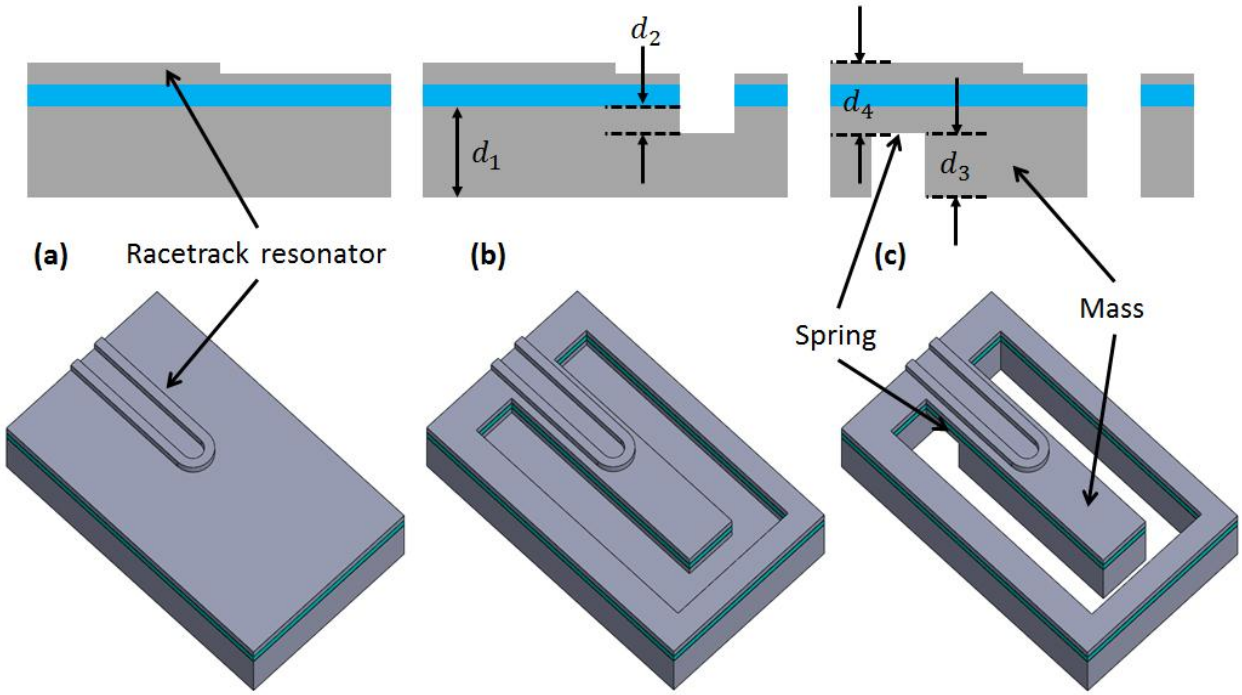

Figure 3.4

The fabrication process for the racetrack resonator on cantilever. (a) The device layer of an SOI wafer is etched to form a rib waveguide racetrack resonator (only half of which is depicted here – the full racetrack resonator is shown in Figure 3.5). (b) The top silicon (grey), buried oxide (cyan), and underlying Si (grey) is etched to depth d_2. (c) The back side is etched to a depth $d_3 \approx d_1 - d_2$.

We first etch the racetrack resonator, then etch a cantilever shape from the top side through the buried oxide and to an additional depth d_2 into the handle wafer. Lastly we etch from the back side, and stop when $d_3 \approx d_1 - d_2$. The total spring thickness is then d_4. By stopping when our top and bottom etch holes meet each other, we ensure the handle-wafer-part of the spring has thickness of about d_2 (perhaps a little less if there is overetching, but this is measured post-fabrication using the

calibrated z-scale on a microscope), therefore we have control over the spring thickness, and we can also easily see when the etch is done.

To make a very soft spring we could etch all the way to the buried oxide in the final step. However we find that built-in stress in the oxide layer causes the spring area to ripple and crack if d_2 is less than a few microns. For the experimental results presented here, $d_2 = 20\ \mu\text{m}$.

The racetrack resonator is shown in Figure 3.5 (a), and its TE mode is shown in (b). We excite only the TE mode by using a single-mode waveguide, and by sending in light through grating couplers that selectively couple only TE light.

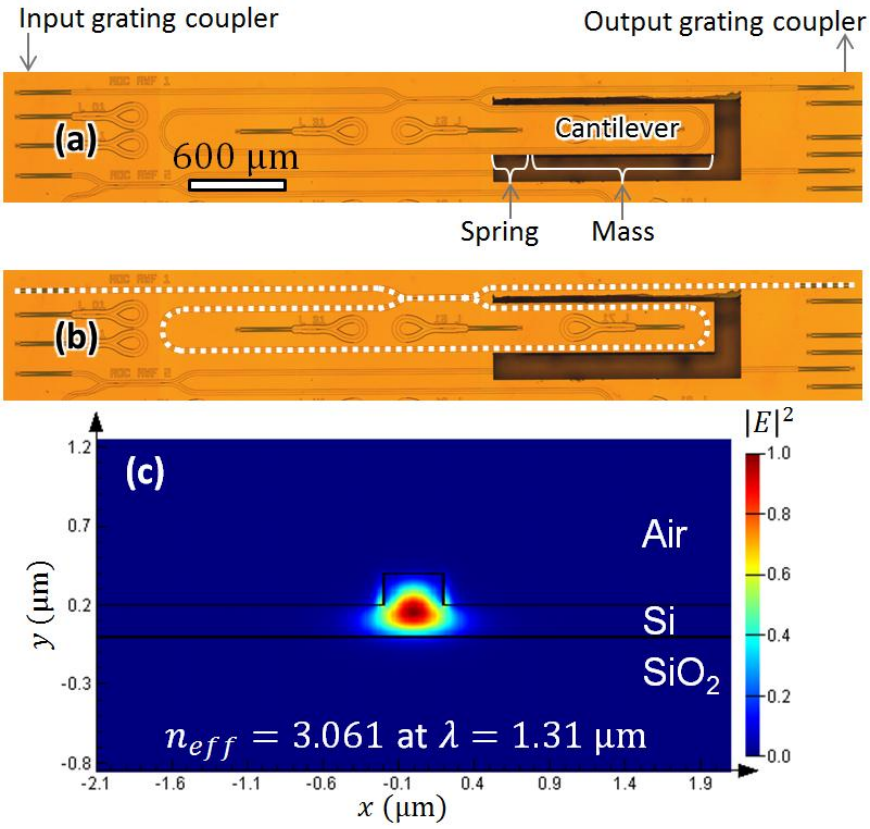

Figure 3.5

(a) Stitched microscope images showing the racetrack resonator. The rough cut around the top part of the cantilever trench was due to needing to manually

screen that part with UV-opaque material during lithography in order to protect the waveguide, but should not affect performance since the cantilever outline is still lithographically defined. (b) The same image with the ring resonator highlighted with a dotted white line for clarity. (c) FEM simulation showing the TE mode used here, and its effective index.

The physical length change is easy to simulate and account for and is shown in the next section. After that we consider the photoelastic effect to see how it compares.

3.4.2 : Physical length-change revisited

We simulated the cantilever with spring thickness varying from 20 to 5 microns (the actual thickness is 20 microns, measured by focusing the image of the aperture-stop of an optical microscope first on the wafer back side and then on the spring back side and measuring the difference on the calibrated microscope z-scale – knowing the wafer thickness the spring thickness can then be deduced), but is not perfectly uniform and it is difficult to get an exact measurement, and we'd like to use a thinner spring in the future so we simulate this case). The resonant wavelength shift due to physical length-change alone can then be calculated using Eq. 3-4. Simulation results are shown in Figure 3.6.

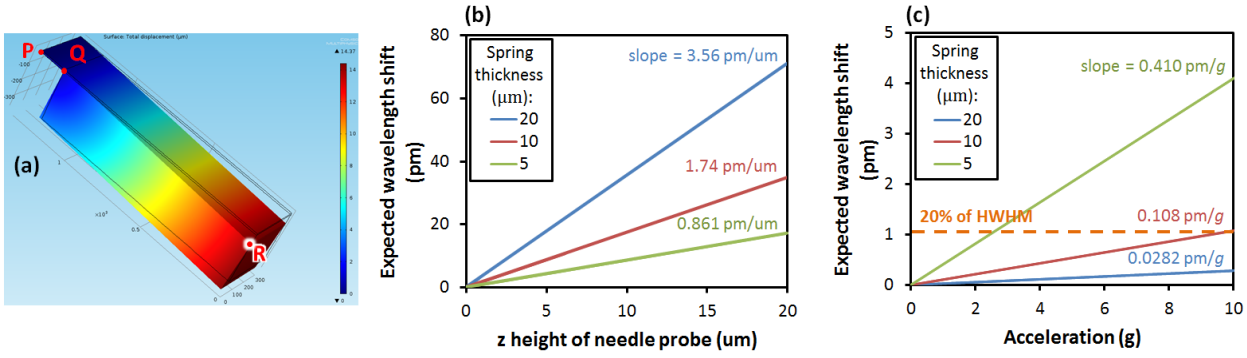

Figure 3.6

(a) FEM model showing the cantilever with 14um of vertical deformation at the

tip. P,Q, R, are discussed in the text. (b) For acceleration corresponding to a known deformation at the point the needle was contacting ("z height of needle probe") and three spring thicknesses, we find these expected resonant frequency shifts. The thicker spring shows more ring-stretching for the same deformation as expected (it is thicker, so the top surface stretches more for the same deformation), but it must be remembered that it is more difficult to deform a thicker spring. The slope of each line is written beside the line. (c) The effect of acceleration on the resonant frequency. For transduction we desire to stay in the linear region of the Lorentzian dip, so a "20% of HWHM" line is shown for scale.

In the FEM model postprocessing, to measure the physical length change of the deformed ring resonator, we integrate and double the length change from P to R in Figure 3.6 (a) (doubled since the waveguide runs along the spring twice). Of course most of the length change happens from P to Q, but we integrate all the way to R to capture any additional length change near Q (between Q and R) that wouldn't be captured if we just integrated from P to Q.

If the laser wavelength is set on the steep side of the transmission dip, then the normalized output power change per unit of acceleration is

$$\frac{d(P/P_0)}{da} = \frac{1}{P_0}\frac{dP}{d\lambda}\frac{d\lambda}{da} \qquad \text{Eq. 3-10}$$

where we know $d\lambda/da$ from Figure 3.6. We find $dP/d\lambda$ by taking the derivative of a Lorentzian at the HWHM point for a critically-coupled ring with input power P_{max} and a HWHM of H, to find $\frac{dP}{d\lambda} = \frac{P_{max}}{2H}$, which for the power halfway down the dip of $P_0 = P_{max}/2$ and writing in terms of optical quality factor we get $\frac{dP}{d\lambda} = \frac{2P_0Q_o}{\lambda_o}$. Thus Eq. 3-12 becomes

$$\frac{d(P/P_0)}{da} = \frac{2Q_o}{\lambda_o}\left(\frac{d\lambda}{da}\right) \qquad \text{Eq. 3-11}$$

For example, from Figure 3.6 (c) for the $20\ \mu m$ thick spring or the $5\ \mu m$ thick spring respectively, we get $\frac{d\lambda}{da}$ of 0.0282 or $0.410\ pm/g$ respectively. Using this in Eq. 3-12 gives

$$\frac{d(P/P_0)}{da} = 0.0056\ g^{-1} \quad \text{or} \quad 0.081\ g^{-1} \qquad \text{Eq. 3-12}$$

respectively.

3.4.3 : Photoelastic effect revisited

In this section we first re-derive Eq. 3-3 for this device, and then show that the length-change effect dominates the photoelastic effect.

Rewriting Eq. 3-1 to include both a "stretched" portion L_S of the ring circumference and a fixed portion L_F (and the effective indices in those two regions $n_{eff,S}$ and $n_{eff,F}$ respectively), and indicating the terms that depend on cantilever displacement x explicitly, we get

$$m\lambda_o(x) = n_{eff,S}(x)\ L_S(x) + n_{eff,F}L_F \qquad \text{Eq. 3-13}$$

We take the x-derivative of Eq. 3-1 to get:

$$m\frac{d\lambda_o}{dx} = n_{eff,S}\frac{dL_S}{dx} + \frac{dn_{eff,S}}{dx}L_S \qquad \text{Eq. 3-14}$$

which leads to the dependency

$$m\ \Delta\lambda_o = n_{eff,S}\ \Delta L_S + \Delta n_{eff,S}\ L_S \qquad \text{Eq. 3-15}$$

Dividing Eq. 3-12 by Eq. 3-1 gives

$$\frac{\Delta\lambda_o}{\lambda_o} = \frac{n_{eff,S}\Delta L_S}{n_{eff}L} + \frac{\Delta n_{eff,S}L_S}{n_{eff}L} \qquad \text{Eq. 3-16}$$

Now we note that the length change in the stretched portion of the spring is the total spring length change $\Delta L_S = \Delta L$, the effective index change in the stretched portion is exactly the effective

index change we called Δn_{eff} before, and that $\Delta n_{eff,S}$ is small so $n_{eff,S} \approx n_{eff}$. Therefore Eq. 3-16 simplifies to

$$\frac{\Delta\lambda_o}{\lambda_o} = \frac{\Delta L}{L} + \frac{\Delta n_{eff}}{n_{eff}} \frac{L_S}{L} \qquad \text{Eq. 3-17}$$

This equation intuitively makes sense – the resonant frequency shift has a contribution from the total circumferential length change and another contribution from the photoelastic effect – but the latter only applies to the portion of the circumference that is being stretched (L_S/L). We are now ready to compare the relative effects of the two terms on the right of Eq. 3-17 (so, we are comparing the magnitude of the physical-length change effect to the photoelastic effect). If the strain at the top surface of the cantilever is $\epsilon = \frac{\Delta L}{L}$, which we assume for this ballpark calculation to be its constant average value over the "spring" part of the cantilever and zero elsewhere, and the stress is only in the vertical direction (the direction the cantilever is bending, which we will call the z direction), then $S_{x,y} = 0$ and so we are interested in S_z (using the notation from Sec. 3.1.2). Furthermore, since we are using TE mode, the electric field is primarily aligned parallel to the cantilever surface (which we will call x). So we are primarily interested in Δn_x, the change in bulk index seen by the x-component of the electric field (the major component of the TE mode). This means we can simplify Eq. 3-9 to find the change in bulk index Δn of the waveguide as

$$\Delta n \approx \Delta n_x \approx -B_2 S_z = -B_2 Y \epsilon \qquad \text{Eq. 3-18}$$

where Y is Young's modulus for the silicon spring. Lastly we note that if we simulate the optical eigenmode in the waveguide and slightly change the bulk index n_x by a small amount Δn_x, the mode shape doesn't change much and so the solved effective index will also change by a linearly proportional amount Δn_{eff}, that is to say: $\frac{\Delta n_{eff}}{n_{eff}} = \frac{\Delta n_x}{n_x}$ for small Δn_x. Now we can compare the ratio of the two terms on the right of Eq. 3-17 to find

$$\text{ratio } R = \frac{\left(\frac{\Delta n_{eff}}{n_{eff}}\right)\left(\frac{L_S}{L}\right)}{\left(\frac{\Delta L}{L}\right)} \approx \frac{\left(\frac{\Delta n_x}{n_x}\right)\left(\frac{L_S}{L}\right)}{\left(\frac{\Delta L}{L}\right)} = \frac{\left(-\frac{B_2 Y \epsilon}{n_x}\right)\left(\frac{L_S}{L}\right)}{\epsilon}$$

$$= \frac{-B_2 Y}{n_x}\left(\frac{L_S}{L}\right) \qquad \text{Eq. 3-19}$$

$$\approx \frac{-(4.2 \times 10^{-12}\ [\text{Pa}^{-1}])(170 \times 10^{9}\ [\text{Pa}])}{3.4}\left(\frac{2 \times 100\ \mu\text{m}}{7000\ \mu\text{m}}\right)$$

$$\approx -0.01$$

where we use B_2 and Y from [57] and the well-known bulk index of silicon at 1310nm, and L_S is twice the length of the cantilever spring since the waveguide runs over that spring twice. So for this device, Eq. 3-19 shows we may expect the photoelastic effect contribution to be about 100 times smaller than the physical length-change effect, and due to the minus sign we expect the two effects to act in opposition to each other – in other words, the measured $\Delta\lambda/\lambda$ will be about 99% of its value calculated from physical length-change alone. Thus we see that this is a negligible effect. To write Eq. 3-17 in terms of R, the fractional resonant wavelength shift is

$$\frac{\Delta\lambda_o}{\lambda_o} \approx \frac{\Delta L}{L}(1 + R) \qquad \text{Eq. 3-20}$$

3.4.4 : Experimental results

We couple light into the ring and observe a resonances in the spectrum with optical quality factor of about 130,000. The spectrum is monitored as the micromanipulator stretches the ring. The results are shown in Figure 3.7.

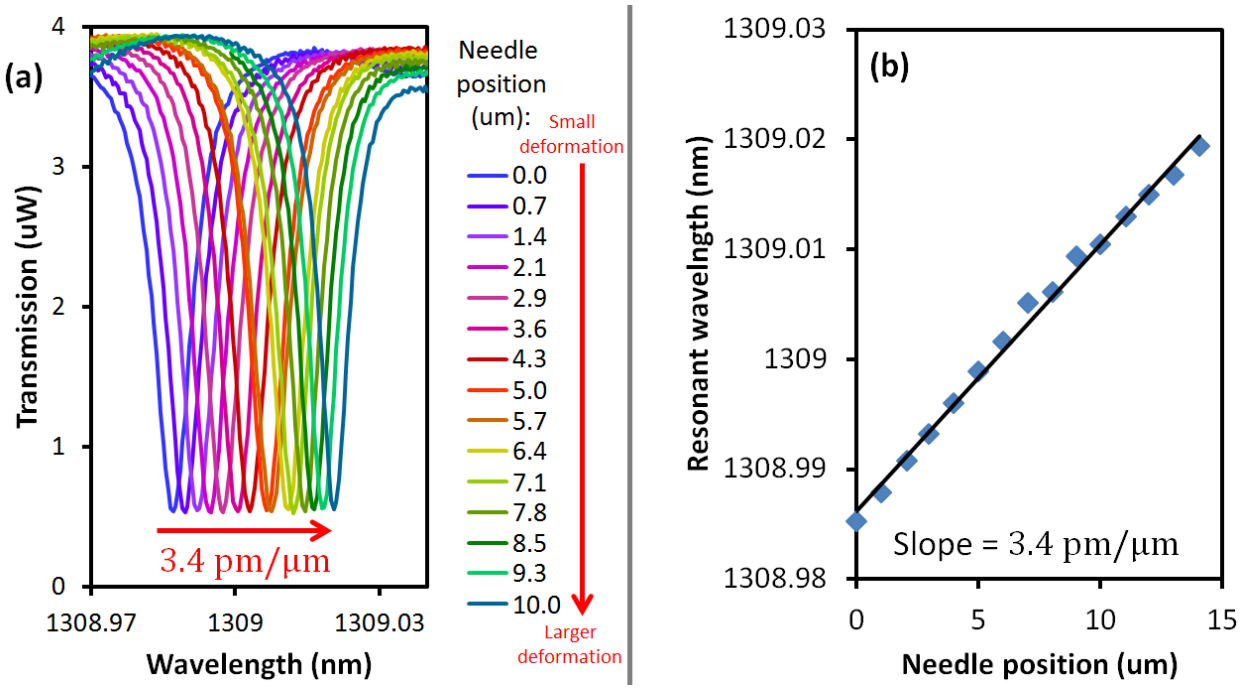

Figure 3.7

(a) Optical spectrum of racetrack resonator as the cantilever tip is deformed by a needle probe. (b) Center wavelength from (a) versus needle probe position.

The slope extracted from Figure 3.7 (b) is $3.4\ \mathrm{pm/\mu m}$. To compare our theory to this observed slope, it is simplest to just simulate the physical length-change in COMSOL (i.e. not simulate the photoelastic effect since we showed it was small).

From the simulations in Figure 3.6 we find that the slope for the $20\ \mu\mathrm{m}$ thick spring is $3.56\ \mathrm{pm}$ of optical wavelength change per micrometer of tip displacement, which correlates reasonably well with the measured $3.4\ \mathrm{pm/\mu m}$ from Figure 3.7. The discrepancy is probably mostly due to the uncertainty in the spring thickness, spring thickness uniformity, and the exact wavelength scale in Figure 3.7 (which we take from the laser's specifications sheet but did not verify ourselves).

We were unable to measure the thermal-mechanical noise of the device by using an electrical spectrum analyzer on the photodetector output, mostly due to the high in-coupling and out-coupling

losses (the grating couplers had insertion loss of about 13 dB each – if using an on-chip laser and detector, we would have much more signal available). However we expect this noise to be very small anyway – using Eq. 2-7 with the known cantilever geometry and assuming Q_m of 100, 1,000, and 10,000 respectively, we calculate thermal-mechanical noise of 206, 65, and 21 $\mathrm{ng}/\sqrt{\mathrm{Hz}}$ respectively, due to the relatively huge mass and soft spring. This is a small number, considering that the (primarily electrical) noise of typical commercial MEMS accelerometers may be $\sim 100\ \mu g/\sqrt{\mathrm{Hz}}$.

Lastly we consider the other noise sources. Unfortunately we have not measured the laser RIN or frequency noise but we assume the same reasonable numbers as we chose in Sec. 2.3.4.3 ($S_{RIN} = -130\ \mathrm{dB/Hz}$, $S_{LFN} = 2e2\ \mathrm{Hz}/\sqrt{\mathrm{Hz}}$ at 100 Hz) to get a ballpark understanding of the noise level. We find through FEM that the fundamental mechanical eigenfrequency for the 20, 10, and 5 μm-thick spring is 6.3, 2.2, and 0.80 kHz respectively. The optical quality factor was 130k, P_0 at the detector was $2\ \mu\mathrm{W}$, and the noise of the New Focus 1811 detector is $S_{NEP} = 2.5\ \mathrm{pW}/\sqrt{\mathrm{Hz}}$ (from the datasheet). Using these numbers in Eq. 6-2 we get non-thermal-mechanical acceleration noise $a_n = 390\ \mu g/\sqrt{\mathrm{Hz}}$. This rather large noise is dominated by the photodetector noise (good photodetectors may have noise floor of $0.01 - 1\ \mathrm{pW}/\sqrt{\mathrm{Hz}}$ as discussed in Sec. 2.3.4.3) and the fact that P_0 is small due to the grating coupler losses. While there were a lot of assumptions go into this calculation it at least gives us a sense of the noise to expect, and can only get better with the orders-of-magnitude more power available from an integrated laser and the potentially much lower-noise detectors available when using a custom-engineered on-chip detector. In light of this, it is not surprising we cannot detect the thermal-mechanical noise (the thermal-mechanical background may be much smaller than the other noise sources, but even the thermal-mechanical resonant peak which is amplified by a factor of Q_m above the background, may still be too small to detect above the other noise sources).

In the future, less massive and higher ω_m devices can be made to be able to detect the thermal-mechanical motion in air if desired.

3.4.5 : Future improvements

The device presented here is not optimized. Considering our analytical model, we see that to increase its performance as an accelerometer by potentially several orders of magnitude in the future, we can consider the following:

- Make the spring as long and thin (i.e. soft) as possible. The spring cannot be made too long or thin though, or it will turn out buckled or cracked after fabrication due to stress mismatch between its the SiO_2 and Si parts, or it will break under large accelerations, or it will lower the mechanical resonant frequency too far for a fixed mass, so there is a tradeoff.
- Make the mass as large as possible if this is to be used for an accelerometer or gyroscope. However, larger mass takes up more footprint which can increase air damping.
- Make the ring circumference L as small as possible so that $\Delta L/L$ is large. The ring still needs to be long enough to run back and forth over the spring, though.
- Make the ring as high-Q_o as possible by reducing waveguide loss (while remaining near critical coupling to take advantage of a steep transduction slope).
- Operate slightly undercoupled for a steeper transduction slope. Through a ballpark calculation knowing the waveguide loss and coupler efficiency we believe we are operating in the slightly-overcoupled regime. In the future we can test this by making more rings (these rings were just some we didn't design but that just were available for us to use).
- There are ways to reduce the photoelastic cancellation effect too (e.g., use TM mode rather than TE mode. Then Eq. 3-18 becomes $\Delta n \approx -B_1 Y \epsilon$ and B_1 is about ten times smaller than

B_2 for this material system [57], or else use a different material with a smaller B_2), but since this effect is small this does not help much for the geometries presented here.

- Use a shorter wavelength to increase the effect, however it is convenient to operate at telecommunication wavelengths.

3.5 : Conclusions

In conclusion we showed ultra-sensitive mechanical transduction using a high-Q_o resonator, and more rigorous results using a lower-Q_o stretched ring, and fit our results with models and simulations. For the second set of experiments the photoelastic effect was considered and it was found that physical length change is much larger effect for that device. The measured wavelength shift for a known displacement matches well with calculated shift from simulated length-change and calculated photoelastic effect.

We also briefly described how the stretched ring can be used as an accelerometer if it can be integrated with an on-chip laser and detector and investigated its thermal-mechanical noise level. It could also be used as a gyroscope if it resides within an outer mechanical resonator, similar to Figure 1.4, with the outer resonator driven in-plane at its resonant frequency ω_m and with the cantilever resonant frequency also at ω_m for maximum Coriolis acceleration transduction. However we have not yet demonstrated either application as we have not yet fabricated an on-chip laser attached to such a device. Without an on-chip laser we rely on precise x,y,z positioning at the input and output couplers, and even gluing on fibers attached to an off-chip laser and detector can be problematic as the fibers can bend and flex, resulting in undesired signal. So, this is preliminary work to investigate the device alone and in the future such a device with on-chip laser will be explored.

Chapter 4 : Single-cavity evanescent-field optomechanical sensing

Equations are more important to me, because politics is for the present,

but an equation is something for eternity.

-- Albert Einstein (when declining the office of president of Israel)

4.1 : Introduction and general approach

In this chapter we consider experimentally and by simulation, two cases:

Sec. 4.2.1 and 4.3 – An *optical absorber moving* in the evanescent field of a microsphere optical cavity.

Sec. 4.2.2 and 4.4 – The *waveguide itself moving*, changing the coupling to a microtoroid optical cavity.

A third case of single-cavity evanescent-field optomechanical sensing has been described in detail elsewhere [42]–[48]. This system, by Kippenberg *et al.*, Basarir *et al.*, and with two further embodiments by Srinivasan *et al.* involves a dielectric (but not the feeding waveguide) moving in the near field of a microdisk resonator. This dielectric is designed to not tap light out of the resonator, due to being too small to support significant optical modes, or a lower index, or both – instead it is designed to simply change the effective index around the ring, changing the path length and thus the resonant frequency. This is a very effective method, especially for high-Q_o cavities, but has been considered in detail elsewhere so we do not consider it here (though it is closely related to the two-cavity device in Ch. 6).

Returning to the two cases we are considering, the goal is to seek understanding for how the cavity evanescent field can be used to sense a moving element (an optical absorber in the first case, and the waveguide itself in the second case) in these configurations. One can imagine an application, for

example, where the waveguide is attached to a proof mass and moves relative to the cavity when subject to acceleration. We seek to compare between these approaches and understand, when the laser is biased onto a point of the cavity resonance, what is the maximum signal transduction $\frac{d(P/P_0)}{dx}$ we can hope to achieve in each case. Of course, the answer to that will be dependent on a variety of parameters such as the evanescent decay rate of a chosen optical mode, the optical quality factor, etc., but nonetheless we seek to draw some general conclusions from this analysis.

4.2 : Transduction regime

Now, firstly it is important to note that this is not the "usual" way of single-cavity optomechanical displacement sensing – the "usual" way in the literature being either deformation of the cavity or sensing motion of a nearby dielectric that causes the resonant frequency to shift (as described briefly in the previous section). In both of these other approaches, the laser wavelength is set on the side of a resonance and we monitor how optical intensity changes as the resonant wavelength shifts. When the cavity linewidth is narrow, the transduction slope is steep and this can result in an extremely effective transduction tool. Why, then, should we consider the alternate approaches in this chapter when these other approaches are extremely sensitive and successful? First let's consider the transduction schemes in more detail, then we will be in a position to offer justification for investigating them.

The general spectral behavior when the waveguide-cavity gap changes is shown in Figure 4.1 (a), and the general behavior of an optical absorber moving in the evanescent field of a cavity is shown in (b).

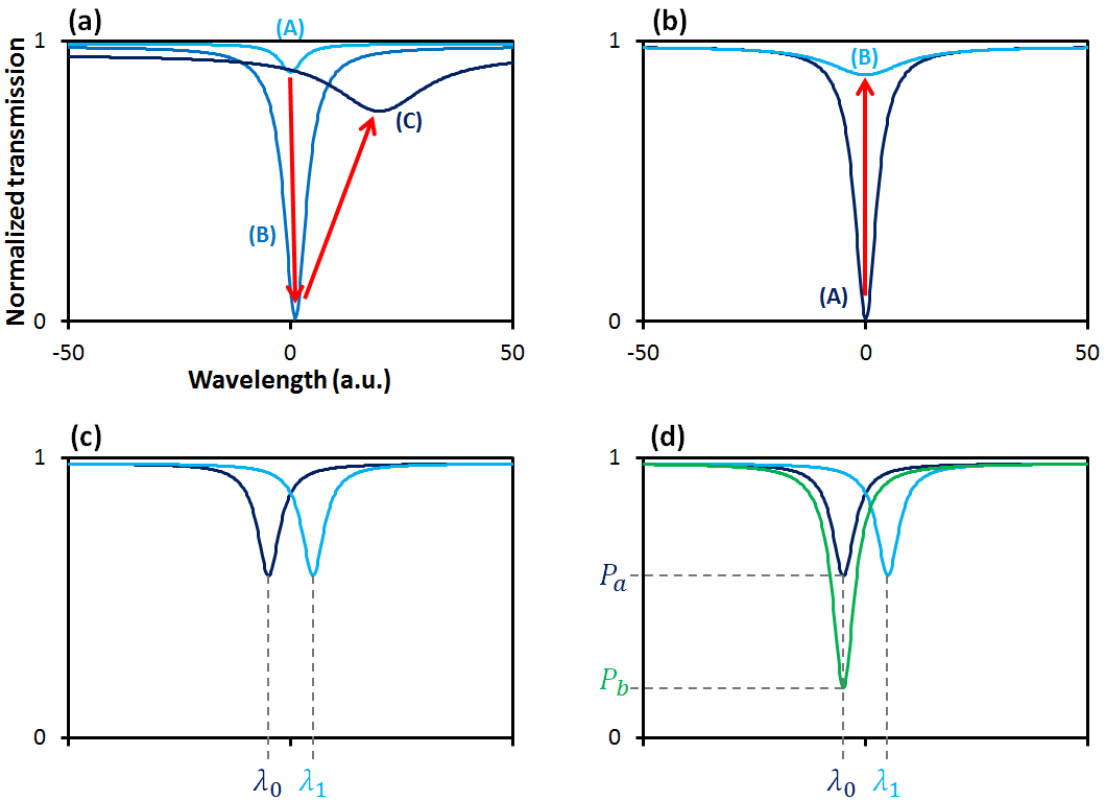

Figure 4.1

Simulated data showing schematically the transduction schemes considered here. (a) The general behavior when a waveguide is moved from large waveguide-cavity gap g_w to small g_w, $(A) \rightarrow (B) \rightarrow (C)$. (b) The general behavior when a critically-coupled resonator has its internal loss increased due to the gap g_a between it and a nearby absorber changing from large g_a to small g_a, $(A) \rightarrow (B)$. (c) In most ring resonator transduction schemes, we look for changes in resonant frequency. However in such schemes, a thermal drift from $\lambda_0 \rightarrow \lambda_1$ is indistinguishable from the signal causing a resonant wavelength shift from $\lambda_0 \rightarrow \lambda_1$ (except for the fact that thermal drift is a slow effect – but if we remove the slow thermal drift via feedback, we forfeit the ability to transduce slowly-

varying signals). (d) In the two schemes in this chapter we are looking for a change in transmission on-resonance $P_a \rightarrow P_b$. This is therefore distinguishable from a thermal drift $\lambda_0 \rightarrow \lambda_1$ as shown here.

4.2.1 : Cavity-waveguide gap changing

As can be seen in Figure 4.1 (a) (A), when the waveguide is far from the cavity, the cavity is undercoupled, has small extinction, exhibits approximately the intrinsic cavity linewidth. As the waveguide is brought closer (B), the resonant frequency doesn't change (much) and for the most part the cavity resonant dip just becomes deeper until the transmission on-resonance becomes zero at the critical coupling point. Beyond that point we enter the overcoupled regime (C) – the extinction decreases, the linewidth increases, and the cavity resonance shifts to longer wavelengths. For this section we consider the regime between (A) and (B), with the laser wavelength set at the resonant frequency. We choose this regime for several reasons:

(1) One motivation for investigating this sensing scheme, even though from the outset it was understood that it can have lower transduction efficiency in terms of $\frac{d(P/P_0)}{dx}$, is described in Figure 4.1 (b) and (c). In (b) we see the most common scheme for ring resonator transduction: A ring resonator dip at λ_0 shifts to the longer wavelength λ_1 in response to some desired signal (acceleration, current injection, dielectric environment changing, stress and strain, etc). This results in a change in output intensity when a laser is biased at λ_{laser} on the side of the dip. However, the same shift can also be seen when there is a change in temperature, so if you observe a slow change in output intensity at fixed wavelength *it is impossible to say if this came from temperature change or from the parameter you are trying to transduce*. If you are detecting changes much faster than temperature drift, you simply use a feedback loop to keep the laser biased on the side of the resonance. However

in doing this you inherently throw away the low-frequency signal along with the thermal drift. For certain applications, e.g. tactical-grade inertial sensors, it is important to capture *all* of the signal – even at low frequencies. On the other hand, the transduction regime we investigate here is shown in Figure 4.1 (c). Note that now there is a difference between thermal drift (which causes $\lambda_0 \rightarrow \lambda_1$) and the signal (which causes $P_a \rightarrow P_b$). By dithering the wavelength around the optical resonant wavelength, these two effects can be differentiated. Dithering the wavelength of an on-chip laser will most likely involve fluctuation of the laser driving current, which can cause slight wavelength tuning by a Joule heating effect. However the device resonant frequency may instead be dithered if preferred (e.g. using the electro-optic effect to dither a ring resonator resonant frequency by injecting current). In doing so we may use feedback to keep the laser wavelength locked directly onto the cavity resonance or vice-versa, and the signal will be correctly transduced, even at very low frequencies.

(2) Sensitivity to displacement (the largest optical output change for a small displacement) is not the only thing that matters. Other things may be important for practical sensors, such as:

    a. Using larger gaps rather than smaller gaps, for ease of and repeatability of fabrication. (The microtoroid example presented in this chapter has its nominal operating point at the rather large gap of about 700 nm – though this is partially due to the low-index materials used, nonetheless the principle is that while in frequency-shift transduction smaller gaps are always better, in the present regime the smallest gap is not necessarily the optimal gap.)

b. There can be large device-to-device variation for high-Q_o ring resonators, changing the response of each device which needs to be measured and calibrated out in the driving circuitry. The scheme presented in this chapter, however, does not depend on linewidth so may be less sensitive to fabrication variations.

c. Temperature stability as described in (1) above. Along with this is the associated power consumption of heaters, etc.

(3) Since the slope of the cavity resonance is zero on resonance, laser frequency noise will not be imprinted on the signal, as it will be for side-of-resonance transduction schemes such as those in Ch. 3 and Ch. 5. This is of course assuming the amplitude of laser frequency noise is much smaller than the cavity linewidth, which it usually is. For example an on-chip laser such as that by Bowers *et al.* [59] has a linewidth of $3.6\ \mathrm{MHz}$ which is rather large compared to state-of-the-art external cavity lasers, but still much smaller than a typical cavity linewidth (for example for $\lambda_o = 1310\ \mathrm{nm}$, $Q_o = 100\mathrm{k}$, the linewidth is $2300\ \mathrm{MHz}$). So, laser noise may be confined to RIN only.

(4) There is actually a slightly better transduction point for maximal output intensity change with movement of the waveguide, so brief discussion is needed to explain why we don't use this other transduction point. The other possible transduction point is the regime between (B) and (C) (still referring to Figure 4.1 (a)), with the laser wavelength set at the resonant frequency. Then not only do we get a similar change in D per unit waveguide movement but the resonant frequency also shifts to the right, leading to a larger observed output intensity change. However this regime is difficult or impossible to attack either analytically or computationally due to the difficulty of modeling in a general manner exactly how much the presence of the waveguide loads the cavity. Furthermore the transduction is only slightly

better, not orders-of-magnitude better, than the transduction scheme we have chosen. So instead we choose the more tenable and only slightly worse regime investigated here. Furthermore, even if this other regime is slightly better for optomechanical transduction and even if we could model it, operating with the larger is preferable compared with the smaller gaps required for this other transduction point. It is easier to fabricate larger gaps and also if this is for an accelerometer or gyroscope it is safer to operate with larger gaps as a sudden impulse can cause the device to crash more easily for smaller gaps.

(5) Lastly but importantly, this transduction scheme has not been been considered much in the literature to the author's knowledge (any relevant papers the author has found were described in Sec. 1.4.2.5). Therefore it makes sense to investigate it further even if it ends up being less useful in the end.

4.2.2 : Absorber near cavity moving

A second transduction regime considered in this chapter is shown in Figure 4.1 (b). We see that the extinction decreases as the cavity loss is increased, due to movement of an optical absorber near the cavity. The absorber, having both real and imaginary parts to its refractive index, may in fact also cause some wavelength shift as the cavity-absorber gap g_a changes, however we consider only high-Q_o resonators here such that κ is small and the effect of any such cavity mode perturbation is small, so the resonant frequency doesn't change much due to any real part of the absorber's refractive index. For simplicity we consider the cavity to be critically-coupled in absence of the absorber.

The reasons for exploring this optomechanical displacement sensing scheme are similar to (1)-(5) listed in the previous section.

4.2.3 : General formalism

We begin by looking at a model for a generalized ring resonator and then proceed to specialize it for the cases considered here. We follow the formalism of Yariv [60] and expanded upon by Rabus [61] but add additional details needed to model optomechanical effects.

A ring resonator cavity is depicted in Figure 4.2.

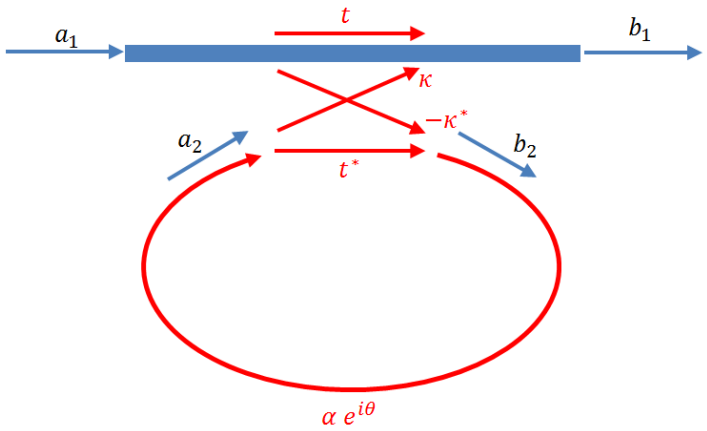

Figure 4.2

A generalized ring resonator.

The equation relating the field amplitudes $a_1,\ a_2,\ b_1,\ b_2$ is

$$\begin{bmatrix} b_1 \\ b_2 \end{bmatrix} = \begin{bmatrix} t & \kappa \\ -\kappa^* & t^* \end{bmatrix} \begin{bmatrix} a_1 \\ a_2 \end{bmatrix} \qquad \text{Eq. 4-1}$$

Without loss of generality, the field amplitudes are normalized so that their squared magnitude corresponds to the modal power and so $|a_1| = 1$. The coupler parameters t, κ are symmetric because the network is reciprocal, so the coupling matrix is unitary and

$$|\kappa^2| + |t^2| = 1 \qquad \text{Eq. 4-2}$$

The round trip in the ring is

$$a_2 = \alpha e^{i\theta} b_2 \qquad \text{Eq. 4-3}$$

Solving Eq. 4-1 and Eq. 4-3 we obtain

$$a_2 = \frac{-\alpha\kappa^*}{-\alpha t^* + e^{-i\theta}} \qquad \text{Eq. 4-4}$$

$$b_1 = \frac{-\alpha + te^{-i\theta}}{-\alpha t^* + e^{-i\theta}} \quad \text{Eq. 4-5}$$

$$b_2 = \frac{-\kappa^*}{1 - \alpha t^* e^{i\theta}} \quad \text{Eq. 4-6}$$

Squaring these leads to the in-ring power and output power as

$$|a_2|^2 = \frac{\alpha^2 (1 - |t|^2)}{1 + \alpha^2 |t|^2 - 2\alpha |t| \cos(\theta + \phi_t)} \quad \text{Eq. 4-7}$$

$$T \equiv |b_1|^2 = \frac{\alpha^2 + |t|^2 - 2\alpha |t| \cos(\theta + \phi_t)}{1 + \alpha^2 |t|^2 - 2\alpha |t| \cos(\theta + \phi_t)} \quad \text{Eq. 4-8}$$

respectively, where ϕ_t is the additional phase due to the coupling $t = |t|e^{i\phi_t}$ and we have defined T to be the cavity transmission spectrum. On resonance

$$\theta + \phi_t = 2\pi m, \qquad m \text{ an integer} \quad \text{Eq. 4-9}$$

and we obtain

$$|a_2|^2 = \frac{\alpha^2 (1 - |t|^2)}{(1 - \alpha |t|)^2} \quad \text{on resonance} \quad \text{Eq. 4-10}$$

$$T = |b_1|^2 = \frac{(\alpha - |t|)^2}{(1 - \alpha |t|)^2} \quad \text{on resonance} \quad \text{Eq. 4-11}$$

Note that a special case occurs when the coupling losses equal the in-ring losses, so that $\alpha = |t|$. Then the power on-resonance becomes zero – this is known as critical coupling.

4.3 : Cavity-waveguide gap changing

4.3.1 : Experimental results

For the results presented here, we used microtoroids fabricated as discussed in Ch. 4. While we have measured optical quality factors in excess of 20 million for such microtoroids, for this work we used a microtoroid with an intrinsic Q_o of 3.1 million. The intrinsic Q_o is identified by fitting a Lorentzian to the resonant dip when it is severely undercoupled.

The fundamental optical TE mode is identified experimentally as the one with evanescent field furthest out from the ring (measured in the radial direction) and therefore the first mode that we encounter as we bring the tapered fiber close to the microtoroid at its equator, sweeping across a wavelength range greater than the expected FSR. The dependence of extinction and cavity linewidth on taper-microtoroid gap is shown in Figure 4.3. This experiment is repeated three times as there is some uncertainty in the piezo's position – the position being accurate to only about 100 nm.

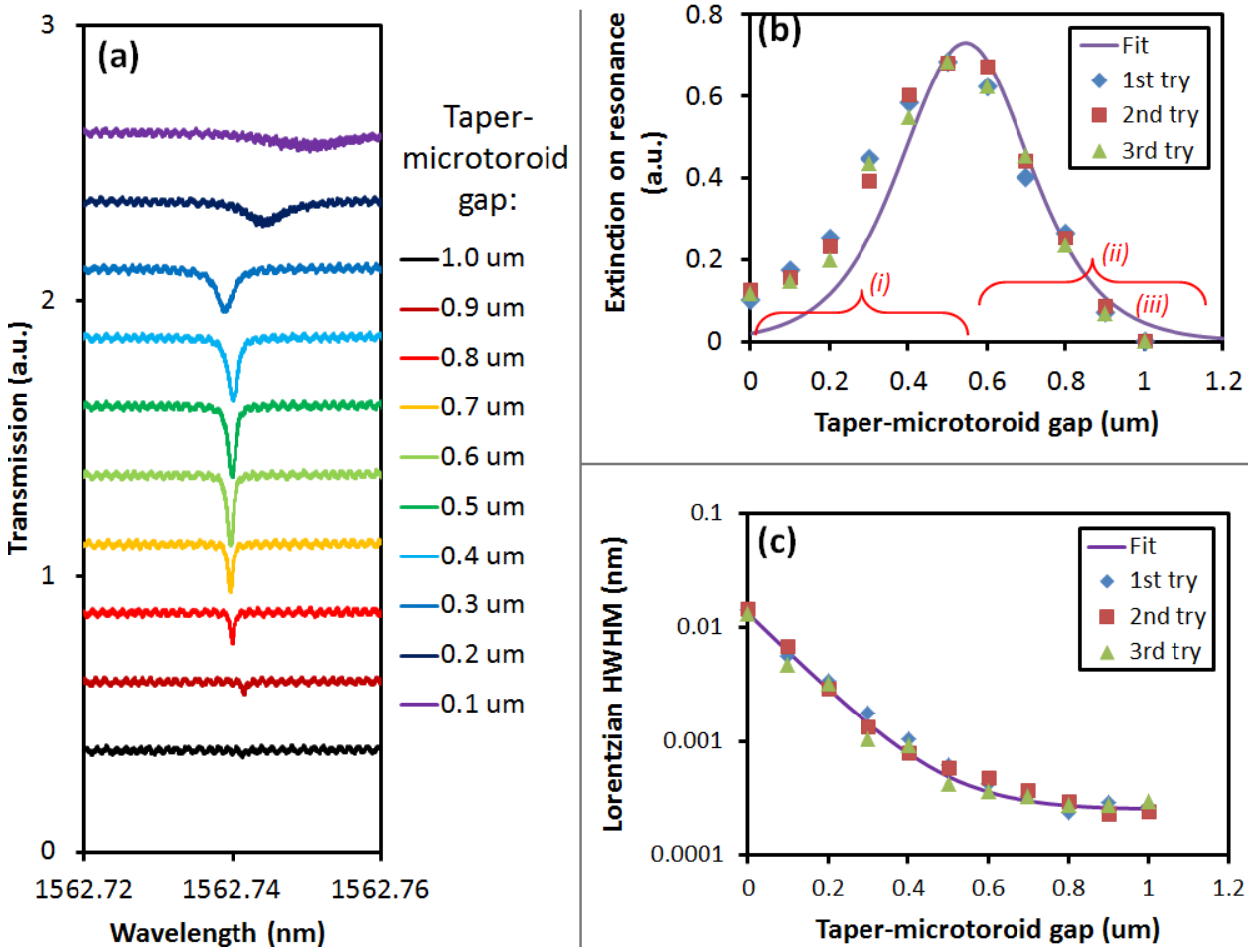

Figure 4.3

(a) Optical transmission vs. taper-microtoroid gap. The plots are offset by 0.25 for clarity. The measured center wavelength is not accurate as described in the text.

(b), (c) : The extinction and HWHM extracted from Lorentzian fits to the data. The HWHM versus gap is fitted with the equation in the text.

Note that when this experiment was performed we were not yet using the Fabry-Perot wavelength reference described in Ch. 2, so the center position of the dips in Figure 4.3 (a) is not accurate for the reasons described in that chapter. However we can expect the width and extinction ratio to be quite accurate. The fit parameters are described in subsequent sections, and show that the model captures the behavior we observe.

A few notes about Figure 4.3 (b) are worthwhile. Region *(i)* corresponds to overcoupling, region *(ii)* to undercoupling. The model we will present is really only valid in region *(ii)*. The model should be just as valid for severely undercoupled points indicated by *(iii)*, but we don't observe a good fit here – mostly due to the difficulty of measuring and fitting the Lorentzian linewidth for small extinctions (extinctions comparable to the amplitude of the large Fabry-Perot fringes observed as background ripples in Figure 4.3 (a)). Furthermore we note that the critical coupling point (where extinction goes to unity) is not observed here due to imperfect mode matching between the mode in the tapered fiber and in the microtoroid – this can be improved by fabricating the tapered fiber with diameter such that the index in the fiber matches the microtoroid mode.

Before proceeding, while intrinsic linewidth and thus intrinsic Q_o can be read directly off Figure 4.3 (c), it will be important later to know how this relates to the round-trip transmission α. We first note that the quality factor depends on round-trip time T_{rt} and round-trip loss $1-\alpha$ as

$$Q_o = \frac{T_{rt}}{1-\alpha}\omega_o \qquad \text{Eq. 4-12}$$

Thus

$$\alpha = 1 - \frac{\omega_o}{Q_o}T_{rt} = 1 - \frac{4\pi^2 r n_{eff}}{Q_o \lambda_o} \qquad \text{Eq. 4-13}$$

For the intrinsic quality factor of about 3.1 million that Figure 4.3 (c) is approaching for large gap, with radius $r = 33\ \mu\text{m}$ (measured) and $n_{eff} = 1.420$ (simulated, for fundamental TE mode for the measured microtoroid geometry), we get $1 - \alpha = 3.8 \times 10^{-4}$.

We now proceed to make a semi-phenomenological model to explain the observed behavior.

4.3.2 : Extinction model

From Eq. 4-11 the transmission T on-resonance is given by

$$T = \frac{(\alpha - |t|)^2}{(1 - \alpha|t|)^2} \equiv \frac{(\alpha - t')^2}{(1 - \alpha t')^2} \qquad \text{Eq. 4-14}$$

where we have defined the quantity t' as shown. We seek the change in transmission as gap g_w between cavity and waveguide changes, which by the chain rule is

$$\frac{dT}{dg_w} = \frac{dT}{dt'}\frac{dt'}{dg_w} \qquad \text{Eq. 4-15}$$

The first differential on the right of Eq. 3-12 is just the derivative of Eq. 4-14:

$$\frac{dT}{dt'} = \frac{2(\alpha - t')(\alpha^2 - 1)}{(1 - t'\alpha)^3} \qquad \text{Eq. 4-16}$$

The second differential on the right of Eq. 3-12 is reasoned the following way. We expect an exponential dependence on gap since the evanescent field decays exponentially. However this is only true when the presence of the waveguide does not perturb the cavity mode much – i.e. this is true for large gaps. However, proceeding with that assumption for now and noting the extreme-case dependence we'd expect between t' and α, we can write down the dependence

$$1 - t' = (1 - t_0')\ \mathrm{e}^{-\frac{g_w}{g_{0w}}} \qquad \text{Eq. 4-17}$$

This includes two phenomenological parameters. g_{0w} encodes how quickly the evanescent field decays, and t_0' encodes the coupling parameter t' at zero gap. Taking the derivative of this gives

$$\frac{dt'}{dg_w} = \frac{1 - t_0'}{g_{0w}} e^{-\frac{g_w}{g_{0w}}} \qquad \text{Eq. 4-18}$$

Now we have the pieces for Eq. 4-15 and can find

$$\frac{dT}{dg_w} = \left(\frac{(\alpha - 1) + (1 - t_0')e^{-\frac{g_w}{g_{0w}}}}{(\alpha - 1) + (1 - t_0')\alpha e^{-\frac{g_w}{g_{0w}}}} \right)^2 \qquad \text{Eq. 4-19}$$

Now, we said there were two phenomenological parameters, g_{0w} and t'. It is however far more satisfying to fit a given dataset with just one parameter. We find, however, g_{0w} can be extracted from the slope of Figure 4.3 (c) near zero – this is truly a one-parameter fit, and we write down the dependence in the next section. Then, with g_{0w} in hand, we only have one parameter remaining to fit the extinction data in Figure 4.3 (b). So this is somewhat better than just fitting one dataset with two free parameters.

So, in Figure 4.3 (b) we use that to plot Eq. 4-19 as a solid purple line. Note that we use the α calculated from the text below Eq. 4-13. We fit our phenomenological parameter only to the points in region *(ii)*, the undercoupled region, and note that as expected it does not describe the data well for the overcoupled case since the presence of the waveguide is perturbing the cavity mode for small gaps. Nonetheless, the qualitative behavior is correct, and we observe this slope to be largest at a gap of approximately $g_w \approx 0.7\ \mu\text{m}$. (As described earlier in this chapter, a similar slope may be seen near $0.3\ \mu\text{m}$, but since our model doesn't capture the overcoupled behavior well, and since it's a similar slope but at an undesirable smaller gap, we choose to consider only the $g_w \approx 0.7\ \mu\text{m}$ operating point and disregard the $0.3\ \mu\text{m}$ point.) The slope of the best-fit line is $\left.\frac{dT}{dg_w}\right|_{g_w = 0.7\ \mu\text{m}} = -2.6 \frac{P_{max}}{\mu\text{m}} = 5.1 \frac{P_0}{\mu\text{m}}$, where we have written it in terms of the P_{max} and P_0 introduced earlier. Therefore

$$\frac{d(P/P_0)}{dx} = 5.1 \times 10^6\ \text{m}^{-1} \qquad \text{Eq. 4-20}$$

To get even better transduction in the future we may:

- Have better mode-matching between the cavity and waveguide so to achieve true critical coupling.
- Have lower g_{0w} – in other words, use a mode that spatially decays more quickly. However this comes at the cost of using a smaller gap than $g_w \approx 0.7$ as the transduction point.

Lastly we note that changing α and t_0' doesn't affect the slope much, within reasonable values of α and t_0'.

4.3.3 : Linewidth model

We expect the linewidth H (half-width at half maximum) to have a contribution from the coupling term t and a contribution from the intrinsic loss. The former comes from the loaded linewidth due to the waveguide loading the cavity, and the latter is the intrinsic linewidth due to cavity losses. The former will obey the same exponential dependence as we expect for t (since the field decays exponentially too) and the latter will be a constant:

$$H = H_0 \exp\left(-\frac{g_w}{g_{0w}}\right) + H_{int} \qquad \text{Eq. 4-21}$$

where $H_{int} = \lambda_o/2Q_o$ is the usual intrinsic linewidth and H_0 is the linewidth at zero gap. We fit Figure 4.3 (c) to Eq. 4-21 to obtain: $H_0 = 13$ pm, $g_{0w} = 0.125$ μm, $H_{int} = 0.25$ pm.

Of course, if our transduction mechanism is as described in the introduction then it matters little if our linewidth changes. However it is mentioned because it is of use in extracting g_{0w} by looking at the slope near zero gap, and it may be of use for further investigation of the optimal transduction points.

4.4 : Absorber near cavity moving

4.4.1 : Experimental results

We fabricate spherical silica resonators by taking optical fiber (Corning SMF-28e+, 125 um diameter), cleaving it, and melting the cleaved end using the arc from a fiber fusion splicer for a few

seconds. This results in very smooth spheres at the cleaved tip with diameters from 200-250 um (larger spheres are made by applying the arc for longer). Microscope images of the sphere next to a tapered fiber are shown in Figure 4.4.

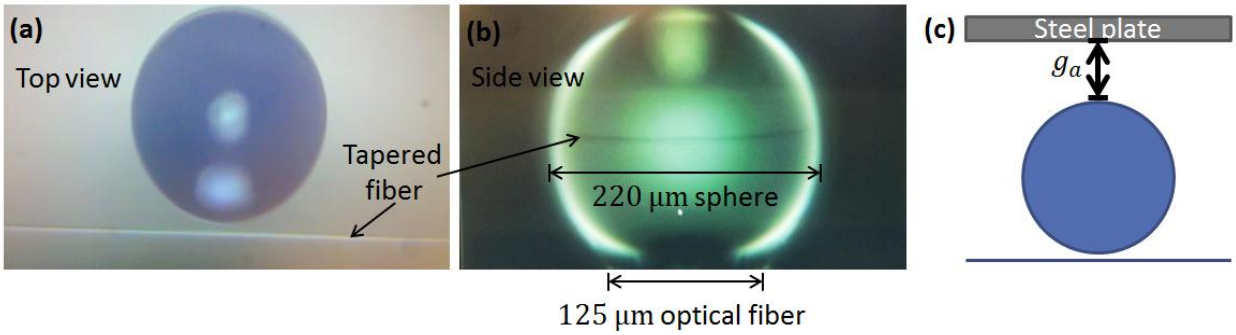

Figure 4.4

(a), (b) The silica sphere used in the experiments in this section. (c) Schematic showing how the polished steel plate is brought close to the sphere, with sphere-plate gap g_a.

This time the taper gap and polarization is optimized for maximum extinction and held fixed. A flat polished steel plate is then brought in from the other side as shown in Figure 4.4(c). This steel plate acts as an optical absorber, evident by the fact the resonant dip disappears completely when it is touching the sphere. There may be some backscattering from the plate, but we believe this is minimal since the curved sphere surface adiabatically approaches the plate due to the large radius of curvature, and so is not considered here. An additional proof that significant backscattering does not occur is that in the past when observing the spectrum from a microsphere with a particle attached (and therefore large back-reflections from that point), we have observed optical mode splitting due to degeneracy between clockwise and counter-clockwise modes – however we do not observe such split resonances for these experiments.

Unlike in the microtoroid which had relatively few optical modes, enabling us to choose the fundamental mode through the mechanism described in that section, for the sphere we have a complicated and dense array of modes and it is not so easy to identify which is which. The result is that for these experiments we don't know which optical mode we are using, but at least the model can be tested and some quantitative results obtained at the end.

The experimental data is shown in Figure 4.5. Note that again the resonant wavelength in Figure 4.5 (a) appears to be moving around but, like in the microtoroid experiments described earlier, this is due to sweep-to-sweep variation in the laser piezo-based scan, and this experiment was done before we started using the Fabry-Perot reference cavity as explained in Ch. 2 to provide a wavelength reference.

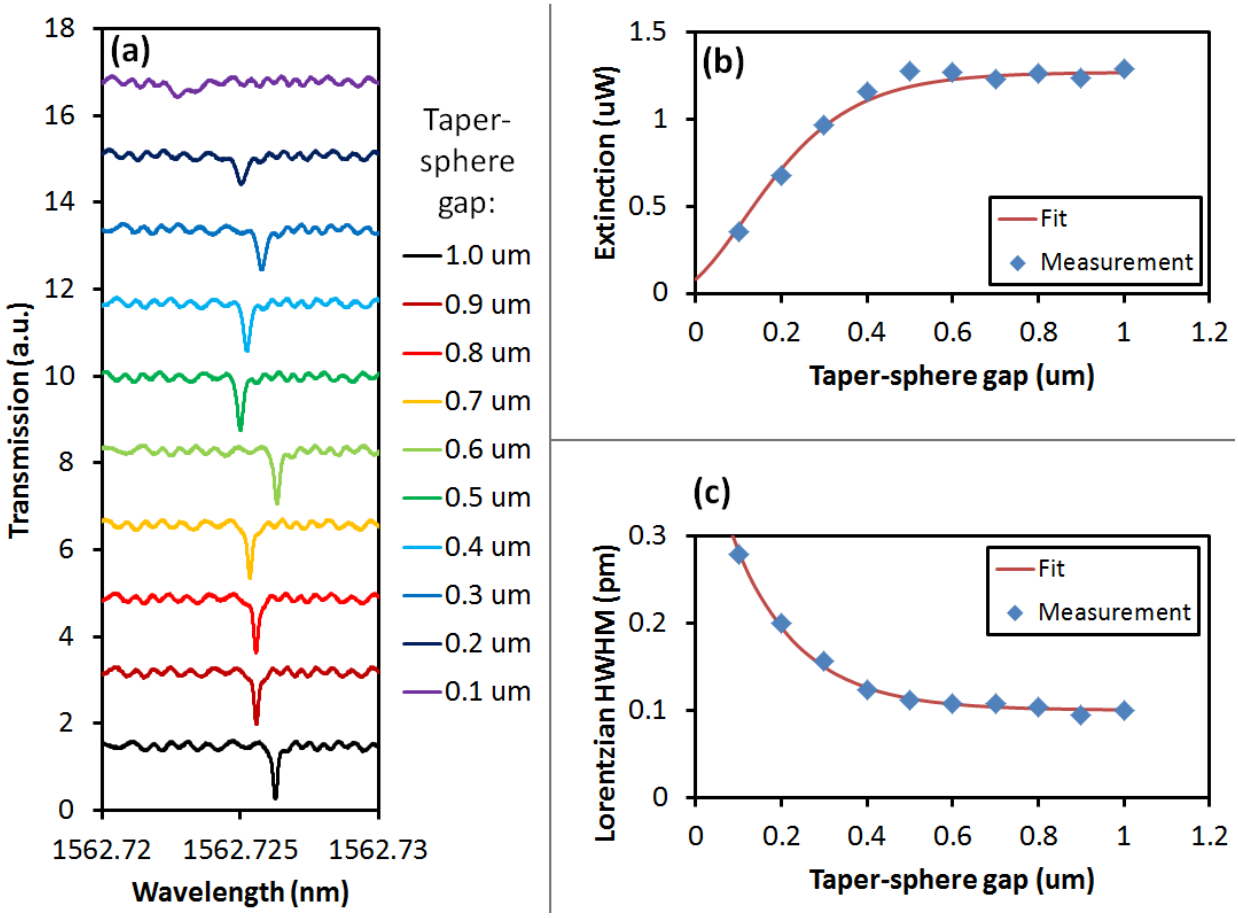

Figure 4.5

(a) Optical spectrum for the silica sphere for different taper-sphere gaps. The resonant frequency appears to be moving around but this is an artifact as explained in the text. (b), (c) : The extinction and HWHM extracted from Lorentzian fits to the data.

4.4.2 : Extinction model

Referring again to Eq. 4-14 (transmission on resonance), we seek the change in transmission as gap g_a changes, which by the chain rule is

$$\frac{dT}{dg_a} = \frac{dT}{d\alpha}\frac{d\alpha}{dg_a} \qquad \text{Eq. 4-22}$$

The first differential on the right of Eq. 3-12 is just the derivative of Eq. 4-14:

$$\frac{dT}{d\alpha} = \frac{-2(\alpha - t')(t'^2 - 1)}{(1 - t'\alpha)^3} \qquad \text{Eq. 4-23}$$

The second differential on the right of Eq. 3-12 is reasoned the same way as for Sec. 4.3.2, and we have the dependence

$$1 - \alpha = (1 - \alpha_0)\, e^{-\frac{g_a}{g_{0a}}} \qquad \text{Eq. 4-24}$$

which has the derivative

$$\frac{d\alpha}{dg_a} = \frac{1 - \alpha_0}{g_{0a}}\, e^{-\frac{g_a}{g_{0a}}} \qquad \text{Eq. 4-25}$$

which when substituted into Eq. 4-15 gives

$$\frac{dT}{dg_a} = \frac{-2(t'^2 - 1)(1 - \alpha_0)\left((t' - 1) + (1 - \alpha_0)\, e^{-\frac{g_a}{g_{0a}}}\right)}{g_{0a}\left((t' - 1) - t'(1 - \alpha_0)e^{-\frac{g_a}{g_{0a}}}\right)^3} \qquad \text{Eq. 4-26}$$

To find t' we note that the fiber was moved to make the microsphere-fiber gap at the critical coupling point (actually, not perfectly critically coupled but as close as the index mismatch between the microsphere and fiber would allow), and we know at critical coupling that $\alpha = |t| = t'$, and we can find

α from Eq. 4-13. For the intrinsic quality factor of about 8 million that Figure 4.5 (c) is approaching for large gap, with radius $r = 110$ μm (measured) and $n_{eff} = 1.44$ (simulated – it varies for different modes but for example, the twenty lowest-order optical modes have $1.442 < n_{eff} < 1.452$) we get $1 - t' = 1 - \alpha|_{g_a \to \infty} = 5.0 \times 10^{-4}$.

Again we have two phenomenological fit parameters g_{0a} and α_0, however unlike in Sec. 4.3.2 we have a harder time extracting a reliable g_{0a} from the slope of the linewidth measurements near zero gap, because the dip disappears near zero gap! So in this case we just simultaneously fit both parameters to the data in Figure 4.5 (b). From the best-fit line, the maximum slope is at $\left.\frac{dT}{dg_a}\right|_{g_a = 0.12\ \mu\text{m}} = 2.7\frac{P_{max}}{\mu\text{m}} = 5.4\frac{P_0}{\mu\text{m}}$, which leads to

$$\frac{d(P/P_0)}{dx} = 5.4 \times 10^6\ \text{m}^{-1} \qquad \text{Eq. 4-27}$$

4.4.3 : Linewidth model

We expect the linewidth H (half-width at half maximum) to have a contribution from the cavity losses $\alpha(g_a)$ and a contribution from the constant coupling term t. The former comes from intrinsic cavity losses and any additional loss due to a nearby absorber, and the latter comes from the loaded linewidth due to cavity losses and also due to the waveguide loading the cavity. The former will obey the same exponential dependence as t (and a constant part that can be lumped into the latter) and the latter will be a constant:

$$H = H_0 \exp\left(-\frac{g_a}{g_{0a}}\right) + H_{int} \qquad \text{Eq. 4-28}$$

where $H_{int} = \lambda_o/2Q_o$ is the usual intrinsic linewidth and H_0 is the linewidth at zero gap. We fit Figure 4.5 (c) to Eq. 4-28 to obtain: $H_0 = 0.35$ pm, $g_{0a} = 154$ nm, $H_{int} = 0.10$ pm.

As for Sec. 4.3.3, the linewidth dependence does not matter much for this transduction scheme, but the linewidth model is only mentioned here because it may be of use for further investigation of the optimal transduction points in the future.

4.5 : Summary and comparison

In summary, for the cavity-waveguide gap changing case, we have

$$\frac{dT}{dg_w} = \left(\frac{(\alpha - 1) + (1 - t_0')e^{-\frac{g_w}{g_{0w}}}}{(\alpha - 1) + (1 - t_0')\alpha e^{-\frac{g_w}{g_{0w}}}} \right)^2 \qquad \text{Eq. 4-29}$$

and we found a transduction figure of $\frac{d(P/P_0)}{dx} = 5.1 \times 10^6\ \mathrm{m}^{-1}$, and discussed some ways to improve that further. Meanwhile for the absorber-moving-near-cavity case we have

$$\frac{dT}{dg_a} = \frac{-2(t'^2 - 1)(1 - \alpha_0)\left((t' - 1) + (1 - \alpha_0)\, e^{-\frac{g_a}{g_{0a}}}\right)}{g_{0a}\left((t' - 1) - t'(1 - \alpha_0)e^{-\frac{g_a}{g_{0a}}}\right)^3} \qquad \text{Eq. 4-30}$$

with a transduction figure of $\frac{d(P/P_0)}{dx} = 5.4 \times 10^6\ \mathrm{m}^{-1}$.

The similarity between these two transduction figures is not completely coincidental – due to the common origins of Eq. 4-29 and Eq. 4-30 and the common material system (though not the same geometry it has somewhat similar mode confinement; and while α, t are different between the two transduction schemes, there is not strong dependence on those parameters within the range of the experiments presented here), these can be expected to be at least a similar order of magnitude. Put another way, because the strongest parameter dependence is on the spatial decay of the mode (g_{0w} or g_{0a} respectively), and because we have a similar material system with similar mode confinement and therefore similar spatial decay rate, these numbers can be expected to be somewhat similar despite their different mechanisms.

These results will be considered further in Ch. 6.

Chapter 5 : Cavity-gap-cavity optomechanical displacement sensing

Equipped with his five senses, man explores the universe around him and calls the adventure Science.

-- Edwin Powel Hubble

5.1 : Introduction

In this chapter, we consider two-cavity devices, with one fixed and one free cavity. As the gap between the cavities changes, the optical resonant frequency changes, which is used to transduce the relative displacement of the two cavities.

We first provide some mathematical formalism, then theoretically and experimentally consider a stacked-ring approach. Lastly we discuss an alternative approach using linear photonic crystal cavities and compare between the two approaches.

5.2 : Sensor operating principle

When two identical cavities are brought into proximity, we observe hybridization of the optical modes – each mode splits into an “even” and an “odd” mode. Examples for stacked ring cavities are shown later, in Figure 5.2, however this applies to any optical cavity. These “supermodes” can be extremely sensitive to the gap between the two cavities. Considering a perturbative model, we imagine that as the cavities are far apart, the presence of one cavity perturbs the mode of the other cavity but little. As the cavities are moved closer together, the presence of a cavity perturbs the other more. Thus we expect the gap-sensing effect to get stronger as the cavities are brought closer. Since the evanescent fields decay exponentially, we expect this effect to get stronger exponentially. Beyond this, an analytical formalism in an experimentally-useful form is not possible since it depends on the spatial shape of the optical mode, but finite element modeling captures this effect well as we shall see. We will consider

these numerical models as we discuss two configurations in subsequent sections: stacked ring resonators, and side-by-side (or stacked) 1D photonic crystal cavities. One parameter we seek is $\frac{d(P/P_0)}{dx}$ which tells how much the optical power output changes with the gap, and therefore we proceed in each case to find each of the differentials on the right side of Eq. 5-1.

$$\frac{d(P/P_0)}{dx} = \frac{1}{P_0}\frac{dP}{d\omega_o}\frac{d\omega_o}{dx} \qquad \text{Eq. 5-1}$$

The stacked-ring geometry is shown in Figure 5.1.

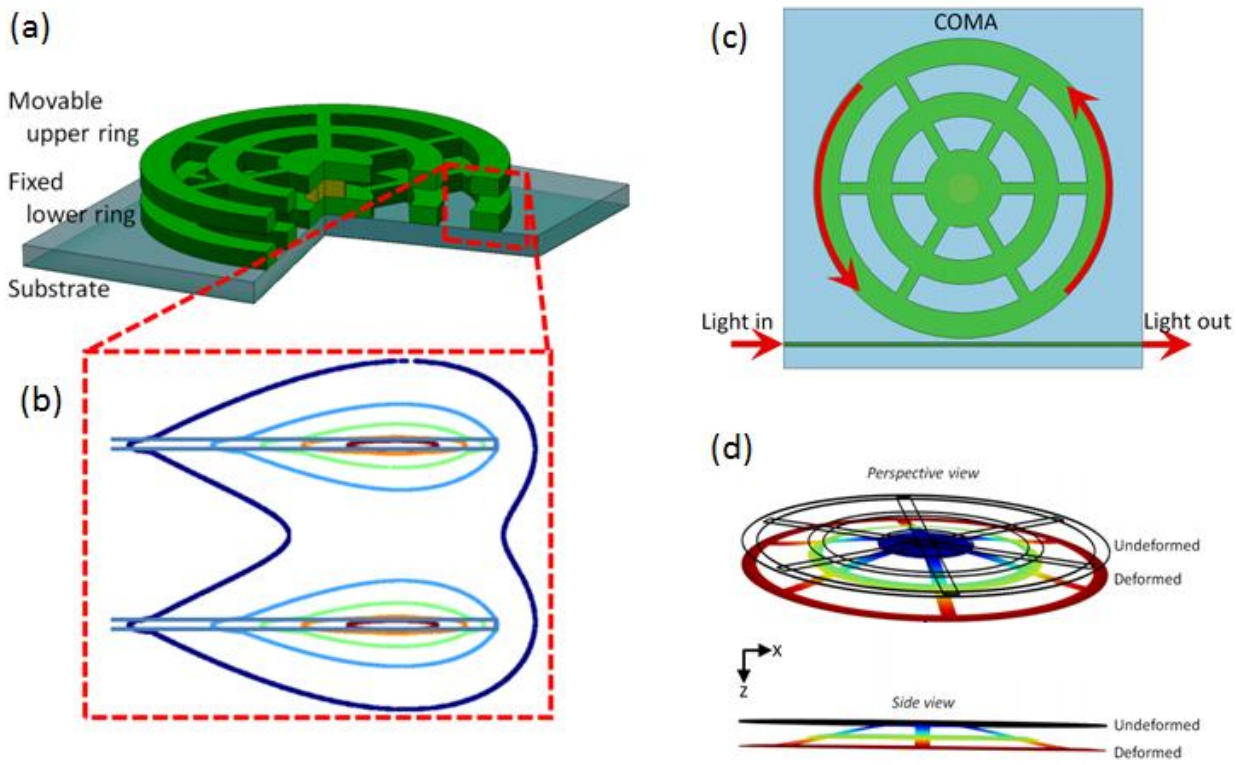

Figure 5.1

(a) Perspective cartoon view of stacked-ring displacement sensor. The lower ring is attached to the substrate and the upper ring is released, attached by a central post. (b) Finite-element model of one optical eigenmode, showing H-field contour lines, showing the coupling between the rings. (c) Light is coupled into the ring via

a nearby waveguide and circulates in the ring. (d) Finite-element model showing only the top ring, in deformed (colored by displacement) and undeformed (black wireframe) state.

There is not just one cavity mode, of course. We simulate and observe different mode families, each of which have a different optomechanical coupling (which can be extracted from simulation). Some of these modes for the geometries of interest are shown in Figure 5.2 (a).

We may ask whether the two cavities need to be exactly identical, as it may have seemed from looking at Figure 5.1 (b). In fact since one ring is fixed onto a dielectric substrate and one ring is surrounded by air, they already do not have identical dielectric environments. A few finite element simulations are illuminating here. We find that in fact the rings do not need to be identical, and the tolerance to non-similarity becomes greater as the gap decreases and the rings become more strongly coupled. Contour plots showing the fundamental even and odd optical mode, for non-identical rings are shown in Figure 5.2 (b). In this plot, we made the top ring have a 200nm smaller radius than the bottom ring. Changing the dielectric environment is another way to break the symmetry between the rings, and yields the same results. In Figure 5.3 we see the plotted results from the simulations in Figure 5.2 (b).

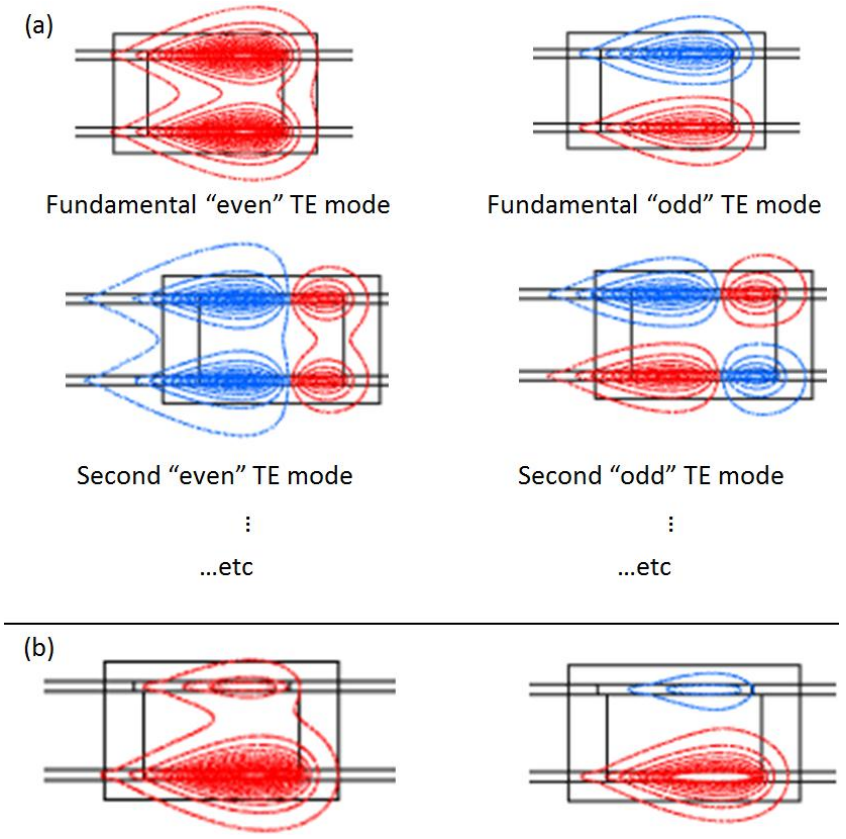

Figure 5.2

(a) Contour plots indicating various optical modes for the geometry of the device presented here. (b) Non-identical rings (in this case, the top ring radius is smaller by 200 nm).

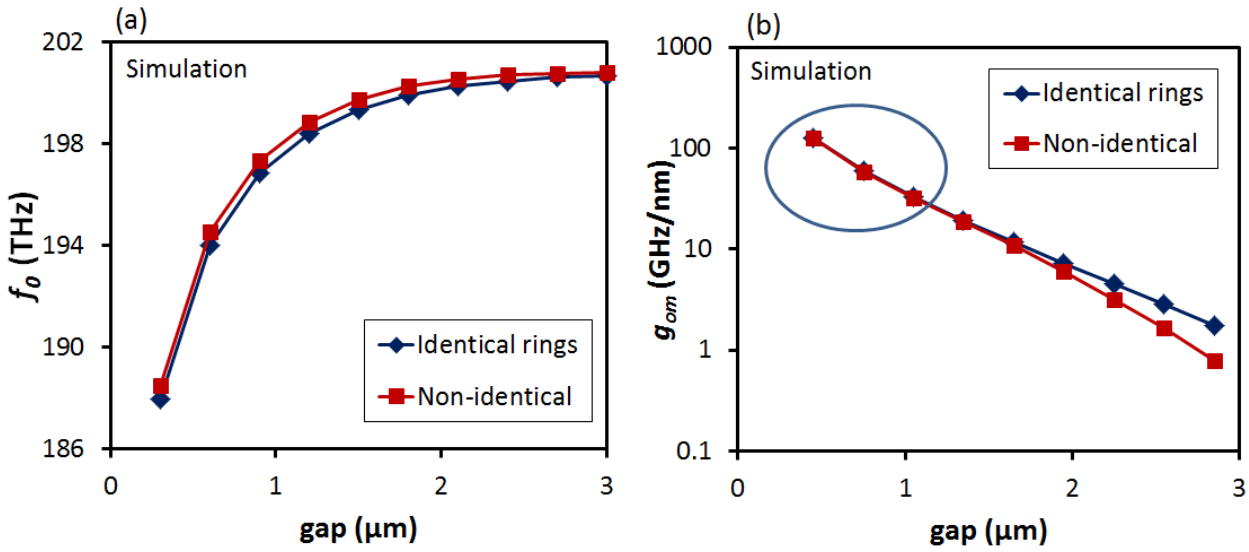

Figure 5.3

(a) The resonant optical frequency and (b) the optomechanical coupling coefficient for the identical and non-identical rings in Figure 5.2 (a) and (b) respectively.

Somewhat surprisingly, given the different appearance of the contour lines in Figure 5.2 (a) and (b), the optomechanical coupling is similar. In particular we see from Figure 5.3 that for small gaps the optomechanical coupling is essentially identical between the two cases. This makes sense, because when the gap is small the two rings are very strongly coupled, and act more like a single (multimode) ring. For large gaps, however, the presence of one ring is more like a perturbation for the mode of the other ring, meaning the non-identicality of the rings is more important.

5.3 : Device fabrication

The first set of devices were fabricated as shown in Figure 5.4. These were probed with a tapered fiber with a wavelength reference cavity in parallel as described in Ch. 2.

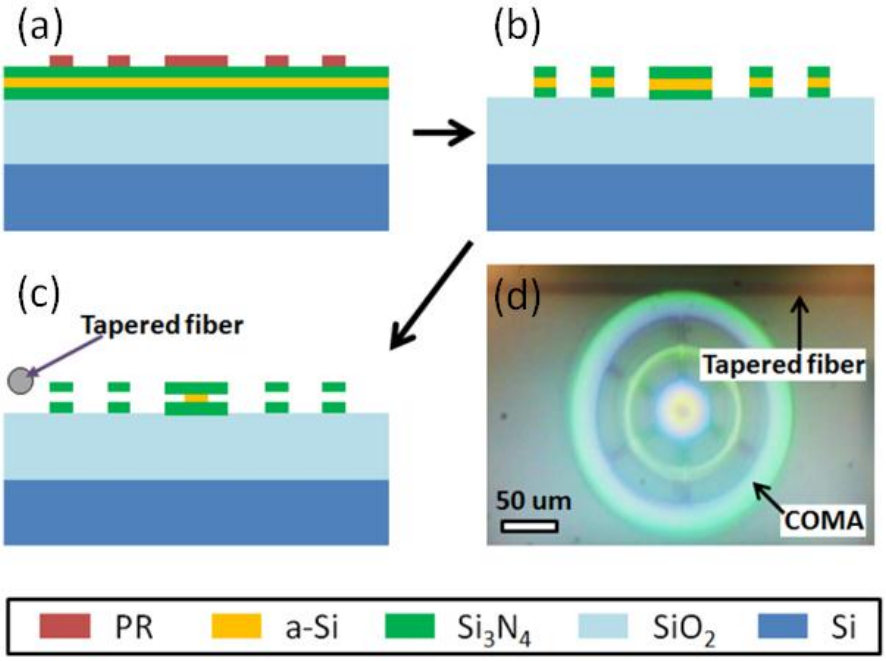

Figure 5.4

The fabrication process for the first type of devices we made. Parts (a)-(d) are discussed in the text.

In Figure 5.4, (a)-(c) shows the fabrication process. Details of these steps are as follows:

(a) First we start with commercially-available 4" Si wafers with 4 um of wet-grown thermal oxide from University Wafer. We deposit 220nm of stoichiometric LPCVD Si_3N_4 at 775 °C, 200 mTorr, flowing 67 sccm of dichlorosilane and 200 sccm of ammonia, resulting in a deposition rate of about 3.7 nm/min. The device wafers were single-spaced with at least 3 "baffle" wafers before and after the device wafers. We observed much greater uniformity using these baffle wafers, and typical uniformity for our process was 3% across the 4" wafer. Next we cool to room temperature and transfer to a different LPCVD furnace to deposit amorphous Si ("a-Si" in the legend) at 570 °C, 200 mTorr, flowing 100 sccm of silane, to get 180 nm of a-Si and a deposition rate of about 2.9 nm/min. Note that if we instead used temperatures above about 600 °C there was a visible change to the resulting film – rather

than looking smooth and grey like a silicon wafer it looks almost transparent – we assume this is because depositions at higher temperatures results in polycrystallinity and different optical properties, however we didn't do further characterization of this.

Next the wafers were cooled again to room temperature as they were taken out of the furnace, and put back into the first furnace for another Si_3N_4 deposition with the same process parameters as we used for the first Si_3N_4 deposition.

Note that since the upper nitride layer is deposited at 775 °C, we observed it to cause crystallization of the underlying amorphous silicon layer – evident as visible roughening or "crystal-like" appearance of the amorphous silicon under the microscope after nitride has been deposited on top. This is probably not ideal as it presumably causes increased roughness of the nitride films, however since we still observed large enough optical quality factors we did not investigate this further.

Next, 3 um of photoresist ("PR" in the legend of Figure 5.4) is spun. For this, first we spin HMDS adhesion promoter at 3000 rpm/s, 3000 rpm/s/s, 30 s, then spin SPR220-3 photoresist at 3000 rpm/s, 3000 rpm/s/s, 60 s, bake at 115 °C on a proximity hotplate for 120 s, exposed to form the "cartwheel" or "spiderweb" shape shown in Figure 5.4 (d), then baked again with the same parameters, then manually developed in MIF-726 for 40 s.

(b) The nitride-silicon-nitride films were etched down to the buried oxide using reactive ion etching in the following process: An Oxford 100 tool was used, and was first put through a 10 min clean cycle with oxygen plasma. The wafer was etched for 8.5 min using 50 mTorr, 50 sccm CHF_3, 2 sccm O_2, 200 W reactive ion etching.

Next the photoresist was removed by immersion in 1165 and sonication for 2 hours, then a immersion in acetone for 60 s then isopropyl alcohol for 60s, then blown dry with nitrogen.

Note that we also tried using an oxygen asher to remove the photoresist but got mixed results – sometimes the photoresist would not be removable – so settled on the wet removal process just described.

(c) For the final step we etched the a-Si using XeF_2, to undercut and release the upper ring. Since this etch is highly density-dependent (thus, for example, devices near the edge of the wafer become released much faster than devices at the center of the wafer), cycles of the following recipe were performed until the desired devices were successfully released (observed in a microscope between each cycle). One cycle consisted of the following etch parameters, and usually 5-10 repeats were needed to release the devices. The recipe is: 10 cycles, 2 s etch time per cycle, 1 mTorr XeF_2,5 mTorr N_2.

(d) A microscope image of the device is shown in Figure 5.4 (d), also showing the tapered fiber used to couple light in.

The device shown in Figure 5.4 has not only an outer ring and a central circle, but also a ring between the two. This ring is purely for structural purposes – while rings both with and without this additional ring successfully released, it was found that the ring was more likely to release and to be flatter (measured using optical profilometry) with the addition of this ring.

The second iteration of devices had an integrated waveguide and therefore different process steps. We show a microscope image of one device later (Figure 5.6 (c)), but first we describe the process to fabricate the device with integrated waveguide in Figure 5.5.

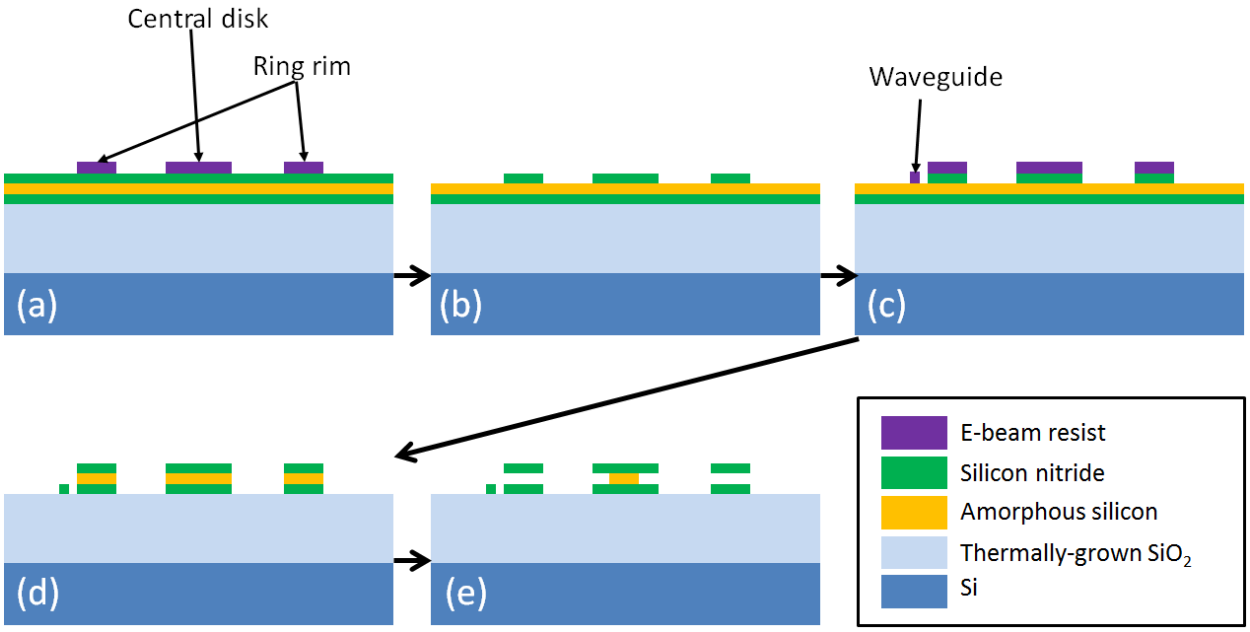

Figure 5.5

The fabrication process for stacked rings with an integrated waveguide.

The fabrication process is similar except two-mask electron beam lithography is used (with 400 nm of ma-N 2403 electron beam resist used in each step). We used proximity correction via LayoutBEAMER software – we found that without proximity correction, the gap between the waveguide and the rings was fused in all devices. This is partially due to the difficulty of electron-beam lithography on thick dielectric layers, but may also be partially due to the difficulty of patterning a waveguide near an extant feature (see Figure 5.5 (c), where the waveguide is to be patterned near the ring rim from Figure 5.5 (a)), but was at least solved well enough by using proximity correction in our case.

The devices were all observed to curl upwards after release as shown in Figure 5.6.

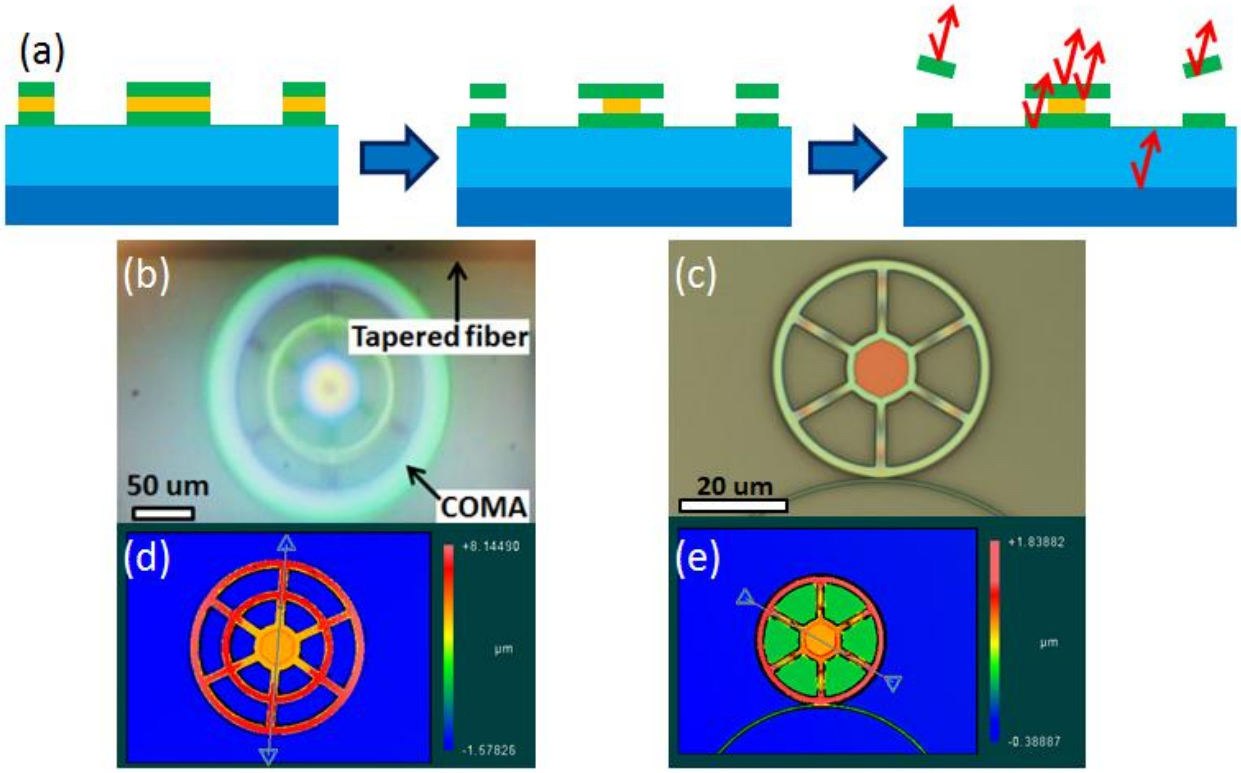

Figure 5.6

(a) The upper ring curls upwards after release as indicated. The red arrows in the third diagram indicate light from the optical profilometer reflecting off different facets, and is discussed further in the text. (b)-(c) This curl-up is evident under an optical microscope as colored fringes on the spokes. (d)-(e) After release we take an optical profilometer measurement to determine the new gap at the rim (which is much larger than the initial gap), however light can bounce from many different surfaces (indicated by red arrows in (a)), and if it bounces from a surface that is not the top surface, the optical profilometer measurement is frustrated. This is solved using the method described in the text (basically, just use reflections from the top facet). Since these images show reflections from all surfaces, and

since light reflected from any non-top-facet surface will have the depth miscalculated by the optical profilometer (because it assumes free-space propagation), the color bar is not very meaningful here.

We note that many (>50%) of the largest rings (radius over about 100-200 microns) of the non-integrated devices we made (Figure 5.6 (b)) were stuck down after release rather than curled up. In contrast, all of the smaller rings were curled up. Therefore when we progressed to making integrated devices (Figure 5.6 (c))) we chose smaller radii and all rings were successfully released.

We also observed that silicon nitride thicknesses above about 350 microns often had cracks running through the film, which cracks may or may not always be obvious by inspection before release. After release, however, the cracks are obvious as the XeF_2 penetrates these gaps and etches a-Si below it. (Films above about 400 nm had cracks and peeling that were obvious even before XeF_2 release.)

In Figure 5.6 (d)-(e) we see the curl-up of the upper ring represented by a color scale, as measured by optical profilometer. A few points are worthy of note however. First, the color bar is not accurate here because (A) the device is transparent, and sitting on a transparent substrate, and optical profilometers do not do a good job of capturing height data in such circumstances – because of reflections from different surfaces and also because the refractive indices of the transparent films must be taken into account (the optical profilometer assumes free-space propagation). Secondly, the space between the spokes in Figure 5.6 (e) is green indicating a higher height than the surrounding blue. We don't fully understand the source of this but often observed it in smaller openings such as this – it may be due to slightly less etching in these areas due to etch proximity effects, thus making a different thickness there or rougher surface which registers as a different thickness. Since we can't trust optical profilometry for such transparent film stacks, we extracted the gap by simply measuring the top-surface reflections from the COMA itself – from comparing the height from top-surface reflections at the center

(hub), and the top-surface reflections from the "rim". Thus the optical profilometer laser light that yields this data never entered the film stack and so refractive index and multiple reflections do not need to be accounted for. It is obvious looking at the optical profilometer data which are the top surface reflections because these are always the highest points (and reflections from each of the other surfaces can be identified). The measurements give gaps of around 2-4 um. For the rings with optical and mechanical data presented here, this gap was measured to be 2.5 um.

5.4 : Further modeling

5.4.1 : Finding $d\omega_o/dx$

We simulate the optical mode to calculate how the optical resonant frequency will be affected by deformation of the upper ring. We model the optical mode of the stacked rings using finite element software to extract the optical eigenfrequencies ω_o versus ring-ring gap z for the fundamental optical mode. The fundamental even optical mode is shown in a contour plot in Figure 5.1 (b), and further plots will be shown later. For this fundamental optical mode, the resonant frequency and its derivative, $g_{om} = \frac{d\omega_o}{dz}$, is plotted in Figure 5.7. For the gap indicated by the dotted line, we find $\frac{g_{om}}{2\pi} \approx 4\ \mathrm{GHz/nm}$, and clearly smaller gaps are desirable.

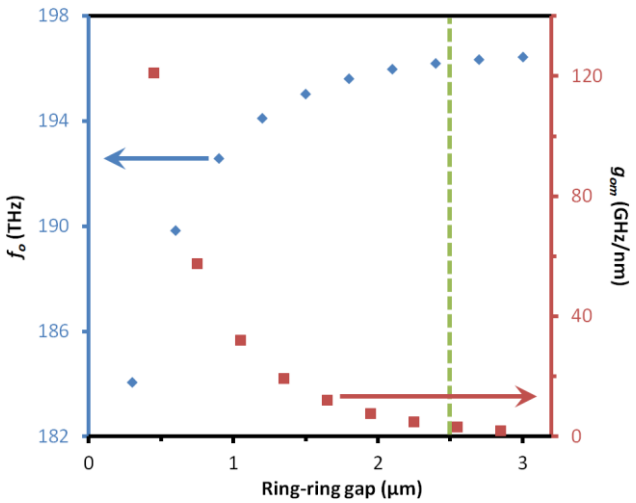

Figure 5.7

Simulated optical eigenfrequency (blue diamonds) and optomechanical coupling strength g_{om} (red squares) [5] for stacked rings separated by different gaps. The green dashed line indicates the measured gap for the fabricated device.

5.4.2 : Finding $dP/d\omega_o$

To find $dP/d\omega_o$ at the transduction point (essentially, the slope of on the side of the resonant dip) we first investigate the optical spectra. The optical resonances are Lorentzian and so are given by [62]

$$P(\omega) = P_{max}\left[\frac{4(\omega-\omega_o)^2 + \omega_o^2\left(\frac{1}{Q_{int}} - \frac{1}{Q_{coup}}\right)^2}{4(\omega-\omega_o)^2 + \omega_o^2\left(\frac{1}{Q_{int}} + \frac{1}{Q_{coup}}\right)^2}\right] \quad \text{Eq. 5-2}$$

where P_{max} is the input power, and Q_{int} and Q_{coup} are the intrinsic optical quality factor and the coupling contribution, respectively. For our analytical model we will assume critical coupling and that our laser wavelength is set to the steepest point of the dip. For critical coupling, $Q_{int} = Q_{coup}$, so the total optical quality factor Q_o is

$$\frac{1}{Q_o} = \frac{1}{Q_{int}} + \frac{1}{Q_{coup}} = \frac{\Delta\omega_{FWHM}}{\omega_o} = \frac{\Delta\lambda_{FWHM}}{\lambda_o} \quad \text{Eq. 5-3}$$

We choose as our transduction point a point halfway down the dip, one HWHM from the resonant frequency. The slope at this point is as follows, where we have also substituted the more relevant $P_0 = P_{max}/2$:

$$\left.\frac{dP(\omega)}{d\omega}\right|_{\omega=\omega_o\pm\frac{\omega_o}{2Q_o}} = \frac{Q_o}{\omega_o}P_{max} = \frac{Q_o}{2\omega_o}P_0 \quad \text{Eq. 5-4}$$

We pause here to mention that in the literature it is usually assumed that the point of maximum slope is halfway down the Lorentzian, as we have done. In fact it is at an offset of $\frac{1}{\sqrt{3}}$ times HWHM as can

be seen by differentiating the Lorentzian to find the point of steepest slope. In practical terms it matters little since $\frac{1}{\sqrt{3}} \approx \frac{1}{2}$, and the point of steepest slope is not necessarily optimal since we also want to maximize SNR by being further up the dip, thus having more signal while sacrificing some slope. In any case the HWHM point is a convenient and simple compromise.

Rearranging the differentials we get

$$\frac{dP}{dz} = \frac{Q_o}{2\omega_o} P_0 \frac{d\omega}{dz} \qquad \text{Eq. 5-5}$$

$$\frac{d(P/P_0)}{dz} = \frac{Q_o}{2\omega_o} \frac{d\omega}{dz} \equiv \frac{Q_o g_{OM}}{2\omega_o} \qquad \text{Eq. 5-6}$$

We may also write this in terms of acceleration:

$$\frac{d(P/P_0)}{da} = \frac{Q_o}{2\omega_o} \frac{d\omega}{dz} \frac{dz}{da} \equiv \frac{Q_o g_{OM}}{2\omega_o} \frac{dz}{da} \qquad \text{Eq. 5-7}$$

The only thing that remains to know in Eq. 5-7 is dz/da, how much the gap at the rim of the ring changes per unit acceleration. To do this we simply simulate the upper ring deforming under its own weight using FEM (not shown) and find the gap change for this particular ring to be $\frac{dz}{da} = 0.45\ \mathrm{nm}/g$.

5.5 : Experimental results

5.5.1 : Static measurements

We took a device without an integrated waveguide (the device in **Error! Reference source not ound.** (b) with radius $150\ \mu\mathrm{m}$), and optically probed it by bringing the tapered optical fiber nearby with the chip face-up, and then with the chip face-down. To measure the chip face-down (and at any arbitrary angle) we constructed a sample-holding stage with a hinge that had 180° of motion so that when the hinge was closed, the chip was face-up, and when the hinge was fully open, the chip was face-down, which we described in Ch. 2. The purpose was to measure gravity, since these two measurements

would have a differential acceleration of $2\ g$ for face-up vs. face-down, and some fraction of that for arbitrary tilts. Results are presented in Figure 5.8.

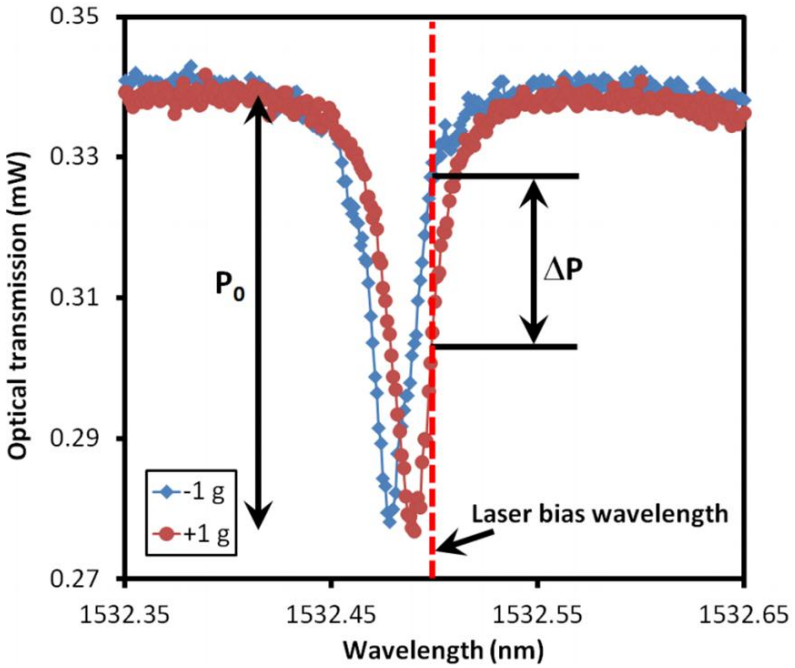

Figure 5.8

An example optical spectrum of the chip face-up (blue diamonds, -1 gee), and face-down (red circles, $+1$ gee).

A shift of nearly half the linewidth is observed.

We next wanted to test the repeatability of the measurement, for two reasons: (A) In Ch. 2 we previously described problems with the piezo wavelength scan of the laser not being the same each time, so wanted to know that the correction mechanism using the Fabry-Perot cavity in parallel that we described before is effective. (B) More importantly, we observed that since the resonant wavelength is dependent on cavity "loading" from presence of the tapered fiber, and since the fiber-cavity gap was set manually each time, we wanted to not only eliminate operator bias but also show that even if the exact same coupling point is not achieved each time, the results are still consistent for the undercoupled case (as we expect). Thus we show that we achieve consistent results each time we take a measurement.

It is necessary to comment briefly here on (B), though a full discussion and measurements were shown in Ch. 4. Varying the fiber-cavity gap from severely undercoupled to critically-coupled does not change the resonant wavelength much, since the fiber is not loading or changing the cavity much, since it is so far away and interacting weakly. However varying the fiber-cavity gap from critically-coupled to overcoupled changes the resonant wavelength a lot, since the presence of the nearby fiber changes the optical path length around the resonator. Therefore in order to ensure we have the exact same coupling each time (and therefore we are not confusing an accelerometry measurement with an effect due to fiber-cavity proximity), we choose for the next measurement to operate in the severely-undercoupled regime.

To do this we position the chip face-up, and bring in the fiber until we are barely coupled to the device (the extinction ratio is intentionally only about 20% as can be seen in Figure 5.9), maximizing the extinction ratio at that large taper-cavity gap using a polarization controller. In other words, the fiber is far from the device but the polarization is matched to the mode we are interrogating. We then take an optical spectrum (along with the spectrum of our reference Fabry-Perot cavity described in Ch. 2). The device and taper are then separated and the device is repositioned on the stage in preparation for a chip face-down measurement and the fiber polarization is manually scrambled. We then bring together chip and fiber in fiber in chip-face-down configuration. Again we manually position the fiber to couple light to the device and vary the polarization, only aiming to get approximately the same extinction ratio as before (and again we choose the polarization that maximizes the extinction ratio). Therefore we have just taken a face-up measurement and then taken a face-down measurement from scratch. Note that due to the way the stage is configured, it is difficult to repeat this laborious process for face-up then face-down – it is much simpler to cycle through these steps if we choose something like 0° tilt and 65° tilt – because then the stage can be easily manipulated into the next measurement. Therefore in Figure

5.9 we show six measurements performed in this fashion for those two angles. It can be seen that regardless of human error in getting the exact same extinction ratio or exact same coupling each time, there is a clear shift in the resonant wavelength even for the relatively small gravitational shift of $1\ g$ (chip at 0°) to $\cos(65°) \approx 0.42\ g$.

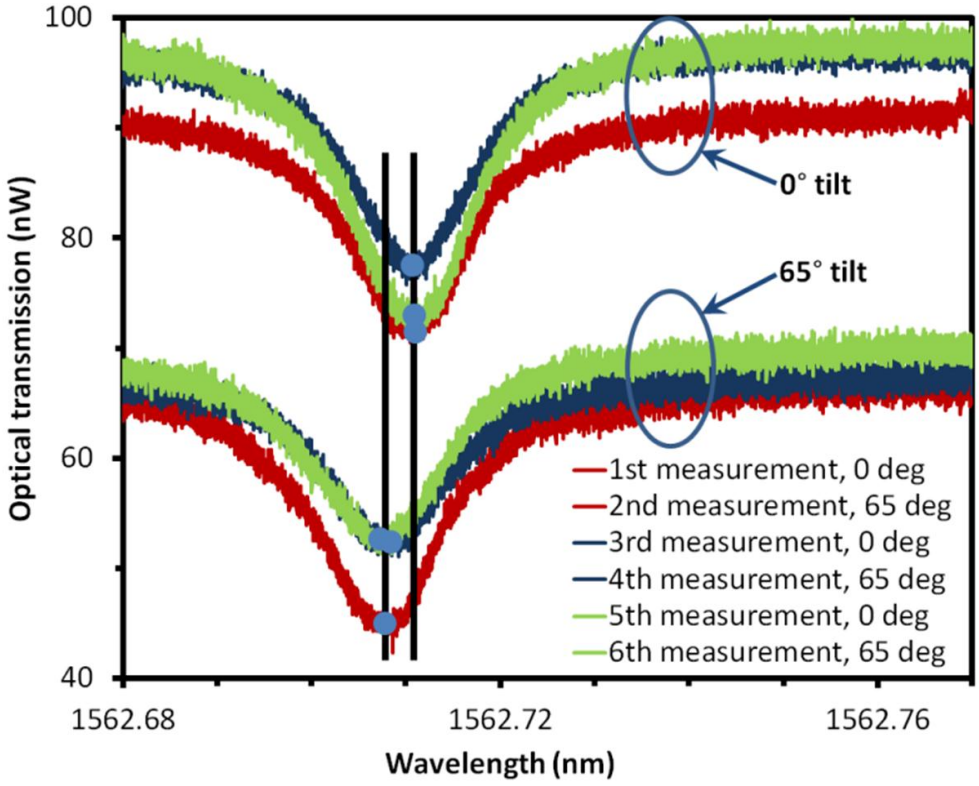

Figure 5.9

A measurement at 0° tilt, then 65° tilt, then 0°, 65°, 0°, 65°, shows that even with the "human" factor of having a slightly different coupling to the device each time (due to manual positioning of the tapered fiber), we observe a consistent shift in the resonant wavelength of the device as we change the orientation of the device relative to gravity.

Note that for this measurement we use only tens of nanowatts of power – we want to be sure we are barely changing the cavity, but also for Figure 5.8 we were using a power meter which tolerated large power inputs while for Figure 5.9 we were using a different detector with much lower thresholds.

We are now in a position to evaluate our model in Eq. 5-6 and Eq. 3-12. In Figure 5.8 we find $Q_o \approx 66{,}000$ and from the simulation shown in Figure 5.7, $g_{OM}/2\pi \approx 4\ \mathrm{GHz/nm}$, which leads to

$$\frac{d(P/P_0)}{dz} = 6.9 \times 10^8\ \mathrm{m}^{-1} \qquad \text{Eq. 5-8}$$

$$\frac{d(P/P_0)}{da} = 0.31\ g^{-1} \qquad \text{Eq. 5-9}$$

In an alternative approach, we find the shift from a Lorentzian fit to Figure 5.8 to be $10\ \mathrm{pm}$ for $2\ g$ of acceleration change, which leads to a back-calculated value of $\frac{g_{OM}}{2\pi} = 8.9\ \mathrm{GHz/nm}$, somewhat comparable to the simulated value in Figure 5.7 of $4\ \mathrm{GHz/nm}$. The discrepancy is likely mostly due to an uncertainty of the exact geometry and the exact resonant frequency.

This could be increased a lot further in the future – foremost by decreasing the gap between the rings as shown in Figure 5.7. For example, Rosenberg *et al.* [17] fabricated similar silicon dioxide cavities with 150 nm gap between them, resulting in $g_{OM}/2\pi = 31\ \mathrm{GHz/nm}$.

5.5.2 : Dynamic measurements

As described in Ch. 2, we cannot simply shake the chip to test our accelerometer because the light is precisely coupled to the chip – in one type of device this is coupled via a nearby tapered optical fiber, and in our integrated devices this light is coupled from a polished angled fiber array into grating couplers.

However, the device is already moving around due to the thermal-mechanical motion of the device itself. We may detect this motion instead and use it to gain important information about the device.

The vacuum testing setup is described in Ch. 2. While we tested both types of devices (taper-coupled and integrated) in the chamber we will report the results from the waveguide-integrated devices since then there is no uncertainty about whether the taper was touching the movable ring.

After putting the device in the vacuum chamber, coupling light in through grating couplers with typical insertion loss of -12 to -15 dB per coupler (these are rather high loss – more work could go in to optimizing these), we pumped the chamber down and observed the optical and mechanical spectrum. A typical optical spectrum is shown in Figure 5.10.

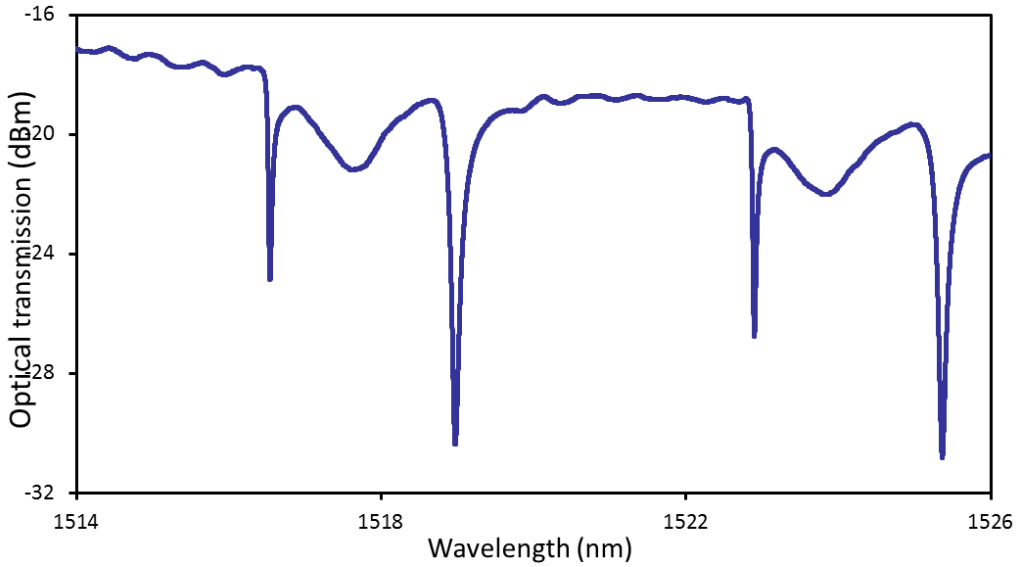

Figure 5.10

A typical optical spectrum for stacked-rings, measured in vacuum.

To take these measurements we used the maximum available input power (+10 dBm) – the grating coupler loss is evident from the figure, however we still got enough light to measure the mechanical signal. The mechanical signal from the device in Figure 5.10 is obtained by sitting on the side of one of the resonances (for the data shown here, the steepest slope at around 1516.5 was chosen) and is shown in Figure 5.11.

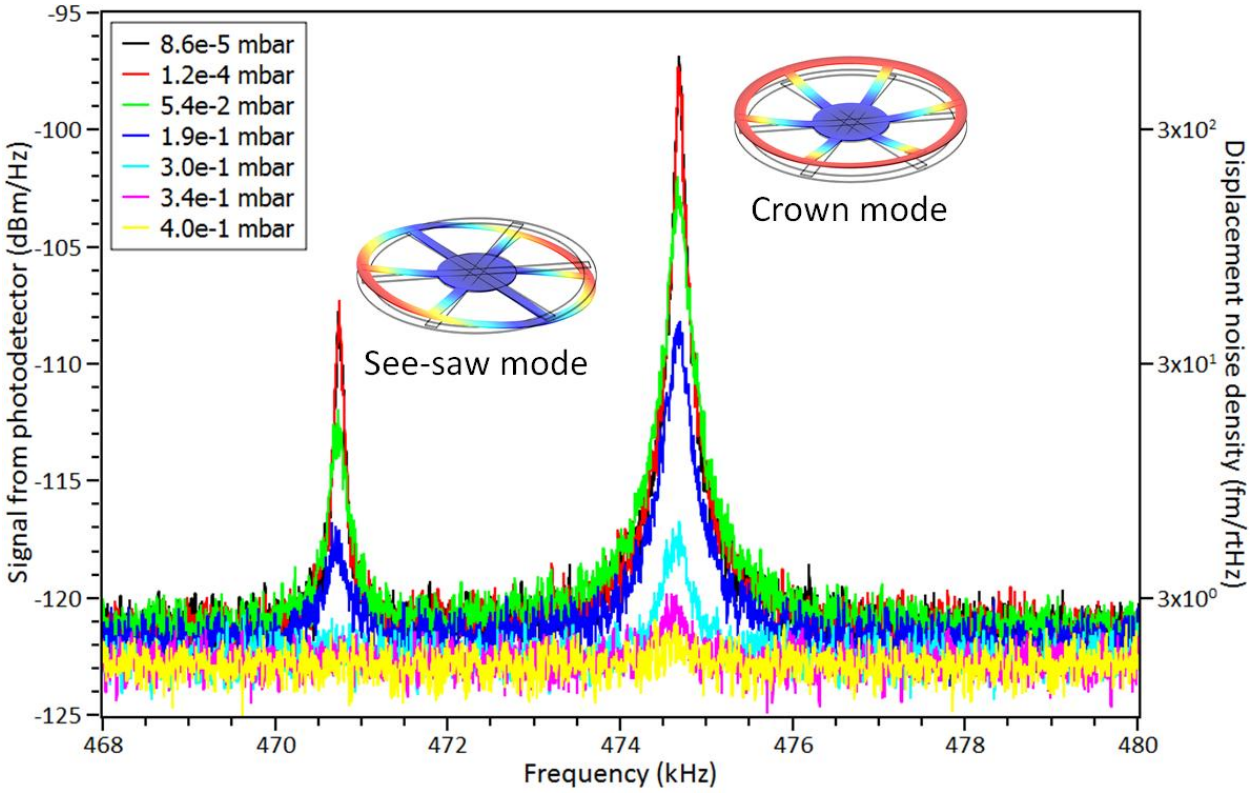

Figure 5.11

Mechanical spectrum observed at different pressures. The two mechanical modes shown here were identified by COMSOL simulation (inset images) to be the "see-saw mode" and "crown mode" of the upper ring moving.

In the mechanical spectrum we see several features worthy of note.

1) Motion is not detectable for pressures above about 0.4 mbar (0.3 Torr). This is due to air damping but also probably due to strong squeeze-film (Couette) damping between the rings, since they have 5 um wide rims and are spaced by only 2.5 um.
2) One may at first wonder why we see the see-saw mode at all – one side moving upwards changes the effective index in half of the ring in one direction, while the other side moving downwards changes the effective index in the other half of the ring in the opposite

direction. However these two effects do not perfectly cancel out because the g_{OM} dependence is an exponential one, not linear.

3) However we do observe that the crown mode has a much larger signal than the see-saw mode. This is to be expected because motion of the crown mode changes the effective index all the way around the ring simultaneously while effect of the see-saw mode motion partially cancels itself as just described. Higher-order out-of-plane modes will move less than the see-saw mode, and are subject to the same partial cancellation effect, so it is not surprising we do not observe any other modes other than the two shown here.
4) The COMSOL simulation gives mechanical frequencies for the free ring that are smaller by about 5% – this is attributed to uncertainty in the thickness of the film and the fact that the mechanical eigenfrequencies for a curled-up ring are probably different than for the flat ring we simulated.
5) The displacement noise density (calculated knowing the power modulation at the detector and assuming $g_{OM} = 4\ \mathrm{GHz/nm}$ from simulations based on a measurement of the gap) is at a level of about $3\ \mathrm{fm}/\sqrt{\mathrm{Hz}}$.
6) As the air- and Couette-damping decreases and the top ring moves more, the noise floor rises by about 2 dB. This is not just the tailing part of the mechanical Lorentzians, instead the noise floor even far from the mechanical resonances was observed to rise by about this amount. This indicates that at atmospheric pressure the thermal motion is air- and/or Couette-damped and so the observed noise floor is limited by the detector noise (it's not the laser noise, for turning off the laser doesn't change it; nor is it the spectrum analyzer noise, for the noise level when attached to the powered-up detector is higher than when not attached). On the other hand, at low enough pressures the device becomes more free to

move and we are limited by the thermal-mechanical noise floor of the device itself. To improve upon this noise floor we may either attach a large mass to the movable ring, or have a device with higher Q_m, as discussed in Ch. 2's noise discussion. An approach to get higher Q_m in a similar device was demonstrated by Krause *et al.* [7] – by using silicon nitride optical cavities under high tension (ours are under no tension at all), they measure Q_m over two orders of magnitude higher than that reported here.

For the plot in Figure 5.11, we extract parameters of interest and plot them in Figure 5.12. The data suggest that air damping is still present – it is likely that even higher thermal-mechanical signal and Q_m are achievable at lower pressure, however the vacuum chamber we were using was limited to a base pressure of about 8.6×10^{-5} mbar.

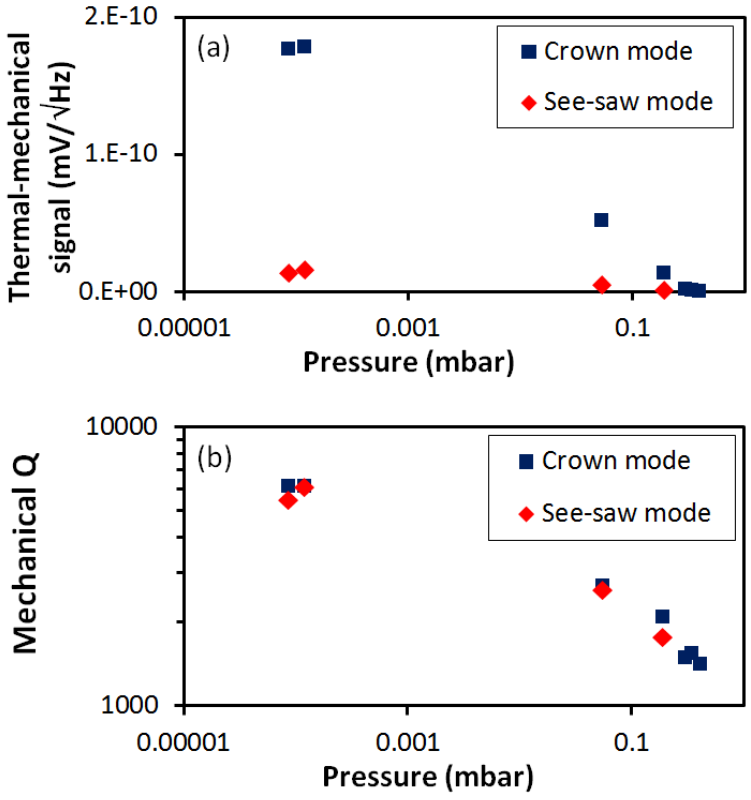

Figure 5.12

(a) The peak thermal-mechanical signal versus pressure. (b) Q_m (from a fitted Lorentzian) versus pressure.

5.6 : 1D photonic crystal cavity version

5.6.1 : Device overview

The approach for photonic crystal (PhC) cavities is analogous to that for stacked ring cavities, and the same approaches can be taken to design (via FEM modeling, extracting g_{OM}) and fabricate them, however they are more difficult to fabricate due to small feature sizes. An in-plane version and a stacked version are schematically shown in Figure 5.13.

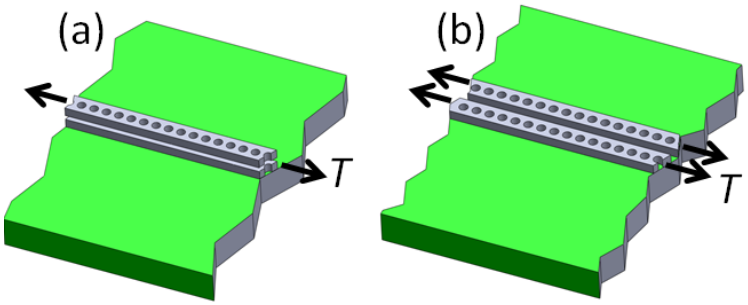

Figure 5.13

Two configurations of coupled photonic crystal cavities. (a) Two stacked PhCs with a gap between – the lower one attached to the green substrate. (b) Two side-by-side PhCs with a gap between – the green substrate will be removed, one PhC is attached to a fixed frame (not shown), the other to a movable proof mass (not shown). The "T" indicates that the upper free PhC in (a), and both PhCs in (b), can be pulled in tension after release via built-in film stress, preserving the small gaps.

The key advantage to the device in Figure 5.13 (a) over the stacked ring geometry investigated earlier is that the upper PhC can be pulled in tension T after release – thus maintaining the desired small

gap between the two photonic crystals. The key advantage to the device in Figure 5.13 (b) is that all devices are fabricated in one layer, allowing for lithographic control over the gap; and both devices can be pulled in tension T after release. Such tension was not possible with a ring geometry because the light must travel around the rim, so the rim (and hence the whole ring) cannot be pulled in tension. Thus we observed large curl-up and hence a large gap increase as the built-in film stress was released after release. An additional advantage of the approach in (b) is that the free PhC can be attached to an arbitrarily large proof mass for increased acceleration or Coriolis force transduction – however it may be difficult to attach a proof mass to the free ring in the stacked-ring device.

So, we have observed that 1D photonic crystal cavities may be a promising way ahead, however most of the author's work has previously been on rings. Krause *et al.* at Caltech [7] have reported an accelerometer based on the device geometry in Figure 5.13 (b).

5.6.2 : Reflection back into on-chip laser

However with all the benefits of Figure 5.13 (b), there is one important difference which may be a problem for integrating these devices with on-chip lasers. Ring cavities in general, and the stacked-ring cavities we presented specifically, have no significant back-reflection when suitably designed, because the feeding waveguide can adiabatically approach and couple light into the ring. Photonic crystal cavities, however, have mirror symmetry – light bounces back and forth inside the cavity. Thus, the light that couples from the resonator back into the feeding waveguide (assuming this waveguide is side-coupled) is equally likely to go forward or backwards. Back-reflections into the laser can cause mode-hopping, increase laser noise, and frustrate sensitive measurements.

In fiber or free-space we simply use an optical isolator or circulator. However, many optical circulators and isolators use ferrimagnetic materials and manual assembly, and to the author's knowledge there are no good options for on-chip CMOS-compatible optical circulators or isolators.

Therefore when we move to the world of on-chip lasers and devices, the back-reflection must be measured and understood to consider, for a given on-chip laser, the effect on laser noise and mode hopping or competition.

Chapter 6 : Comparison and Conclusions

We shall not cease from exploration

And the end of all our exploring

Will be to arrive where we started

And know the place for the first time

Through the unknown, remembered gate

When the last of earth left to discover

Is that which was the beginning.

-- T. S. Eliot, from "Four Quartets"

6.1 : Introduction

In Ch. 1 we showed that reinventing the displacement sensing element of a MEMS sensor (e.g. accelerometer) has the effect of *reinventing the entire system*. We considered some of the ramifications of this with an accelerometer as a test case, and then surveyed optomechanical displacement sensors in the literature.

Ch. 2 provided some supporting material and most particularly a review of noise sources that we will refer to in this chapter.

Ch. 3-5 investigated four optomechanical displacement sensors theoretically and experimentally.

In this chapter we consider further the noise sources described in Ch. 2, the signal $\frac{d(P/P_0)}{dx}$ from the devices in Ch. 3-5, and with some assumptions based on results reported in the literature we show that optomechanical sensors are a promising route for high-SNR MEMS sensors.

6.2 : Noise

In this section we will:

1) See what noise figures are reported for commercial MEMS accelerometers.
2) Assume these noise figures are primarily electronic noise.
    - This is reasonable as we showed in Sec. 2.3.4.2, and because if they were thermal-mechanical-noise-limited then this is easily remedied by, for example, increasing the mass. Although this may increase footprint, thickness, and/or cost, this can be made to be a marginal tradeoff. In summary, thermal-mechanical noise limits are easy to fix so there is little reason for accelerometers to ever be thermal-mechanical noise limited, and in practice commercial accelerometers are electronic-noise limited.
3) Choose a noise figure around 100 times smaller than commercial MEMS accelerometers as our target for this analysis.
4) Assume we instead use optical transduction, see what combination of reasonable laser noise, detector noise, transduction strengths, etc, meets this target noise figure.

First we investigate acceleration noise figures for a random pick of eight common MEMS accelerometers (Figure 6.1). For the analysis in this section, we assume these numbers essentially represent the non-thermal-mechanical noise and we choose a target noise figure of $1\ \mu g/\sqrt{\text{Hz}}$.

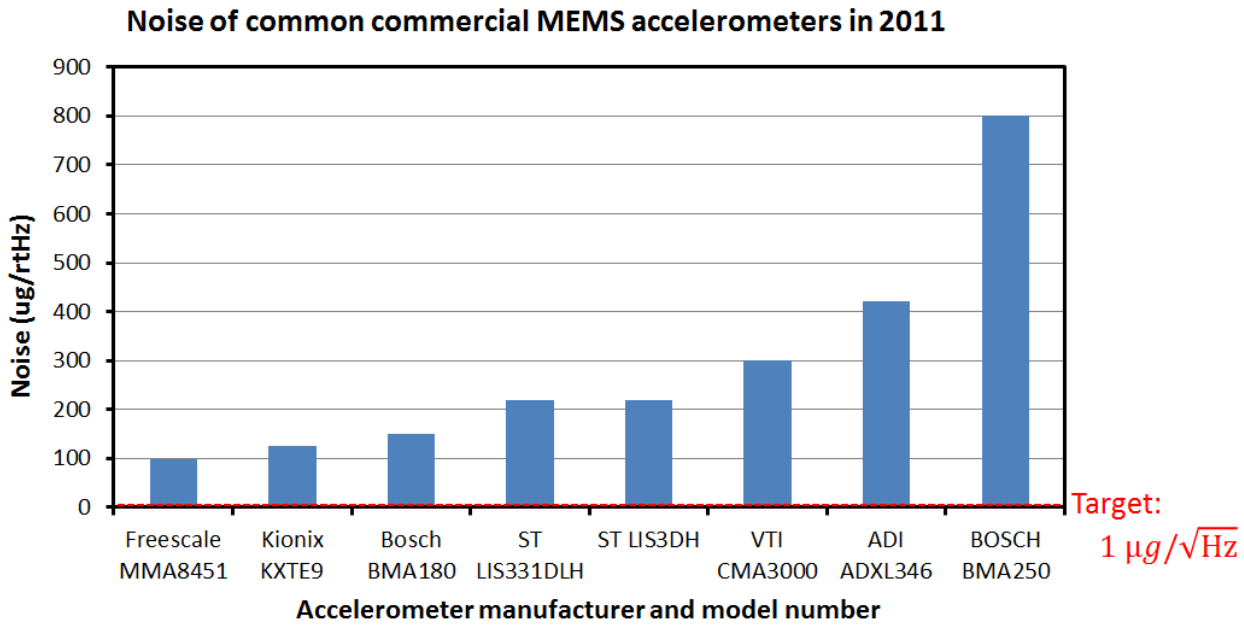

Figure 6.1

Noise figures for eight common MEMS accelerometers, and the target level we are using for the analysis in this section.

Now we have the difficult task of considering what the noise would be if this were to use optical transduction. This task is difficult because there are so many inputs as we will see below, however without actually having a fabricated device with on-chip laser and detector, we will do our best to draw conclusions that can guide future research.

As discussed in Sec. 1.3.7, reinventing the transduction scheme has the effect of reinventing the whole system – the only constant is the thermal-mechanical noise, assuming the mass and spring system is unchanged, and all other noise sources are fundamentally different. Taking into account all of Sec. 2.3.4, we can write down the relation between acceleration noise and the non-thermal-mechanical noise sources as

$$a_n = \frac{\omega_m^2 \sqrt{S_{RIN}^2 + \left(\frac{dP}{d\omega}\right) S_{LFN}^2 + S_{NEP}^2}}{\left(\frac{d(P/P_0)}{dx}\right) P_0} \quad \text{Eq. 6-1}$$

where we have added the non-thermal-mechanical noise sources in quadrature under the square root sign. This applies to resonant devices which transduce acceleration by looking for resonant wavelength shift such as in Ch. 3 and Ch. 5. For the devices in Ch. 4, we have

$$a_n = \frac{\omega_m^2 \sqrt{S_{RIN}^2 + S_{NEP}^2}}{\left(\frac{d(P/P_0)}{dx}\right) P_0} \quad \text{Eq. 6-2}$$

The inputs on the right side of Eq. 6-1 or Eq. 6-2 with their units for clarity are:

- ω_m $[\mathrm{s}^{-1}]$: Since we are not necessarily reinventing the mass or spring arrangement, we assume typical mechanical resonant frequencies of $\omega_m = 2\pi\ (10\ [\mathrm{kHz}])$.
- S_{RIN} $\left[\frac{\mathrm{mW}}{\sqrt{\mathrm{Hz}}}\right]$: The linear laser RIN per root bandwidth.
- $\frac{dP}{d\omega}$ $\left[\frac{\mathrm{mW}}{\mathrm{Hz}}\right]$: The slope of the Lorentzian cavity resonance, if applicable, at the point of steepest slope. Taking the derivative of a Lorentzian we find this is $\frac{dP}{d\omega} = \frac{Q_o P_0}{\omega_o}$ where Q_o is the optical quality factor, P_0 is described later, and we take the resonant frequency to be $\omega_o = \frac{2\pi c}{1.31\ \mu\mathrm{m}}$.
- S_{LFN} $\left[\frac{\mathrm{Hz}}{\sqrt{\mathrm{Hz}}}\right]$: The linear laser frequency noise per root bandwidth.
- S_{NEP} $\left[\frac{\mathrm{mW}}{\sqrt{\mathrm{Hz}}}\right]$: The detector noise-equivalent power.
- $\frac{d(P/P_0)}{dx}$ $[\mathrm{m}^{-1}]$: The optomechanical sensitivity.
- $P_0[\mathrm{W}]$: The nominal optical power at the detector at the transduction wavelength.

First, looking at the transduction schemes in Ch. 3 and Ch. 5 (Eq. 6-1), some combinations of the six variable inputs above are shown in Table 6.1. Guided by the numbers in Sec. 2.3.4.1, Sec. 2.3.4.2, and Sec. 2.3.4.3 we choose fixed $S_{RIN} = -130\ \mathrm{dB/Hz}$, $S_{LFN} = 200\ \mathrm{Hz}/\sqrt{\mathrm{Hz}}$, and $S_{NEP} = 0.1\ \mathrm{pW}/\sqrt{\mathrm{Hz}}$ as

representative ballpark numbers – though the reader can calculate for any other combination of noise figures, and in reality these should be spectral quantities rather than constants. The right-most column in Table 6.1 shows that, given these assumptions, the typical needed optomechanical transduction figures $\frac{d(P/P_0)}{dx}$ are on the order of $10^3 - 10^5\ \mathrm{m}^{-1}$.

	$S_{RIN}\left[\frac{\mathrm{dB}}{\mathrm{Hz}}\right]$	Q_o	$P_0[\mathrm{mW}]$	$S_{LFN}\left[\frac{\mathrm{Hz}}{\sqrt{\mathrm{Hz}}}\right]$	$S_{NEP}\left[\frac{\mathrm{pW}}{\sqrt{\mathrm{Hz}}}\right]$	$\frac{d(P/P_0)}{dx}[\mathrm{m}^{-1}]$
A	-130	1k	0.01	2e2	0.1	**1.4e5**
	-130	10k	0.01	2e2	0.1	**1.4e5**
	-130	100k	0.01	2e2	0.1	**2.0e5**
B	-130	1k	0.1	2e2	0.1	**1.4e4**
	-130	10k	0.1	2e2	0.1	**2.0e4**
	-130	100k	0.1	2e2	0.1	**1.4e5**
C	-130	1k	1	2e2	0.1	**2.0e3**
	-130	10K	1	2e2	0.1	**1.4e4**
	-130	100k	1	2e2	0.1	**1.4e5**

Table 6.1

Some combinations of inputs that achieve $1\ \mu g/\sqrt{Hz}$, for the transduction schemes in Ch. 3 and Ch. 5.

For the transduction schemes in Ch. 4 (Eq. 3-12), we have instead the following examples:

	$S_{RIN}\left[\frac{\mathrm{mW}}{\sqrt{\mathrm{Hz}}}\right]$	Q_o	P_0	$S_{LFN}\left[\frac{\mathrm{Hz}}{\sqrt{\mathrm{Hz}}}\right]$	$S_{NEP}\left[\frac{\mathrm{pW}}{\sqrt{\mathrm{Hz}}}\right]$	$\frac{d(P/P_0)}{dx}[\mathrm{m}^{-1}]$
A	-130	N/A	0.01	N/A	0.1	**1.4e5**
B	-130	N/A	0.1	N/A	0.1	**1.4e4**
C	-130	N/A	1	N/A	0.1	**1.4e3**

Table 6.2

Some combinations of inputs that achieve $1\ \mu g/\sqrt{Hz}$, for the transduction schemes in Ch. 4.

Next we proceed to summarize the $\frac{d(P/P_0)}{dx}$ found in this dissertation for comparison with the numbers in Table 6.1 and Table 6.2.

6.3 : $\frac{d(P/P_0)}{dx}$ comparison

In Ch. 3 we considered stretching a single cavity, and found (Eq. 3-12) $\frac{d(P/P_0)}{da} = 0.0056\ g^{-1}$ or $0.081\ g^{-1}$, for the 20 μm- and 5 μm-thick spring respectively. We now seek a number, $\frac{d(P/P_0)}{dx}$, that we can use to compare to the results in the other chapters. We could use the simulated or measured displacement at the tip of the cantilever, however this would be rather artificial as we are not fundamentally trying to transduce the displacement at the tip of the cantilever (imagine for example a device with identical acceleration sensitivity but longer cantilever resulting in larger displacement at the tip – thus displacement at the tip is rather meaningless), rather we are fundamentally transducing acceleration. We could use Eq. 3-7 which is ostensibly a measure of optical power change per displacement (in which case we get $37 \times 10^6\ \mathrm{m}^{-1}$ for this device), but while this is a true number it can't be directly compared to the other $\frac{d(P/P_0)}{dx}$ quoted below for Ch. 4-5. Our best option is to use Eq. 2-2 to convert to displacement sensitivity, so we use $\frac{d(P/P_0)}{dx} = \omega_m^2 \frac{d(P/P_0)}{da}$. While this results in "x" that may not correspond to any physically meaningful displacement, at least when the $\frac{d(P/P_0)}{dx}$ values for Ch. 4-5 are converted to acceleration sensitivity $\frac{d(P/P_0)}{da}$, the comparison will be a meaningful one. So, with that caveat in mind, for the stretched-ring device in Ch. 3 using Eq. 2-2 and the simulated ω_m in Ch. 3, we find $\frac{d(P/P_0)}{dx}$ to be 8.9×10^5 or $2.1 \times 10^5\ \mathrm{m}^{-1}$ respectively.

In Ch. 4 we first considered changing the waveguide-cavity gap, and found (Eq. 4-20) $\frac{d(P/P_0)}{dx} = 5.1 \times 10^6\ \mathrm{m}^{-1}$. Next in Ch. 4 we considered moving an optical absorber in the evanescent field of the cavity, and found (Eq. 4-29) $\frac{d(P/P_0)}{dx} = 5.4 \times 10^6\ \mathrm{m}^{-1}$.

In Ch. 5 we considered two stacked ring cavities, and found (Eq. 5-8) $\frac{d(P/P_0)}{dx} = 6.9 \times 10^8\ \mathrm{m}^{-1}$.

Of course, all these discrete numbers only serve as one example of the achievable transduction levels. Each one depends on so many device- and experiment-specific factors that it is entirely possible for these numbers to be many orders of magnitude different for a device with different Q_o, geometrical parameters, material parameters, excitation wavelength, etc. Therefore for each of these cases, we also considered a general model which pointed the way to understand and improve these numbers further.

However, such sensitivity numbers are rather meaningless if not compared to noise figures. Looking back at Table 6.1 and Table 6.2, we can see that for reasonable optical noise numbers, to beat the SNR reported for commercial MEMS accelerometers by two orders of magnitude may require $\frac{d(P/P_0)}{dx}$ of only around $10^3 - 10^5$, significantly smaller than all the measured numbers above.

Similar arguments may apply to gyroscopes or other MEMS devices. Of course, this is not the only thing that matters – cost and power consumption being two more salient parameters, and we considered a low-power operation mode in Sec. 1.3.5 that can potentially rival typical traditional MEMS inertial sensor power consumption (typically a few mW).

6.4 : Conclusions

In this dissertation we showed several optomechanical transduction schemes, and compared them theoretically and experimentally. As described in Sec. 1.3.7, however, reinventing the transduction scheme of a MEMS displacement sensor has a greater impact than just the device itself – it inherently requires reinventing the entire system. For example, the driving circuitry is fundamentally different and the associated noise is limited by different mechanisms. A full noise analysis using on-chip lasers and detectors coupled to such optomechanical displacement sensing devices is necessary; however in the meantime in Sec. 6.1 and Sec. 6.2 we have assumed some typical values from the literature to show that the noise of such on-chip optical systems can be much lower than, say, the electronic noise for

commercially-available MEMS accelerometers (though the argument is more generally applicable than just to accelerometers).

Considering this very rough noise analysis, we have shown that each transduction scheme in this dissertation may ultimately exceed commercial MEMS accelerometer SNR, paving the way to high-sensitivity, low-noise MEMS sensors. All transduction schemes are not equal, though – in this dissertation we have discussed some of the desirable aspects unique to each one.

Of course, much remains to be proven and there is a lot of further work to be done. We hope this dissertation has at least served to investigate some optomechanical displacement sensing transduction schemes, both quantitatively and qualitatively. By pointing out salient points that will be useful in future work we hope this dissertation can also point the way to future optomechanical sensors.

Bibliography

[1] A. W. Fang, H. Park, O. Cohen, R. Jones, M. J. Paniccia, and J. E. Bowers, "Electrically pumped hybrid AlGaInAs-silicon evanescent laser," *Opt. Express*, vol. 14, no. 20, p. 9203, 2006.

[2] H. Park, A. W. Fang, R. Jones, O. Cohen, O. Raday, M. N. Sysak, M. J. Paniccia, and J. E. Bowers, "A hybrid AlGaInAs-silicon evanescent waveguide photodetector.," *Opt. Express*, vol. 15, no. 10, pp. 6044–52, May 2007.

[3] Wikipedia, "Dynamic Stability Control." [Online]. Available: http://en.wikipedia.org/wiki/Dynamic_stability_control. [Accessed: 01-Dec-2013].

[4] Yole-Developpement, "Status of the MEMS Industry." 2011.

[5] Northrupp-Grumman, "Hemispherical Resonator Gyro (HRG)." [Online]. Available: http://www.northropgrumman.com/capabilities/hrg/Pages/default.aspx. [Accessed: 01-Dec-2013].

[6] A. A. Trusov, I. P. Prikhodko, S. A. Zotov, and A. M. Shkel, "High-Q and wide dynamic range inertial MEMS for north-finding and tracking applications," in *Proceedings of the 2012 IEEE/ION Position, Location and Navigation Symposium*, 2012, pp. 247–251.

[7] A. G. Krause, M. Winger, T. D. Blasius, Q. Lin, and O. Painter, "A high-resolution microchip optomechanical accelerometer," *Nat. Photonics*, vol. 6, no. 11, pp. 768–772, Oct. 2012.

[8] W. Kuehnel and S. Sherman, “A surface micromachined silicon accelerometer with on-chip detection circuitry,” *Sensors Actuators A Phys.*, vol. 45, no. 1, pp. 7–16, 1994.

[9] R. M. Field, J. Lary, J. Cohn, L. Paninski, and K. L. Shepard, “A low-noise, single-photon avalanche diode in standard 0.13 μm complementary metal-oxide-semiconductor process,” *Appl. Phys. Lett.*, vol. 97, no. 21, p. 211111, Nov. 2010.

[10] P. Ripka and A. Tipek, *Modern Sensors Handbook*. John Wiley & Sons, 2013.

[11] R. S. Quimby, *Photonics and Lasers: An Introduction*. John Wiley & Sons, 2006, p. 251.

[12] H. Koizumi, M. Togashi, M. Nogawa, and Y. Ohtomo, “A 10Gb/s burst-mode laser diode driver for burst-by-burst power saving,” in *2012 IEEE International Solid-State Circuits Conference*, 2012, pp. 414–416.

[13] S. J. Dixon-Warren, “Motion sensing in the iPhone 4: MEMS accelerometer.” [Online]. Available: http://www.memsjournal.com/2010/12/motion-sensing-in-the-iphone-4-mems-accelerometer.html. [Accessed: 17-Oct-2013].

[14] H. Rokhsari, T. J. Kippenberg, T. Carmon, and K. J. Vahala, “Radiation-pressure-driven micro-mechanical oscillator,” *Opt. Express*, vol. 13, no. 14, p. 5293, 2005.

[15] G. S. Wiederhecker, L. Chen, A. Gondarenko, and M. Lipson, “Controlling photonic structures using optical forces.,” *Nature*, vol. 462, no. 7273, pp. 633–6, Dec. 2009.

[16] D. Van Thourhout and J. Roels, “Optomechanical device actuation through the optical gradient force,” *Nat. Photonics*, vol. 4, no. 4, pp. 211–217, Apr. 2010.

[17] J. Rosenberg and Q. Lin, “Static and dynamic wavelength routing via the gradient optical force,” *Nat. Photonics*, vol. 3, no. July, 2009.

[18] G. S. Wiederhecker, S. Manipatruni, S. Lee, and M. Lipson, “Broadband tuning of optomechanical cavities,” *Opt. Express*, vol. 19, no. 3, pp. 2782–2790, 2011.

[19] B. Guldimann, P. Thiebaud, N. F. de Rooij, and R. A. Turpin, “Micromachined, fiber-optic based accelerometer with shutter modulation,” in *Proceedings IEEE Thirteenth Annual International Conference on Micro Electro Mechanical Systems (Cat. No.00CH36308)*, 2000, pp. 710–714.

[20] A. Malki, P. Lecoy, J. Marty, C. Renouf, and P. Ferdinand, “Optical fiber accelerometer based on a silicon micromachined cantilever.,” *Appl. Opt.*, vol. 34, no. 34, pp. 8014–8, Dec. 1995.

[21] D. Uttamchandani, D. Liang, and B. Culshaw, “A micromachined silicon accelerometer with fibre optic interrogation.” pp. 4/1–4/4, 1992.

[22] K. E. Burcham, G. N. De Brabander, and J. T. Boyd, “Micromachined silicon cantilever beam accelerometer incorporating an integrated optical waveguide,” in *Integrated Optics and Microstructures*, 1993, pp. 12–18.

[23] E. Ollier, P. Philippe, C. Chabrol, and P. Mottier, “Micro-opto-mechanical vibration sensor integrated on silicon,” *J. Light. Technol.*, vol. 17, no. 1, p. 26, 1999.

[24] M. Li, W. H. P. Pernice, and H. X. Tang, “Broadband all-photonic transduction of nanocantilevers.,” *Nat. Nanotechnol.*, vol. 4, no. 6, pp. 377–82, Jun. 2009.

[25] M. Li, W. H. P. Pernice, C. Xiong, T. Baehr-Jones, M. Hochberg, and H. X. Tang, "Harnessing optical forces in integrated photonic circuits.," *Nature*, vol. 456, no. 7221, pp. 480–4, Nov. 2008.

[26] W. H. P. Pernice, M. Li, and H. X. Tang, "Optomechanical coupling in photonic crystal supported nanomechanical waveguides," *Opt. Express*, vol. 17, no. 15, p. 12424, Jul. 2009.

[27] E. Hallynck and P. Bienstman, "Integrated Optical Pressure Sensors in Silicon-on-Insulator," *IEEE Photonics J.*, vol. 4, no. 2, pp. 443–450, Apr. 2012.

[28] D. N. Hutchison and S. A. Bhave, "Z-axis optomechanical accelerometer," in *2012 IEEE 25th International Conference on Micro Electro Mechanical Systems (MEMS)*, 2012, pp. 615–619.

[29] Y. Wu, X. Zeng, Y. Rao, Y. Gong, C. Hou, and G. Yang, "MOEMS Accelerometer Based on Microfiber Knot Resonator," *IEEE Photonics Technol. Lett.*, vol. 21, no. 20, pp. 1547–1549, Oct. 2009.

[30] B. Bhola, W. H. Steier, and L. Fellow, "A Novel Optical Microring Resonator Accelerometer," *Sensors (Peterborough, NH)*, vol. 7, no. 12, pp. 1759–1766, 2007.

[31] X. Zhao, J. M. Tsai, H. Cai, X. M. Ji, J. Zhou, M. H. Bao, Y. P. Huang, D. L. Kwong, and A. Q. Liu, "A nano-opto-mechanical pressure sensor via ring resonator.," *Opt. Express*, vol. 20, no. 8, pp. 8535–42, Apr. 2012.

[32] P. J. Harmsma, M. J. Engelmann, R. Schmits, W. J. Westerveld, J. H. van den Berg, K. Agovic, R. E. van Vliet, and M. Yousefi, "Photonic pressure sensor in silicon on insulator," in *CLEO/Europe - EQEC 2009 - European Conference on Lasers and Electro-Optics and the European Quantum Electronics Conference*, 2009, pp. 1–1.

[33] R. L. Waters, M. E. Aklufi, and T. E. Jones, “Electro-Optical Ultra Sensitive Accelerometer,” *Opt. Eng.*, no. 100, pp. 36–43, 2002.

[34] R. L. Waters and M. E. Aklufi, “Micromachined Fabry–Perot interferometer for motion detection,” *Appl. Phys. Lett.*, vol. 81, no. 18, p. 3320, 2002.

[35] M. A. Perez and A. M. Shkel, “Design and Demonstration of a Bulk Micromachined Fabry-Perot microg-Resolution Accelerometer,” *IEEE Sensors (Peterborough, NH)*, vol. 7, no. 12, pp. 1653–1662, 2007.

[36] K. Zandi, B. Wong, J. Zou, R. V Kruzelecky, W. Jamroz, and Y. Peter, “In-plane silicon-on-insulator optical MEMS accelerometer using waveguide fabry-perot microcavity with silicon/air bragg mirrors,” *Micro Electro Mech. Syst. (MEMS), 2010 IEEE 23rd Int. Conf.*, no. 24–28 Jan 2010, pp. 839–842, 2010.

[37] F. G. Cervantes, L. Kumanchik, J. Pratt, and J. Taylor, “Self-calibrating optomechanical accelerometer with high sensitivity over 10 kHz,” Mar. 2013.

[38] A. H. Safavi-Naeini, T. P. M. Alegre, M. Winger, and O. Painter, “Optomechanics in an ultrahigh-Q two-dimensional photonic crystal cavity,” *Appl. Phys. Lett.*, vol. 97, no. 18, p. 181106, 2010.

[39] A. M. Jayich, J. C. Sankey, B. M. Zwickl, C. Yang, J. D. Thompson, S. M. Girvin, A. A. Clerk, F. Marquardt, and J. G. E. Harris, “Dispersive optomechanics: a membrane inside a cavity,” *New J. Phys.*, vol. 10, no. 9, p. 095008, Sep. 2008.

[40] M. Karuza, C. Molinelli, M. Galassi, C. Biancofiore, R. Natali, P. Tombesi, G. Di Giuseppe, and D. Vitali, "Optomechanical sideband cooling of a thin membrane within a cavity," *New J. Phys.*, vol. 14, no. 9, p. 095015, Sep. 2012.

[41] W. Mo, H. Wu, and D. Gao, "A novel accelerometer based on microring resonator," *Chinese Opt. Lett.*, vol. 7, no. 9, pp. 798–801, 2009.

[42] G. Anetsberger, O. Arcizet, Q. P. Unterreithmeier, R. Rivière, a. Schliesser, E. M. Weig, J. P. Kotthaus, and T. J. Kippenberg, "Near-field cavity optomechanics with nanomechanical oscillators," *Nat. Phys.*, vol. 5, no. 12, pp. 909–914, Oct. 2009.

[43] O. Basarir, S. Bramhavar, and K. L. Ekinci, "Monolithic integration of a nanomechanical resonator to an optical microdisk cavity.," *Opt. Express*, vol. 20, no. 4, pp. 4272–9, Feb. 2012.

[44] K. Srinivasan, H. Miao, M. Rakher, and M. Davanco, "Optomechanical transduction of an integrated silicon cantilever probe using a microdisk resonator," *Nano Lett.*, pp. 1–11, 2010.

[45] Y. Liu, H. Miao, V. Aksyuk, and K. Srinivasan, "Integrated cavity optomechanical sensors for atomic force microscopy," in *2012 Microsystems for Measurement and Instrumentation (MAMNA)*, 2012, pp. 1–3.

[46] Y. Liu, H. Miao, V. Aksyuk, and K. Srinivasan, "Wide cantilever stiffness range cavity optomechanical sensors for atomic force microscopy.," *Opt. Express*, vol. 20, no. 16, pp. 18268–80, Jul. 2012.

[47] H. Miao, K. Srinivasan, and V. Aksyuk, "A microelectromechanically controlled cavity optomechanical sensing system," *New J. Phys.*, vol. 14, no. 7, p. 075015, Jul. 2012.

[48] Houxun Miao, K. Srinivasan, and V. Aksyuk, “Integrated MEMS tunable high quality factor optical cavity for optomechanical transduction.” pp. 1–2, 2010.

[49] M. Davanço, J. Chan, A. H. Safavi-Naeini, O. Painter, and K. Srinivasan, “Slot-mode-coupled optomechanical crystals.,” *Opt. Express*, vol. 20, no. 22, pp. 24394–410, Oct. 2012.

[50] M. I. Davanco, J. Chan, A. Safavi-Naeini, O. Painter, and K. Srinivasan, “Si3N4 nanobeam optomechanical crystals,” in *CLEO: 2013*, 2013, p. CW3F.2.

[51] K. G. McConnell and P. S. Varoto, *Vibration testing: Theory and practice, Second edition*. Wiley, 2008.

[52] S. Tanaka, S.-H. Jeong, S. Sekiguchi, T. Kurahashi, Y. Tanaka, and K. Morito, “High-output-power, single-wavelength silicon hybrid laser using precise flip-chip bonding technology.,” *Opt. Express*, vol. 20, no. 27, pp. 28057–69, Dec. 2012.

[53] C. Spiegelberg, J. Geng, Y. Hu, Y. Kaneda, S. Jiang, and N. Peyghambarian, “Low-Noise Narrow-Linewidth Fiber Laser at 1550 nm (June 2003),” *J. Light. Technol.*, vol. 22, no. 1, pp. 57–62, Jan. 2004.

[54] G. A. Cranch, “Frequency noise reduction in erbium-doped fiber distributed-feedback lasers by electronic feedback,” *Opt. Lett.*, vol. 27, no. 13, p. 1114, Jul. 2002.

[55] C. T. DeRose, D. C. Trotter, W. A. Zortman, A. L. Starbuck, M. Fisher, M. R. Watts, and P. S. Davids, “Ultra compact 45 GHz CMOS compatible Germanium waveguide photodiode with low dark current.,” *Opt. Express*, vol. 19, no. 25, pp. 24897–904, Dec. 2011.

[56] N. Biyikli, O. Aytur, I. Kimukin, T. Tut, and E. Ozbay, “Solar-blind AlGaN-based Schottky photodiodes with low noise and high detectivity,” *Appl. Phys. Lett.*, vol. 81, no. 17, p. 3272, 2002.

[57] COMSOL Inc., “Stress-Optical Effects in a Photonic Waveguide.” [Online]. Available: http://www.comsol.com/model/download/178401/models.woptics.stress_optical.pdf. [Accessed: 01-Oct-2013].

[58] G. Anetsberger, R. Rivière, A. Schliesser, O. Arcizet, and T. J. Kippenberg, “Ultralow-dissipation optomechanical resonators on a chip,” *Nat. Photonics*, vol. 2, no. 10, pp. 627–633, Sep. 2008.

[59] A. W. Fang, E. Lively, Y.-H. Kuo, D. Liang, and J. Bowers, “Distributed Feedback Silicon Evanescent Laser,” in *Optical Fiber Communication Conference/National Fiber Optic Engineers Conference*, 2008, p. PDP15.

[60] A. Yariv, “Universal relations for coupling of optical power between microresonators and dielectric waveguides,” *Electron. Lett.*, vol. 36, no. 4, p. 321, 2000.

[61] D. G. Rabus, *Integrated Ring Resonators: The Compendium (Springer Series in Optical Sciences)*. Springer, 2007, p. 274.

[62] B. E. Little, S. T. Chu, H. A. Haus, J. Foresi, and J. P. Laine, “Microring resonator channel dropping filters,” *Light. Technol. J.*, vol. 15, no. 6, pp. 998–1005, 1997.

[63] T. J. Kippenberg and K. J. Vahala, “Cavity Opto-Mechanics,” *Opt. Express*, vol. 15, no. 25, p. 17172, 2007.